Experimental and numerical study of an aircraft seat

POLITECNICO DI BARI

Dipartimento di Meccanica, Matematica e Management

DOTTORATO DI RICERCA IN INGEGNERIA MECCANICA E GESTIONALE

SSD: ING-IND/14 – PROGETTAZIONE MECCANICA E COSTRUZIONE DI MACCHINE

EXPERIMENTAL AND NUMERICAL STUDY OF AN AIRCRAFT SEAT

Marika PATRONELLI

Supervisori

Prof.ssa Caterina CASAVOLA, PhD

Prof. Giovanni PAPPALETTERA, PhD

Ing. Lucia DEL CORE, PhD

Coordinatore:

Prof. Giuseppe Pompeo DEMELIO

XXXV ciclo, Triennio: 2019-2023

Dedication

This doctoral thesis is dedicated to my son *Raul*, born during this journey, bringing light, love, and happiness into my life.

Questa tesi di dottorato è dedicata a mio figlio *Raul*, nato durante questo percorso portando luce, amore e felicità nella mia vita.

Abstract

The aircraft certification process is a complex and costly undertaking for a company, involving a meticulous material selection process and the execution of experimental tests to prove compliance with existing regulations. This dissertation is focused on the development of a complex numerical-experimental methodology aimed at evaluating the crashworthiness of an aeronautical seat. This methodology takes into account not only the materials involved and their thickness, but also critical impact conditions described in CS 23.562. What sets this research apart is the seat configuration, which is fully integrated into the aircraft's fuselage structure. This type of seating refers to a specialized aircraft seating arrangement where passenger seats are an integral part of the aircraft's fuselage, as opposed to being standalone fixtures. This design concept is commonly found in modern commercial airliners and offers several advantages, including increased aircraft design flexibility, weight reduction, space efficiency, decreased maintenance requirements, and enhanced passenger comfort. From a safety perspective, integrated seats have the potential to provide robust safety features as they distribute loads across a larger surface area. However, due to the seat's inherent rigidity as a structural component, it can transmit high loads to the pilot. Additionally, in the specific case under consideration, the only element designed to mitigate lumbar loads is the seat cushion. Therefore, the selection of material for the seat cushion becomes a critical factor. The physical properties of these cushions, if chosen incorrectly, can amplify the pelvic load on the seated occupant during a vertical impact event. This study is structured into six chapters, each focusing on specific lines of inquiry. The first chapter is an introduction and provides a general overview of the topics covered in the thesis. The second chapter provides an overview of the regulatory framework and the regulatory authority relevant in the aviation sector. Follows an *excursus* of aviation safety and the update of safety standards as a direct consequence of technological progress. In fact, as will be seen, there is currently a shift towards performance standards, as this approach allows for the surpassing of outdated solutions. The focus then turns to the type certificate and light aircraft in the prospective of the discussion about the increased weight of the aircraft under analysis, Bk 160. Chapter 3 is an introduction to the seat as a safety device. It describes the impact problem and the crashworthiness based on the crash physics, involving the work-energy relationships, and analyzing the energy content of an aircraft during an impact. The core of the chapter is, therefore, the seat, seen as the primary safety device protecting the pilot and the occupant in case of emergency landing conditions. Different technical solutions for energy absorption and seat validation for the aircraft class under study are discussed considering the current regulations. Chapter 4 is entirely dedicated to the mechanical characterization of the foams used for the seat cushion. Crucial to detect the deformation of the foams during the tests is the measurement technique, namely digital image correlation (DIC), that will be presented. Polyurethane foams and their properties are introduced, and experimental and

numerical results for tensile, shear, and cyclic compression tests are provided. The crashworthiness analysis is presented in chapter 5, which is dedicated to multibody modelling by Madymo. Due to the significant time and cost associated with seat certification, aviation authorities recommend the use of numerical simulations, particularly dynamic analysis, as a complementary approach to support the seat approval process. This also necessitates the use of validated virtual dummies, in this case, the Hybrid III 50th Percentile Dummy provided by Siemens. While experimental dynamic testing cannot be entirely replaced, numerical simulations offer valuable capabilities for assessing critical loads and estimating injury criteria. In this specific case, these functionalities are particularly advantageous. Since the seat is integrated into the fuselage, conducting an impact test using the entire aircraft fuselage would be required. This would entail the need for a dedicated setup and the construction of aircraft solely for this purpose. It is evident that the costs associated with such approach would be significantly higher compared to conducting the test using the seat mounted on the conventional deceleration sled. The dissertation will conclude in Chapter 6, where a summary of the results will be presented.

Sommario

Il processo di certificazione di un velivolo rappresenta un'operazione complessa e onerosa per qualsiasi azienda, coinvolgendo una rigorosa selezione dei materiali e l'esecuzione di test sperimentali per dimostrare la conformità alle normative vigenti. Questa tesi è incentrata sullo sviluppo di una strategia numerica e sperimentale per verificare la risposta all'impatto di una seduta aeronautica e la conformità con la CS 23.562 relativa alle condizioni dinamiche di atterraggio di emergenza. Ciò che distingue questa ricerca è la configurazione del sedile, completamente integrato nella struttura della fusoliera dell'aereo. Questo tipo di configurazione della seduta fa riferimento ad una progettazione specifica in cui il sedile è parte integrante della fusoliera dell'aereo, anziché essere installato come elemento distinto. Questo concetto di progettazione lo si trova più frequentemente nei moderni aerei di linea commerciali e offre vari vantaggi, tra cui una maggiore flessibilità nella progettazione dell'aeromobile, una riduzione del peso, una maggiore efficienza dello spazio, minori requisiti di manutenzione e un miglior comfort per i passeggeri. Dal punto di vista della sicurezza, i sedili integrati hanno il potenziale di conferire robustezza alla seduta e sono più sicuri poiché distribuiscono i carichi su una superficie più ampia. Tuttavia, a causa della loro intrinseca rigidità, data dal fatto di essere a tutti gli effetti un componente strutturale, le sedute integrate possono trasmettere carichi elevati all'occupante. Inoltre, per il caso specifico in analisi, l'unico elemento adibito a mitigare i carichi lombari è il cuscino del sedile. Pertanto, la scelta del materiale per il cuscino del sedile diventa un fattore critico. Le proprietà fisiche di questi cuscini, se scelte in modo errato, possono amplificare il carico pelvico sul passeggero durante un evento di impatto verticale.

Questa ricerca è strutturata in sei capitoli, ciascuno dei quali si concentra su specifiche linee di indagine. Il primo capitolo è di introduzione e fornisce una panoramica generale sugli argomenti trattati nella tesi. Il secondo capitolo fornisce un'ampia panoramica del quadro normativo e delle autorità regolatrici rilevanti nel settore dell'aviazione. Segue una panoramica sulla sicurezza dell'aviazione e l'aggiornamento degli standard di sicurezza come diretta conseguenza del progresso tecnologico. Attualmente, come verrà illustrato, si sta verificando un passaggio verso gli standard di prestazione, poiché questo approccio consente di superare soluzioni obsolete. L'attenzione si sposta quindi sul certificato di tipo e sugli aeromobili leggeri nella prospettiva della discussione sull'aumento del peso dell'aeromobile in esame, il Bk 160. Il terzo capitolo rappresenta un'introduzione al sedile come dispositivo di sicurezza. Esso descrive il problema dell'impatto e la crashworthiness basata sulla fisica di un impatto, coinvolgendo, quindi, le relazioni tra lavoro ed energia e analizzando il contenuto energetico di un aeromobile durante un impatto. Il cuore del capitolo è il sedile, visto come il dispositivo di sicurezza primario che protegge il pilota e l'occupante in caso di condizioni di atterraggio d'emergenza. Sono discusse diverse soluzioni tecniche per l'assorbimento dell'energia e la convalida del sedile per la classe di aeromobili in studio, tenendo

conto delle normative attuali. Il quarto capitolo è interamente dedicato alla caratterizzazione meccanica delle schiume utilizzate per il cuscino del sedile. La tecnica cruciale per rilevare la deformazione delle schiume durante i test è la Digital Image Correlation (DIC). Sempre nel 4 capitolo sono introdotte le schiume di poliuretano e le loro proprietà, e vengono forniti risultati sperimentali e numerici per i test di trazione, taglio e compressione ciclica. L'analisi della crashworthiness è presentata nel quinto capitolo, che è dedicato alla modellazione multi-body con Madymo. A causa dei tempi e dei costi associati alla certificazione dei sedili, le autorità dell'aviazione raccomandano l'uso di simulazioni numeriche, in particolare l'analisi dinamica, come approccio complementare per supportare il processo di approvazione del sedile. Questo comporta anche l'uso di manichini virtuali convalidati, in questo caso, il manichino Hybrid III al 50° percentile fornito da Siemens. Anche se i test dinamici sperimentali non possono essere completamente sostituiti, le simulazioni numeriche offrono capacità preziose per valutare i carichi critici e stimare i criteri di lesione. In questo caso specifico, queste funzionalità sono particolarmente vantaggiose. Poiché il sedile è integrato nella fusoliera, sarebbe necessario condurre un test d'impatto utilizzando l'intera fusoliera dell'aereo. Ciò comporterebbe la necessità di una configurazione dedicata e la costruzione di aeromobili esclusivamente per questo scopo. È evidente che i costi associati a un tale approccio sarebbero significativamente più elevati rispetto alla conduzione del test utilizzando il sedile montato sulla tradizionale slitta di decelerazione dedicata ai test dinamici. La tesi si concluderà col sesto Capitolo, in cui è presentata la sintesi dei risultati.

Contents

List of Figures

List of Tables

1. Introduction

On December 17, 1903, the Wright brothers conducted the first flight experiment. They covered a mere 36 meters, and the aircraft remained airborne for only 12 seconds. This event marked the beginning of a new era: mankind was capable of flying. In a hundred years, the skies all over the world have been traversed by thousands of aircraft of various types and sizes, serving diverse purposes such as military defense, transportation, acrobatic performances, and more. The aviation industry is in constant evolution, thanks to the continuous introduction of new materials and technologies, which drive ongoing updates to aviation safety standards. It is well-known that, from a design perspective, increasingly lighter materials with high mechanical properties are being used, such as carbon fiber. The result is that, compared to the past, aircraft are now lighter but with higher performance capabilities.

1.1. Motivation of the research

In the present thesis, the upgrading process of a two-seats carbon fiber aircraft from the CS-VLA category to the higher CS-23 category will be discussed. This would enable the aircraft to be used in new areas such as flight training and aerobatic flying, thus expanding the growth potential for the manufacturing company and its target market. Obtaining certification for the CS-23 category requires the implementation of new design procedures, particularly with regard to more stringent experimental verification of the aircraft's structure, especially concerning passenger safety in the event of an accident. Therefore, the aim of the present work is the study of passive safety or crashworthiness of the aircraft. The primary safety system for the pilot/passenger of the aircraft treated in this study is the seat, as it is responsible for absorbing a significant portion of the energy generated during an impact. CS-VLA class aircraft only have limited requirements for impact safety verification. In higher-class aircraft, regulations call for specific tests and modeling to assess accelerations, i.e., the forces transferred to passengers during an impact. The aircraft under study also has the unique feature of the seat being an integral part of the structure, contributing to its rigidity and structural strength. To adapt the aircraft to these regulations, it is necessary to first analyze the critical points and limitations of the current structure, followed by an initial design phase to identify potential solutions, including the development of removable absorption systems (cushions) and potential redesign of the seat-to-fuselage attachment system.

In this work, following the initial redesign phase, an experimental characterization campaign of the materials to be used for the cushions was conducted, providing designers with valuable information to create numerical models that are as accurate and realistic as possible. To study the entire strain field of extremely soft materials, non-destructive and non-contact optical measurement techniques

should be used. In fact, in soft materials, clip-on or contact extensometers should be avoided because they cannot be directly applied on the material as they would deform it. Some difficulties can be overcome by using full-field strain measurement methods, such as digital image correlation (DIC). The foams tested in this study can be analyzed in an original manner thanks to the small black particles of expandable graphite randomly scattered into the material, making it fireproof.

Experimental data is crucial for numerically modelling the hyperelastic behavior of foams and for progressing to the final design of the aircraft. Regulation CS-23.562 Amendment 4 requires the execution of two dynamic tests directly on the seat. Given the unique nature of the studied aircraft, where the seat is integrated into the structure, the test must be conducted on a section of the entire structure, requiring appropriate design of the experimental setup. In order to reduce the number of costly full-scale tests required for structural certification, numerical modeling of impact tests is highly significant. To this end, modeling has been carried out using the multibody software Madymo provided by Siemens. In special circumstances, as will be explained in the next chapter, the company can reach an agreement with the relevant aviation authority, in this case, EASA, to establish a *special condition* aimed at simplifying, if the requirements are met, the aircraft certification process.

Therefore, improvements in the aircraft's impact resistance will expand its usability and enhance passenger safety, with significant implications for the aerospace industry. The acquired know-how will also enable the development of future projects for higher-class aircraft.

1.2. Objectives and proposed research topics

As discussed in the previous section, the main research objective is the study of crashworthiness for an upgraded version of the actual Bk160 Gabriél aircraft in compliance with the CS-23 Amdt 5. The new aircraft will be aimed for the training of professional pilots belonging to both civilian and military organizations. In order to carry out this study, three lines of investigation can be defined as follows:

1. Regulatory framework and preliminary design:
    - the first phase of the work involves studying the prerequisites of the standard that must be complied with, in this case, CS-23 Amdt 5, to identify: engineering requirements, material characteristics to be used, referenced speeds and accelerations, static and dynamic tests to be conducted for the experimental validation of the aircraft.
    - examine the current aircraft configuration, including the design, materials, performance, and characteristic speeds, to identify the limitations of the current configuration compared to the one to be implemented, which requires more rigorous experimental checks, especially to ensure passenger safety in the event of an accident. In this regard, particular attention will

be given to the study of the aircraft seat, which serves as the primary safety system for the pilot/passenger;

- evaluation of available space, potential interferences, and alternative materials for both the structural part and the seat itself. Among the various plausible solutions, there is the identification of removable absorption systems (cushions) capable of absorbing energy in the event of an impact using materials with different mechanical characteristics than the current ones.

2. Experimental characterization campaign:
    - among the data of significant interest for the mechanical characterization of materials, there are: tensile strength, compressive strength, shear strength, cyclic compression behavior for the analysis of hysteresis and softening phenomena. The seat is an element in direct contact with the occupant, so, in addition to being safe, it must also be ergonomic;
    - the study of soft, hyperelastic materials requires the use of non-destructive and non-contact optical measurement techniques. Therefore, digital image correlation (DIC) was employed, which typically involves applying a speckle pattern to the analyzed area. The technique was applied innovatively, taking advantage of the presence of small fireproof graphite particles within the material, without applying any speckle pattern.
3. Numerical Modelling:
    - numerical replications of experimental tests and numerical modeling of hyperelastic materials using finite element software (Abaqus);
    - dynamic simulations performed by a combination of finite element software and multibody analysis (Madymo). The multibody software includes virtual dummy models that provide initial information on the velocities and accelerations experienced by occupants. This design approach allows for conducting initial preliminary assessments to select the best solutions for the execution of experimental impact tests, that, as mentioned in the previous section, are really expensive.

1.3. Blackshape Bk 160 Gabriél

Blackshape is an Apulian company, established a few years ago and quickly gaining prominence in the aerospace industry. At its facility located in Monopoli, they manufacture small aircraft falling within the categories of light and ultralight aircraft, primarily constructed using carbon fiber. The use of carbon fiber, in addition to ensuring high performance and operational standards, has allowed the company, and its designers, to introduce modern and appealing designs without sacrificing important aspects such as structural safety and cabin comfort. Considering modern designs, carbon fiber lends to versatile shaping while simultaneously maintaining high physical and mechanical properties.

Figure 1Blackshape Bk 160 Gabriél aircraft.

Figure 2 Blackshape Bk 160 Forward Fully Integrated seat.

The meticulous work of engineers and technical personnel within the company enables the management of the entire aircraft production line, starting from the pre-impregnated materials processed in the clean room, continuing with the molding/polymerization processes in the autoclave, and concluding with the assembly of parts to provide a valid product. The quality and safety of the aircraft produced by Blackshape, which is part of the larger Angel group, are further ensured by the type certificate issued by EASA (European Union Aviation Safety Agency). Bk 160 Gabriél (Figure 1) with tandem seats, retractable landing gear, and a Hartzell three-blade composite constant speed propeller driven by a 160 horsepower Lycoming IO-320, has performance exceeding by far those of the category, with a top speed of 164kts and a flight envelope of +5 -2,5g to manoeuvres the aircraft while enjoying its flying qualities [1]. A view of the forward fully integrated seat structures, together with the controls and the front view of the cabin, it is provided in Figure 2.

2. Regulatory framework

"It is inconceivable to imagine a world without aviation. Moreover, it is almost impossible to imagine a world of aviation without safety regulation" [2].

Ronald I. C. Bartsch

2.1. Reference Institutions in the Aviation Industry

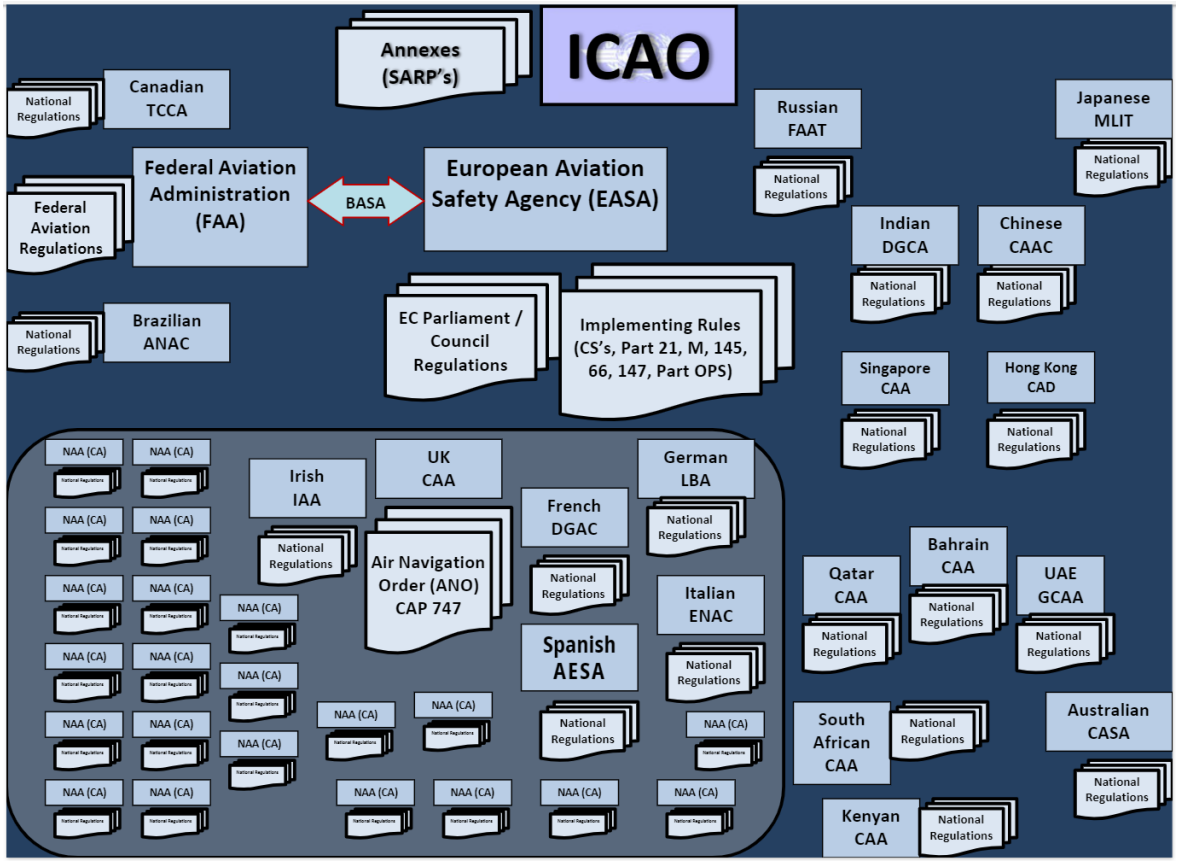

Figure 3 Global Overview of Regulatory Authorities which are responsible for drafting and verifying the enforcement of mandatory rules for the aviation industry [3].

Aviation law is considered a matter of international law due to the nature of air travel. In the international realm, the International Civil Aviation Organization (ICAO) provides general rules and mediates international concerns to an extent regarding aviation law. In the United States aviation law is considered a federal or state-level concern and is regulated at that level. Also, Europe followed the US example and founded EASA, an organization that operate at the European level that obliges the member states of the European Union and the non-member states which take part (i.e. Switzerland) to adopt common rules in the civil aviation sector with the aim of achieving high levels of safety and environmental compatibility as well as the free exchange of goods, products and services.

Therefore, in the individual states the authorities that already existed continue to operate (i.e. ENAC in ITALY and LBA in Germany) following the directives issued by EASA. There are other states (Canada, India, China) in which the aviation authorities operate at a national level following the guidelines of the international organization (ICAO). Figure 3 provides a comprehensive view of regulatory authorities on a global scale. These entities play a crucial role in the aviation industry by not only creating but also ensuring the implementation of mandatory regulations. They are responsible for maintaining safety standards, operational guidelines, and overall compliance within the aviation sector. In summary, Figure 3 showcases the interconnectedness and cooperation among the aviation entities in order to maintain the highest level of safety and efficiency in aviation worldwide.

Figure 4 Schematic of the aviation authorities from the global to the national level.

Figure 2 illustrates the hierarchical structure of aviation authorities, spanning from the global level down to the national level. It demonstrates how the aviation regulatory framework is organized, with global organizations such as the International Civil Aviation Organization (ICAO) at the top, setting international standards and guidelines. Beneath them, there are regional authorities that adapt and implement these standards in their respective regions. Finally, at the national level, there are individual aviation authorities responsible for overseeing aviation operations and compliance within their countries. This figure helps to visualize the multi-tiered approach to aviation regulation and highlights the collaboration among different levels of authority to ensure safe and efficient air travel.

2.1.1. FAA and EASA

The Federal Aviation Administration (FAA) was established in 1958 by the United States Department of Transportation to regulate and oversee all aspects of U.S. civil aviation. In Europe, the European Union established the European Union Aviation Safety Agency (EASA) in 2002 to take over the functions of the Joint Aviation Authorities (JAA), which had been active since 1970. EASA fully

assumed its functions starting in 2008 and currently also involves countries within the European Free Trade Association (EFTA). The tasks performed by these agencies are diverse and complex, including regulating commercial space transportation, implementing and monitoring safety regulations, conducting inspections in member states, certifying aircraft and components, assisting in the development of new technologies, suspending or revoking pilot certificates, conducting ongoing research to enhance safety, managing air traffic control systems, approving or disapproving organizations involved in aircraft design, and implementing programs to control aircraft noise and other environmental impacts.

These two entities are the authors of various regulatory codes that will be referenced in the upcoming chapters. Here is an example to help the reader navigate the world of aviation rules. It is common to encounter abbreviations such as CS 23.561 or FAR Part 23.561, both related to Emergency Landing Conditions. The first belongs to the Implementation Rules found in the Certification Specification (CS) section, which compiles various requirements categorized by aircraft elements or classes based on their function, aircraft performance, and passenger capacity. The second is part of the Federal Aviation Regulation (FAR), which encompasses sections (Part) related to the specific aeronautical product to be certified. For example, transport aircraft must meet the requirements outlined in "Part 25," engines in "Part 33," propellers in "Part 35," and so forth. Both agencies separately publish explanatory information and additional details, often referred to as non-binding standards, which include Acceptable Means of Compliance (AMC) for EASA and Advisory Circular (AC) for FAA. Additionally, Guidance Materials (GM) are also provided by these agencies.

2.1.2. Aviation Safety and key statistics

In Europe, EASA annually collects data on aircraft approved according to its own standards and publishes them in the *Annual Safety Review*. The issue of impact and its effects on human health is a topic of utmost importance for safety and applies to any type of moving vehicle. This field is mainly known as c*rashworthiness*.

Fatalities involving airplane and cargo operations worldwide are a critical concern in the aviation industry. These tragic incidents involve the loss of human lives and often have far-reaching consequences for families, communities, and the industry as a whole.

Aviation safety is a paramount priority for regulatory authorities, airlines, aircraft manufacturers, and all stakeholders involved. Various safety measures and protocols, such as rigorous pilot training, aircraft maintenance standards, air traffic control procedures, and advanced technology like collision avoidance systems, are continuously developed and improved to mitigate the risk of accidents. Statistical analysis of fatalities in the aviation sector provides valuable insights into trends, potential areas for improvement, and the effectiveness of safety initiatives. This data is essential for identifying

and addressing specific challenges in aviation safety and for continually striving to enhance the safety of airplane passenger and cargo operations worldwide.

Figures below show the contribution of EASA Member States' operators to the number of global fatal accidents and fatalities.

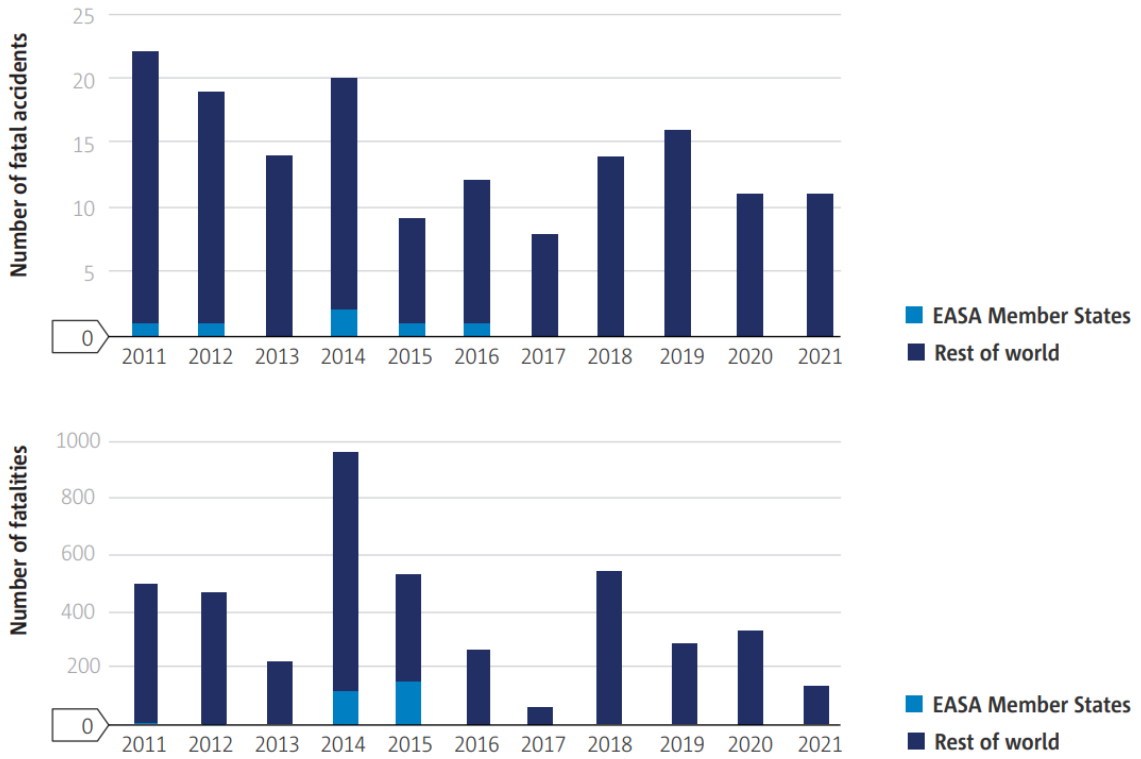

Figure 5 Fatal accidents and fatalities involving aeroplane passenger and cargo operations, EASA Member States and the rest of the world [4].

Figure 5 shows that the number of fatal accidents in recent years has stabilized, despite the reduction in air traffic caused by the COVID-19 pandemic in 2020 and 2021. As such, both regulators and the industry should remain highly vigilant to aviation safety risks. Despite the stabilization in the number of accidents, the number of fatalities in 2021 is the second lowest in the decade. This contrast is largely because over half of the fatal accidents in 2021 involved cargo operations, with fewer people onboard the aircraft [4]. The definition of an accident is set out in EU law [5] and in Annex 13 to the Convention on International Civil Aviation (Chicago Convention). Although this definition excludes unlawful acts, such acts have often been investigated by safety investigation authorities and the management of safety and security risks are increasingly connected. This year for the first time, the data presented in Figure 6 has been divided to show the fatalities related to accidents and those related to unlawful acts. Whereas accidents have reduced markedly since 1970 and then more slowly in recent years, fatalities related to unlawful acts have re-emerged since 2014. When focusing on this

most recent period (2014-2021), the fatalities caused by unlawful acts represent a significant percentage of the total number of fatalities. This observation, in conjunction with the current challenges associated with the developing geopolitical situations, increasingly focuses concern on security matters that require an integrated risk management approach in order to be adequately mitigated [4].

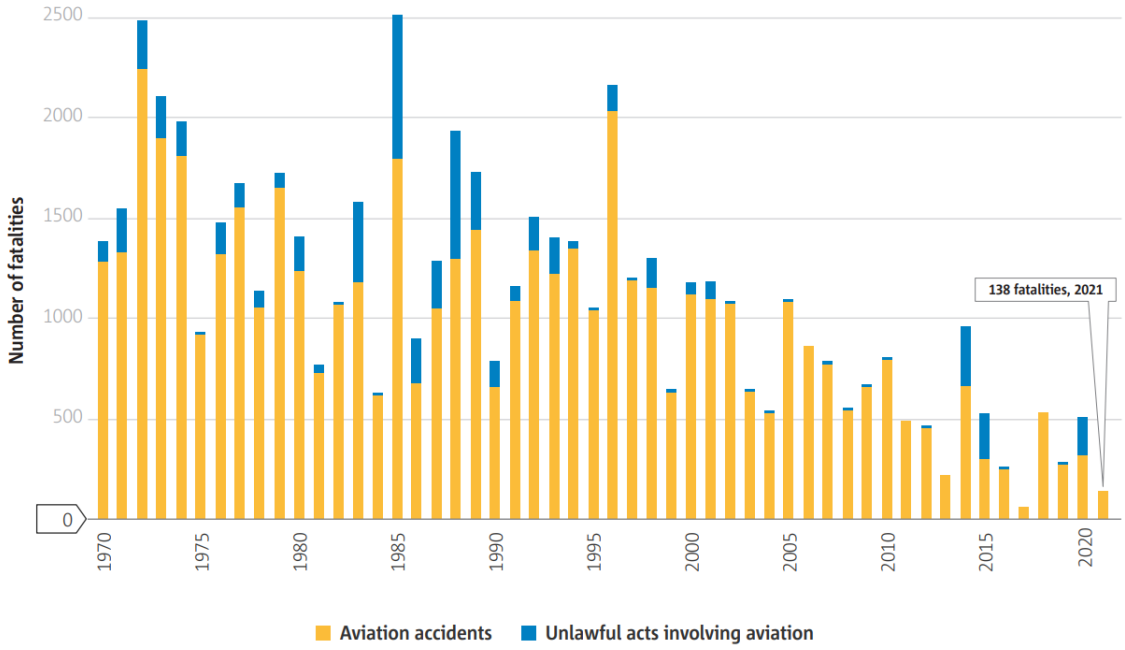

Figure 6 Fatalities involving aeroplane passenger and cargo operations worldwide [4].

From the data presented in the images above, it is evident that aviation authorities carry out meticulous work to minimize the possibility of fatalities. As mentioned in the introduction, this extensive effort necessitates constant updates in new technologies and assessments of new materials and design procedures. Compliance with the rules requires significant effort from companies, but at the same time, it ensures the safety of designing an aircraft correctly to reduce the number of fatalities as much as possible.

2.2. Airworthiness

Airworthiness of an aircraft is the fitness of an aircraft for flight in all conditions for which it has been designed, and to which it may therefore be exposed [6]. This means that during the whole lifecycle of the aircraft, for all types of operations and in all environments, the structure of the aircraft must remain unchanged. To that end, every aircraft must first be certified. The certification process, also known as initial airworthiness, is carried out in the EU by the European Union Aviation Safety

Agency (EASA) on behalf of the Member States. The common technical requirements and administrative procedures for the airworthiness and environmental certification of aircraft are set out in Regulation (EU) No 748/2012 [7]. During the aircraft's lifetime, 'continuing airworthiness activities' are carried out to ensure continuous fitness for flight [6]. The common technical requirements and administrative procedures for the continuing airworthiness are set out in Regulation (EU) No 1321/2014 [8].

The certification of airworthiness for civil aircraft is based on two principles: the use of prescriptive safety standards in design, and inspections and tests to verify compliance with regulations. It is an axiom that prescriptive safety standards are based on experience and therefore do not pre-empt technological advancements. In other words, safety design rules in the aviation industry are established reactively rather than proactively [9]. Currently, there is a trend towards a shift to performance standards, as will be clarified in the following paragraphs. This ongoing transition encourages the adoption of new technologies to implement solutions and tools that are in line with the times.

2.2.1. Type Certificate

To commercialize and operate any category of aircraft in various countries around the world, it is necessary for the aircraft to have gone through and passed the various steps of the certification process in the respective country. The Type Certificate or Certification (Type Certificate) is issued by the aviation authority of the nation where the aircraft will operate when compliance with the airworthiness requirements specified by current regulations is demonstrated.

In the European Union, EASA (European Union Aviation Safety Agency) issues the civil type certificate based on the requirements outlined in Regulation (EC) 216/2008 and their respective implementation rules, known as Part 21. In the United States, the responsible body is the FAA (Federal Aviation Administration), and the requirements that an aeronautical product must meet are contained in the Federal Aviation Regulations (FAR). Any addition, subtraction, or modification to the approved configuration in the certification requires additional certification. The Type Certificate Holder (TCH) must also establish a list of maintenance operations that the aeronautical product must undergo periodically to maintain its airworthiness certificate. When the type certificate holder decides to cease support, they return the certificate to the aviation authority, and the related fleet is grounded, as was the case when Airbus returned the Concorde's certificate, for example [10].

When the modification being proposed is substantial (for example, one that alters flight performance, fuselage dimensions, or the type of installed engines), it is necessary to go through a new certification process to obtain a new type certificate. However, if the new aircraft does not deviate significantly from the previous version, it is also possible to avoid some very costly tests [10].

2.2.2. Prescriptive safety standards

Prescriptive safety standards are standards that specify design requirements, such as the materials to be used, how a certain characteristic should be achieved, or how an item should be manufactured, so that the object can be considered safe. A prescriptive requirement is a design solution explicitly mandated for an implicit safety objective. Generally, prescriptive requirements are very useful at the lower levels of the product hierarchy (at the level of parts, bolts, nuts, tanks, batteries, etc.). Prescriptive standards (also known as design standards or rule-based standards) are easy for the manufacturer to implement and for the certifying authority to verify compliance. Planning is efficient because it simply needs to read and incorporate them into the design. The disadvantages of prescriptive standards are that they may be effective in some cases but not in others; they can prove to be more expensive than equally effective alternative solutions; they can inhibit innovation and become outdated; they are reactive (revised and changed after incidents) and can lead to over-engineered or under-engineered solutions; and they can foster a conformist mindset rather than a focus on safety. The underlying motivation behind prescriptive requirements is to prevent evasion by avoiding any subjective interpretation in implementation and verification. Violating a requirement can be unequivocally determined through a simple inspection or test. Most safety standards used in the aerospace industry and other "evolving" industries are the result of lessons learned from incidents or developed through gradual technological advancements. On the contrary, there are industries where following past experience is not possible because the system is highly innovative, unique (such as the International Space Station), or safety-critical (for example, nuclear power plants) [9].

2.2.3. Performance standards

A performance standard specifies the required outcome (i.e., the level of safety to be achieved) but leaves the specific measures to achieve it at the discretion of the designer. In this approach, how a performance standard is defined "*a priori*", implemented, and verified "*a posteriori*" is of utmost importance. Performance standards can be qualitative and/or quantitative with reference to the acceptable level of safety. Quantitative performance requirements can be divided into those for which compliance can be demonstrated through prediction (e.g., system failure) and those for which compliance can be demonstrated through measurement (e.g., fine particulate matter in the atmosphere). Qualitative performance requirements are expressed in terms of error and failure tolerance levels. By focusing on results, performance standards offer flexibility to designers and allow them to find the most cost-effective means to meet the requirements. Generally, performance standards can accommodate technological changes and the emergence of new risks associated with new technologies in ways that prescriptive standards cannot. Performance standards can be imprecise

when requirements are too generic or debatable when compliance is evaluated through quantitative predictions (e.g., reliability analysis). Sometimes, the uncertainty in a performance standard is intentional to make it as generic as possible. Proper implementation of performance standards requires training and familiarity within the project team to avoid misinterpretations (either too broad or too narrow) and necessitates conducting risk analyses at the full system level (hardware + software + human). Sometimes, providing guidelines on interpreting the requirements and accepted methods of compliance can assist the design team. In any case, the key concept in implementing a performance standard is that it cannot be directly used for design but requires a risk analysis. In fact, it is through a risk-based design process (iteratively) that detailed design solutions and operational procedures are selected [9].

2.3. Light aircraft standard

The standard applicable to light aircraft are distinguished based on category, maximum takeoff weight, number of passengers, and type of propulsion. Figure 7 presents the main standards developed by the European Union Aviation Safety Agency (EASA).

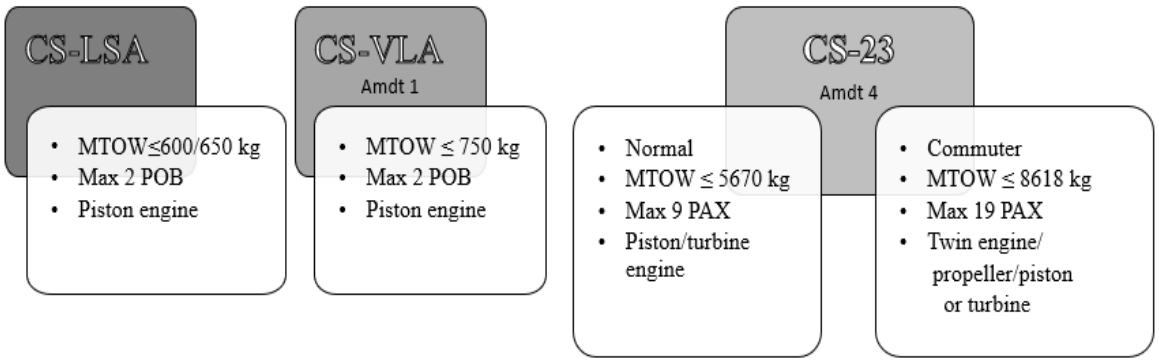

Figure 7 Standard applicable to light aircraft distinguished based on category, maximum takeoff weight, number of passengers, and type of propulsion.

2.3.1. Reorganization of CS-23 and harmonization with Part 23

Over the past two decades, technological and industrial progress has made it possible to develop complex and high-performance aircraft that have become part of the weight range historically designated for light and simple aircraft. In particular, the introduction of high-performance light aircraft has necessitated an update to Part 23, aimed at incorporating more stringent and demanding regulations, often based on the requirements of Part 25, which pertain to much larger transport category airplanes. The unintended result is that some of the stricter and more demanding standards for high-performance aircraft have been applied to the certification of simple and low-performance

aircraft. The emergence of difficulties for those seeking certification for smaller and simpler aircraft led to the initial steps in the United States for the public to request the FAA to reorganize Part 23. The authority, based on criteria related to performance complexity and design, restructured the requirements based on perceived risk, favouring cost reduction and reducing the time burden associated with the certification of small aircraft. Similar needs were recognized in Europe, along with the additional requirement of addressing unnecessary differences in regulatory requirements between CS-23 and Part 23. In this regard, the general aviation industry has repeatedly expressed the high costs associated with dealing with the "unnecessary" differences in airworthiness requirements among various authorities. The breakthrough came when EASA, through the publication of *Notice of Proposed Amendment* (NPA), proposed a reorganization of CS-23 with the intention of achieving long-term harmonization with Part 23, thus promoting collaboration with the FAA and ensuring significant savings for European manufacturers exporting to the United States and *vice versa*. The result was the consolidation and restructuring of CS-VLA and CS-23 into a single CS-23 that covers the applicability of both certification specifications. Prior to Amendment 5, the divisions into aircraft categories, i.e., normal, utility, acrobatic, and commuter, were determined by referencing a combination of factors, including weight, number of passengers, and type of propulsion. This historically was an appropriate method as there was a clear relationship between propulsion, aircraft weight, its performance, and associated complexities. However, technological advancements have altered the dynamics of these relationships and are no longer considered in the new concept.

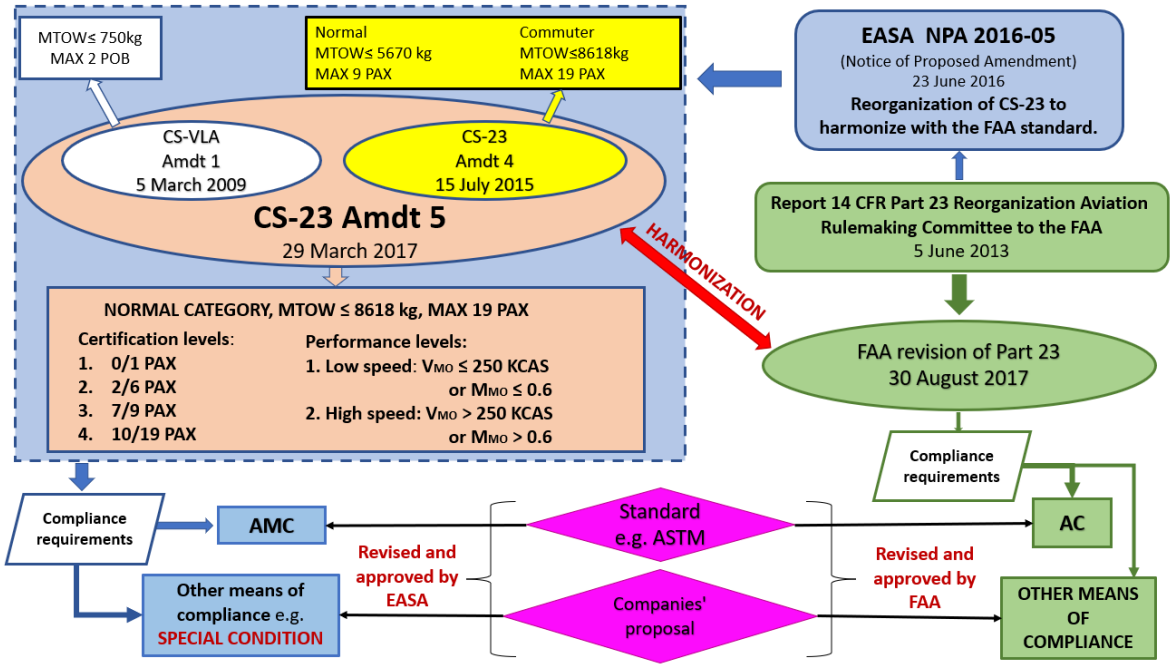

Figure 8 Schematic of the EASA CS-23 update and parallel activities conducted by the FAA.

EASA has retained only a single standard category for all new design approvals of aircraft certified under CS-23. Since weight criteria are considered inappropriate for modern designs, the old categories have been replaced with certification levels ranging from 1 to 4 based on the number of passengers, as it can be seen in Figure 8. Regarding performance, a new definition of "High Speed/Low Speed" has been introduced. The new organization focuses on technical and operational capabilities, with a particular emphasis on technical drivers such as stall speed, visual flight rules (VFR), instrument flight operations (IFR), and pressurization. The authorities believe that transitioning to performance-based standards should significantly reduce or eliminate barriers to innovation and facilitate the introduction of new technologies that enhance safety. Additionally, the new CS-23 concept has a positive economic impact on the aviation industry, requiring fewer administrative resources and consequently leading to a more streamlined and cost-effective certification process.

2.3.2. Means of compliance

In the new CS-23, information is structured differently: if performance and safety objectives are included in Amendment 5 of the same, specific design details and means of compliance, i.e., the methods to be used to meet regulatory requirements, have been relegated to *Acceptable Means of Compliance* (AMC, namely the European version of FAA Advisory Circulars). In summary, through Amendment 5, EASA has shifted much of the prescriptive aspects of the rules into AMC, promoting the introduction of technologies aimed at improving safety and allowing greater options for demonstrating compliance. Moreover, in CS-23.2010 of Amendment 5, it is specified that an applicant can comply with the AMC issued by EASA or can use another means of compliance as long they are accepted by EASA. These "means" can include both consensus standards (such as ASTM, SAE, RTCA, etc.) and procedures developed "*ad hoc*". Regarding consensus standards, industry groups rely on ASTM International as a reliable organization. In the aeronautical sector, reference is made to "*ASTM General Aviation Aircraft F44*". Using ASTM standards is advantageous as it reduces liability risks since these standards are shared with authorities and governments. When the requirements of applicable CS do not contain safety standards or appropriate references to AMC for a particular application or aircraft, there is the possibility of developing a "customized" or "special condition" procedure, simplifying certification tasks for both the applicant and the competent authority.

2.3.3. Special condition

After clarifying the rules and procedures for navigating among various codes and references, it can be shed light on the regulatory framework for the $BK160_{850}$. According to *Subpart A-General*, *CS*

23.2005 Certification of Normal Category Airplane this airplane falls within the category defined by the standardand CS 23 Amdt 5. Indeed, it is a two-seater airplane with a stall speed equal to 45 knots. The scope of this code is quite broad as it encompasses rules for simple aircraft (previously classified under VLA) and those reserved for high-performance aircraft with up to 19 passengers.

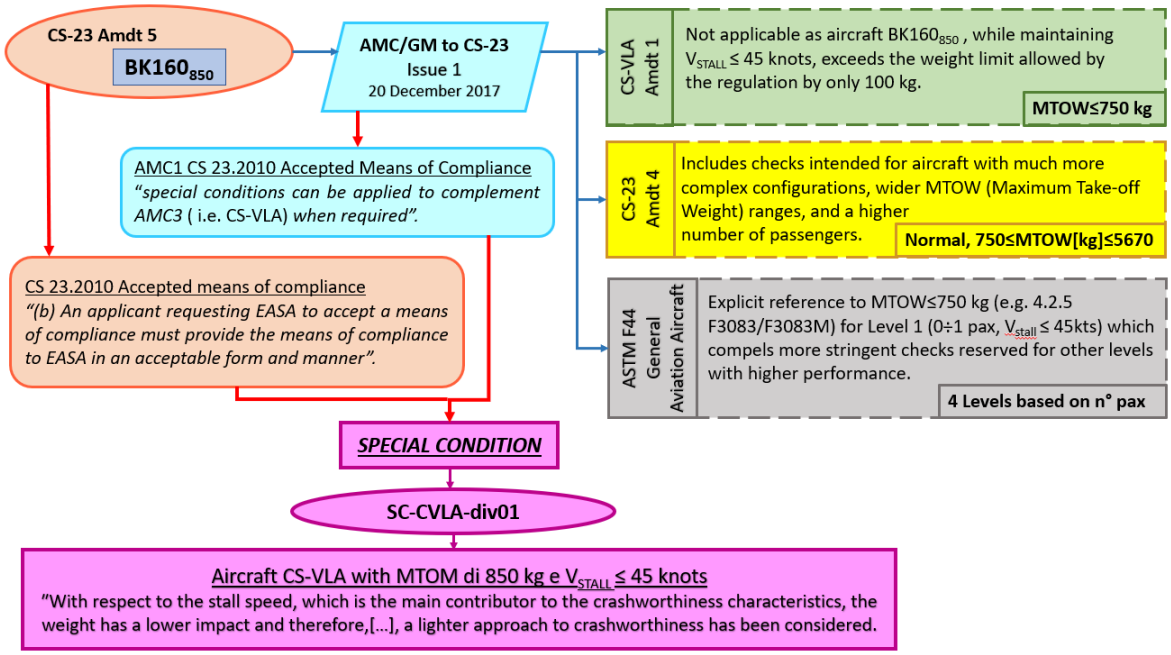

Figure 9 Applicability of certification specifications and means of compliance to the updated configuration of the BK160.

This results in some requirements being excessive and inappropriate for simple and low-performance aircraft like the one discussed in this thesis. Notably, CS-VLA Amendment 1 and CS-23 Amendment 4 have become Acceptable Means of Compliance (AMC) following the approval of Amendment 5 (See AMC/GM to CS-23 Issue1 of December 20, 2017). This raises the issue of the increased weight of the $BK160_{850}$, which, even though 100 kg more, exceeds the applicability limit of the simpler CS-VLA, which has a maximum take-off weight of 750 kg. Complying with Amendment 4 could be a viable option but would involve cumbersome and costly checks. In fact, the standard applies the same safety criteria to an 850 kg, two-seat aircraft with a simple configuration as it does to a 5670 kg aircraft with 9 passenger seats and significantly higher speeds. The turning point lies in the new interpretive approach of EASA and the FAA, which focuses on performance rather than weight, considered an outdated criterion for classifying modern aircraft, which are increasingly high-performing and equipped with lighter structures. This is discussed in EASA's A-NPA 2015-06 (2.1.1.1 The diversity of aeroplane designs), and similar topics have also been proposed by the FAA and presented in detail in AC No. 23-11B. Leveraging what is regulated in section CS-23.2010 *Accepted means of compliance*, Blackshape has formulated its own means of compliance, which,

after EASA's review and approval, has become a Special Condition specifically tailored for the $BK160_{850}$. In this special condition, a less rigid and restrictive approach is proposed compared to CS-23 Amendment 4, while still maintaining a high level of safety appropriate to the category and performance of the aircraft. The presence of a single engine, only two seats, the limited contribution of the 850 kg maximum take-off weight (MTOW) to crashworthiness characteristics, and, most importantly, the stall speed of 45 knots, which matches the limit in CS-VLA, are the key factors determining the level of safety and the applicability of the Special Condition, which serves as a kind of compromise between the two CS categories. A schematic of what has been discussed in this paragraph is presented in Figure 9.

3. Aircraft seat as a safety measure

Aircraft seats are a fundamental component of aviation safety. Seats are primarily designed for passenger comfort but also provide restraint, impact protection, and clear evacuation pathways. They play a critical role in protecting passengers during various phases of flight, especially in the event of unexpected turbulence or an emergency situation. Here's a closer look at how aircraft seats contribute to passenger safety:

- **Restraint System:** the primary safety function of aircraft seats is to provide a restraint system for passengers. This restraint system helps keep passengers securely in their seats, preventing them from being thrown around the cabin in case of turbulence or sudden manoeuvres.
- **Impact Protection:** aircraft seats are designed to absorb and distribute the forces generated during a sudden stop or impact. In the event of a hard landing or a crash, the seat's structure and materials are engineered to minimize the risk of injury to the occupant by absorbing and dispersing energy.
- **Crash-Resistant Features:** modern aircraft seats are equipped with various safety features. These include fire-resistant materials, crash-resistant designs, and emergency lighting. In the event of a fire or impact, these features help protect passengers and provide a clear path to evacuation.
- **Cabin Layout and Safety Regulations:** the placement and design of aircraft seats are subject to strict safety regulations set by aviation authorities. These regulations cover everything from seat spacing to seatback angle to ensure that passengers are protected as effectively as possible.

Airlines and aircraft manufacturers continue to innovate and improve seat designs to enhance passenger protection and overall aviation safety.

In the following paragraphs, with particular reference to small airplanes within the category addressed in this study, the issue of impact and the study of solutions developed to safeguard human health will be introduced. Factors characterizing emergency landing conditions, the kinematics, and the energy-absorption relationships will be disclosed, in order to properly design aircraft seating according to the specific requirements of the considered aircraft class.

3.1. Crashworthiness

Crashworthiness is a critical concept in engineering and design, especially in industries where safety is paramount, such as aviation, automotive, and transportation. It refers to the ability of a structure or system to protect occupants or passengers during a crash, impact, or collision. The term usually refers to the capacity of a structural system to dissipate kinetic impact energy by itself, by means of

a controlled and predictable deformation. Thus, the kinetic energy is transformed into inelastic strain energy, heat, and fracture energy [11].

In this discussion, the focus is on crashworthiness in the aviation industry. Crashworthiness in aviation primarily relates to the design of the aircraft cabin, including the seats, seatbelts, flooring, overhead compartments, and other interior components. These elements are engineered to absorb and dissipate the energy generated during a crash, thereby reducing the forces experienced by passengers. Crashworthy designs incorporate energy-absorbing materials and mechanisms, such as crumple zones in the seat frames or cabin structure. These mechanisms help to slow down and dissipate the energy of an impact, reducing the risk of injury to passengers. Aircraft and their components undergo rigorous testing to ensure they meet crashworthiness standards set by aviation authorities. Crash tests, simulations, and real-world scenarios are used to evaluate how well the aircraft and its interior components protect passengers during various crash scenarios. The aviation industry continually strives to improve crashworthiness standards. Lessons learned from accidents and incidents are used to enhance design and safety features in new aircraft and retrofit older ones. Aviation authorities, such as the Federal Aviation Administration (FAA) in the United States or European Union Aviation Safety Agency (EASA) in Europe, have strict regulations and standards in place to govern crashworthiness. Aircraft manufacturers must adhere to these regulations to certify their aircraft for commercial use, as was already clarified in §2.2.

In summary, crashworthiness in aviation is about designing aircraft and their interior components to protect passengers during unexpected events, such as crashes or hard landings. It involves a combination of engineering, materials science, and testing to ensure that aircraft meet rigorous safety standards and provide the highest level of protection for passengers in emergency situations.

3.2. Basic principles of crash physics

Basic principles of crash physics encompass the fundamental concepts and scientific principles that govern the behavior of objects and systems during a collision or impact. These principles are critical in various fields, including automotive safety, aviation, engineering, and accident investigation. As will be explained in the next paragraphs principal keys of crash physics are the Newton’s laws of motion, energy conservation, impulse-momentum, Hooke’s law. Understanding how materials behave under various forces and the point at which they yield is crucial for crash analysis. Many modern vehicles are designed with crumple zones, areas of the vehicle that deform in a controlled manner during a collision to absorb and dissipate kinetic energy. This reduces the forces experienced by occupants. During a crash, occupants experience deceleration forces that can lead to injury. These forces are often measured in G-forces (acceleration due to gravity), where 1 G is equivalent to the force of gravity at the Earth's surface. In order to design safety systems such as seatbelts, airbags,

and child restraint systems, how the human body responds to impacts, namely human biomechanism, plays a crucial role.

The following sections, taken from the *Small Airplane Crashworthiness Design Guide*[12], will provide an explanation of the invariant relationships among displacement, velocity, and acceleration crucial to understand of how objects and systems behave during impacts and to guide efforts to minimize injuries and fatalities in accidents and collisions.

3.2.1. Kinematics

A large volume of data associated with vehicle accident studies and human tolerance to decelerative loads is presented in the form of time plots of displacement, velocity, and acceleration. The following section will provide an explanation of the invariant relationships among these four quantities. Consider an aircraft impacting a vertical wall as shown in Figure 10.

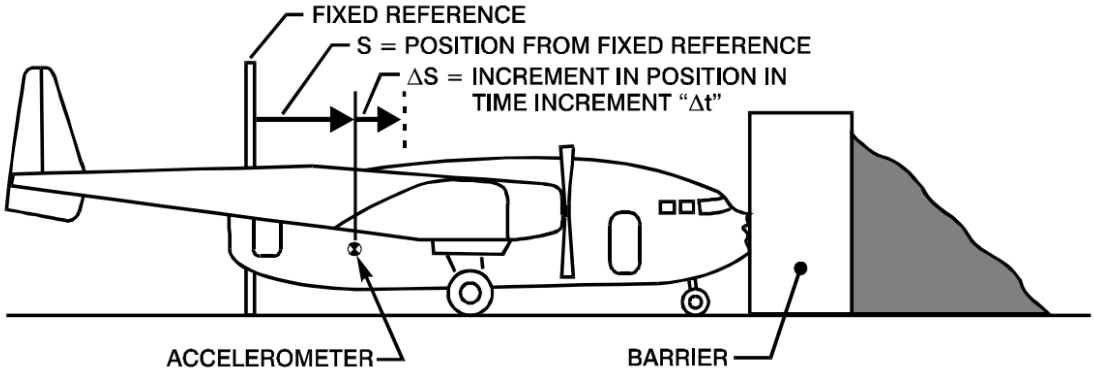

Figure 10 Schematic of an aircraft impacting a vertical wall [12].

If ΔS is the infinitesimal displacement, which occurs in the infinitesimal time interval Δt, then we say by definition that the velocity at the beginning of the time interval is:

$$V = \frac{\Delta S}{\Delta t} \tag{1}$$

Note that the velocity is an instantaneous quantity and has the units of length per unit of time. Similarly, if ΔV is the change in velocity, which occurred in the time interval Δt, then the acceleration at the beginning of the time interval is defined by:

$$a = \frac{\Delta V}{\Delta t} \tag{2}$$

Acceleration is also an instantaneous quantity and has the unit of velocity per unit time. Unfortunately, these mathematical expressions leave much to be desired in the practical interpretation and understanding of these basic quantities. An excellent visual aid to better understanding these

quantities is the velocity-time diagram (Figure 11). This diagram consists of three plots: (1) acceleration versus time, (2) velocity versus time, and (3) displacement versus time [12].

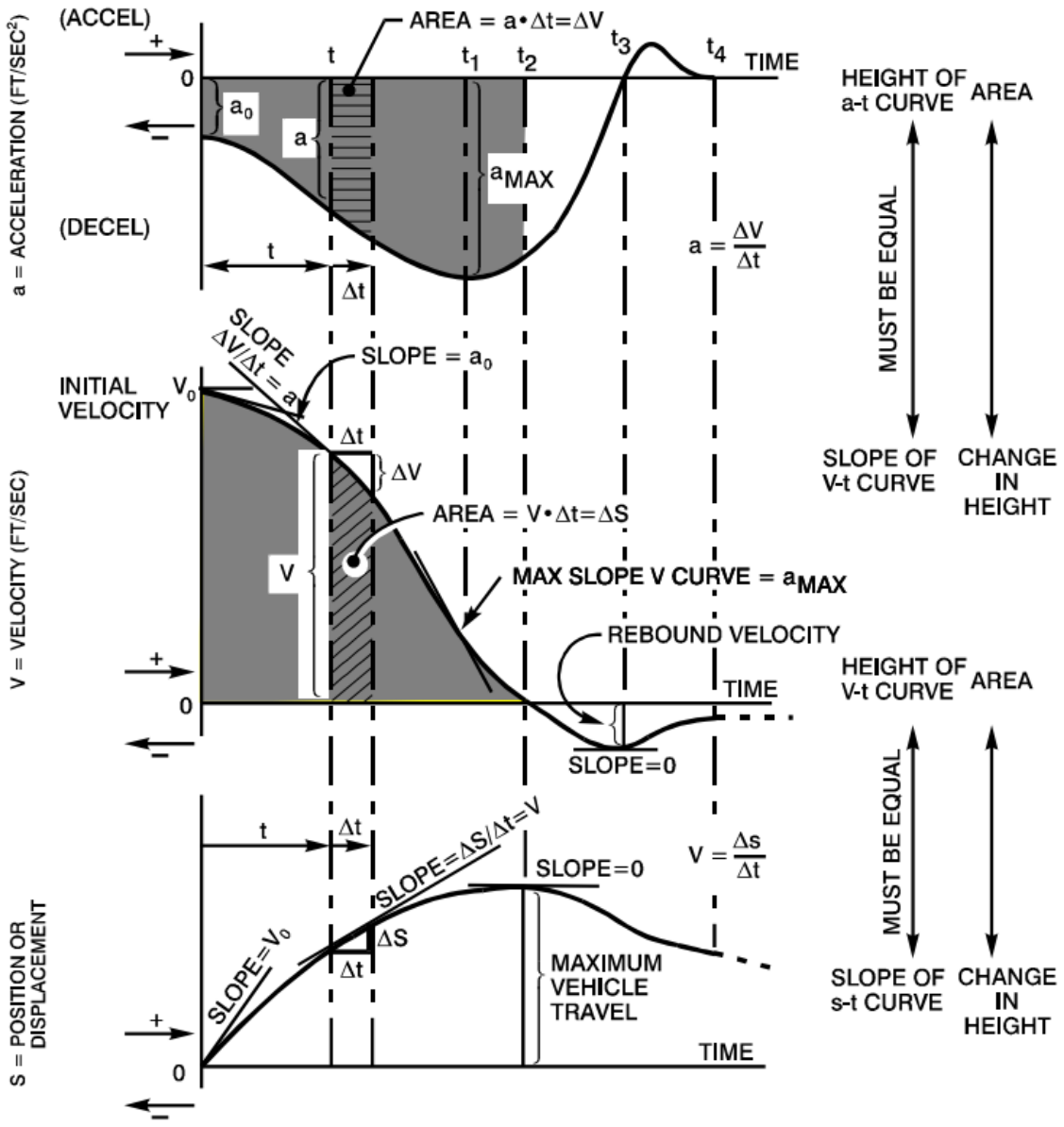

Figure 11 Velocity-time diagram [12].

Observation of Figure 11 reveals that the "a" in Equation 2 is the height of the a-t curve and $\Delta V/\Delta t$ is the slope of the V-t curve. Therefore, the height of the a-t curve is numerically equal to the slope of the V-t curve. This is an invariant relationship and any data, whether experimental or theoretical, must meet this criterion to be valid. Similarly, Equation 1 and Figure 11 illustrate that the height of the V-t curve is equal to the slope of the S-t curve. Through basic algebraic manipulation, two additional invariant relationships can be obtained among these three curves. By rearranging Equation 2, is obtained that the total change in velocity = area under the a-t curve:

$$\sum \Delta V = \sum a \cdot \Delta t \quad (3)$$

In this expression, Σa·Δt represents the area of the horizontally shaded strip in the a-t curve (see Figure 11). The sum of these areas in any time interval is the total area under the a-t curve in the interval. The term ΣΔV is the sum of the successive changes in velocity, which is the total change in velocity in a given interval. Thus, Equation 3, which states that the total change in velocity in a given interval is equal to the area under the a-t curve in the interval, is valid for all situations. This same condition exists between the V-t and S-t curves. By rearranging Equation (1), is obtained that the total change in velocity = area under the V-t curve [12]:

$$\sum \Delta S = \sum V \cdot \Delta t \quad (4)$$

This expression indicates that the maximum vehicle travel, as shown on the lower curve of Figure 11, would have to be equal to the shaded area under the V-t curve.

Other important relationships to note from Figure 11 include:

- the areas below the t axis must be considered to be negative (deceleration), thus giving negative velocity changes or reductions in velocity. When the curve lies above the "t" axis, the area under the axis is positive (acceleration), giving an increase in velocity;
- the velocity is changing at the most rapid rate when the acceleration (or deceleration) is maximum, time "t_1";
- the displacement reaches a maximum when the velocity becomes zero, time "t_2";
- the velocity need not necessarily be zero (time t_2) when the acceleration is maximum (time t_1);
- the area under the deceleration pulse (from t_0 to t_3) is equal to the initial velocity plus the rebound velocity or the total algebraic change in velocity;
- the area under the deceleration curve between t_2 and t_3 is equal to the rebound velocity.

These same relationships can be determined for any set of displacement, velocity, and acceleration curves [12].

3.2.2. Work-Energy Relationship

Designing crashworthy aircraft involves finding ways to absorb the kinetic crash energy within tolerable acceleration levels. Applications include seats, restraint systems, landing gear, and in the aircraft structure itself. As a result, aircraft designers need a thorough understanding of the concepts of energy and energy-absorbing principles. This section will briefly discuss some of the key principles related to work and energy in crash scenarios. The concept of energy arises in the work-

energy principle, which is derived from Newton's Second Law. If the resultant force applied to the mass is "F", as shown in Figure 12, then the force, the mass, and the acceleration are related by Equation 5 [12].

$$F = ma = m\frac{\Delta V}{\Delta t} = m\frac{\Delta V}{\Delta t}\cdot\frac{\Delta S}{\Delta S} = mV\cdot\frac{\Delta V}{\Delta S} \tag{5}$$

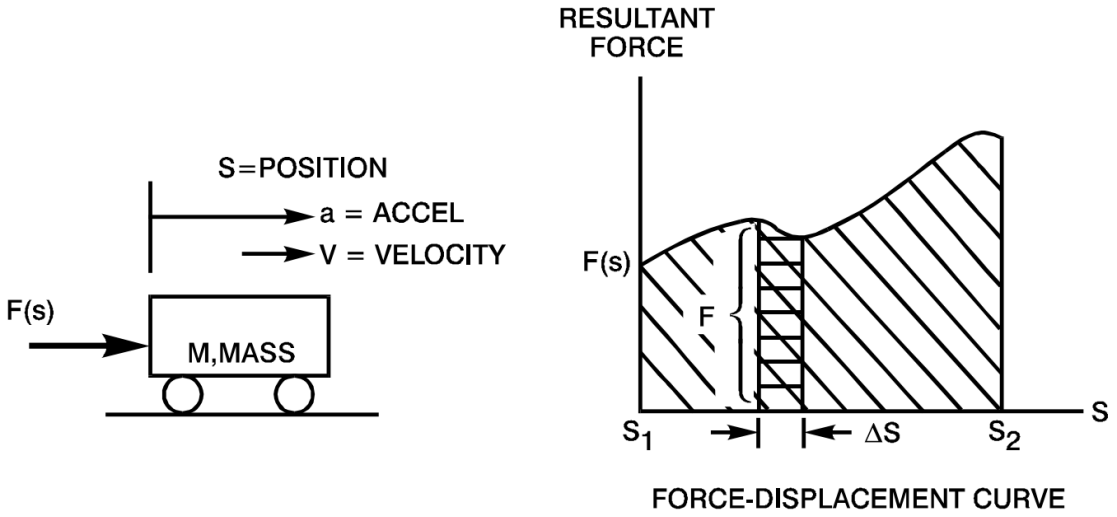

Figure 12 The work-energy principle [12].

The area under the F-S curve is referred to as the system's kinetic energy and is expressed as:

$$\Delta KE = \frac{1}{2}mV_2^2 - \frac{1}{2}mV_1^2 \tag{6}$$

where V_1 and V_2 are respectively the initial and the final velocity of the mass M in Figure 12. The square dependence in Equation 6 is a very powerful consideration in designing for crashworthiness. It indicates that doubling the velocity of a mass quadruples its kinetic energy. But, more subtly, the square dependence indicates that the increase in kinetic energy that is due to an incremental change in velocity depends very strongly on the original velocity to which the increment is added.
The change in kinetic energy, as described by Equation 7, is equivalent to the amount of work done on the mass.

$$\text{Work} = \Delta\text{KE} \tag{7}$$

Work can also be expressed as [12]:

$$W = \Sigma F \cdot \Delta S = area\ sotto\ la\ curva\ F - S. \quad (8)$$

3.2.3. Energy Absorption

The area under the F-S curve in Figure 12 represents the amount of energy absorbed. Equations 7 and 8 indicate that the only way in which energy can be removed from a body (i.e., reducing a body's velocity) is to hold a force on the body as the body moves (Figure 13a). This can be accomplished by the use of a crushable structure or material that maintains a constant force as the mass travels through a certain distance (Figure 13b). A device or system that achieves this objective is referred to as an energy absorber [12].

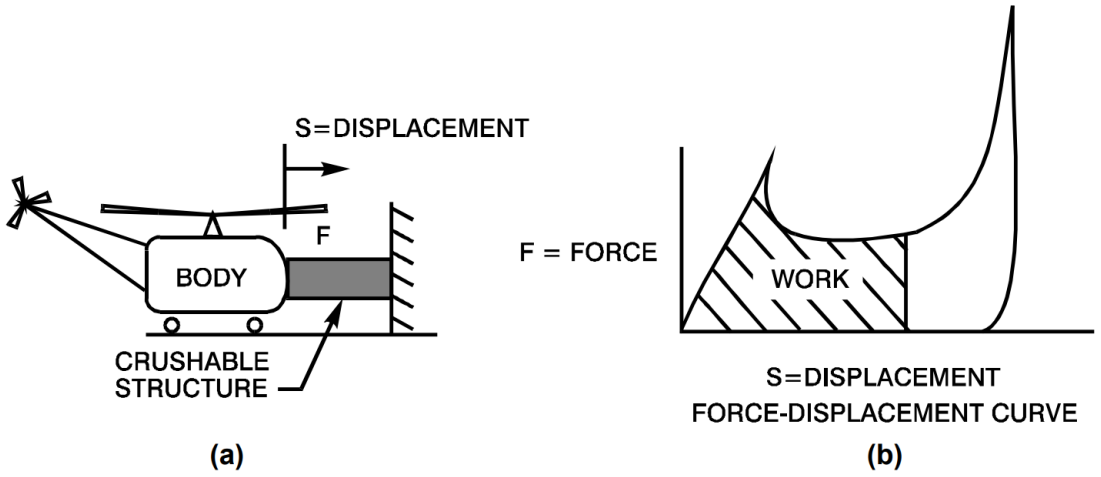

Figure 13 Use of energy absorber [12].

The generation of an "ideal energy absorber" is shown in Figure 14a and b. As shown in Figure 14a, if "a" is constant, the F=ma is also constant. The F-S curve for the energy absorber is represented by Figure 14b. Certain foamed materials and honeycomb materials approach this ideal force-displacement curve to the extent shown in Figure 15 [12].

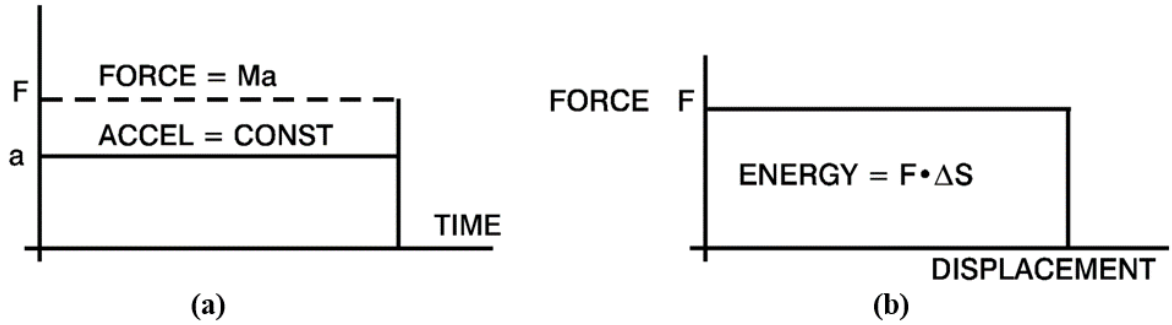

Figure 14 a) Relationship between constant acceleration and constant force, b) ideal energy absorber [12].

As previously mentioned, the area under the force-displacement curve (Figure 15b) represents the amount of energy absorbed. This area can be divided into three separate regions: elastic, plastic, and

rebound. If loading increases only up to Point A in Figure 15b, then unloading generally occurs along the elastic curve 0A, and the energy indicated by Area "1" is given back, in the same manner as a spring gives back its energy when it is unloaded. Area "2" represents plastic energy absorption. If loading reaches Point C in the figure, the energy corresponding to Areas "1" and "2" plus Area "3" is absorbed. However, as unloading occurs, the energy of Area "3" is given back in the form of rebound. Loading in the region from B to C in the figure is often referred to as "bottoming out," a condition wherein the deforming structure or material has become completely compacted and the load increases rapidly with very little increased deformation [12].

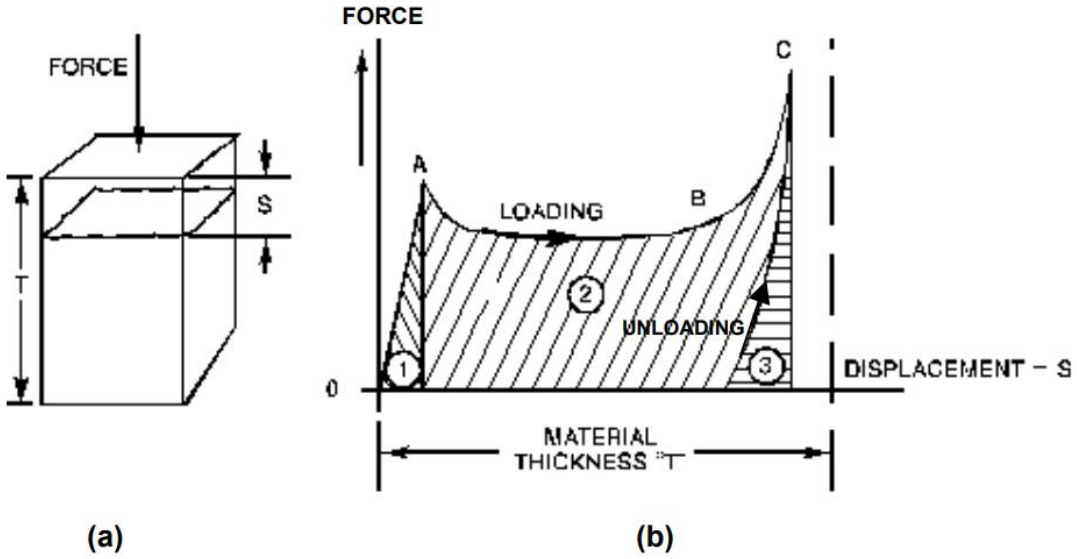

Figure 15 Force-displacement curve for honeycomb materials [12].

3.2.4. Design Crash Impact Conditions

This subsection presents the impact conditions that should be used in the design of Advanced General Aviation Transport Experiments (AGATE) Alliance – class airplanes. The current requirements for the impact conditions used to design aircraft occupant protection systems are located in 14 CFR Part 23 and CS 23 Amdt 4, Subpart C - Structure; specifically, in Section 23.561 "General" and in Section 23.562 "Emergency Landing Dynamic Conditions". The regulations mainly address the strength and performance of seat/restraint systems, although some consideration is given to the occupant's immediate surroundings and to the strength of the fuselage. The impact conditions in the regulations are based on crash research and accident investigation studies conducted by the FAA, NASA, and the NTSB from as far back as the 1950's. Except for adjustments in the static loads and vertical dynamic test conditions for airplanes with stall speeds greater than 61 kts, the static and dynamic regulatory impact conditions assume that all airplanes respond similarly in a crash. In other words,

the current regulations presume all airplanes crash such that the loads, accelerations, and velocity changes are the same. This assumption is clearly a simplification and emphasizes that the CFR's and CS' are minimum performance standards. The impact conditions are presented here in Table 1 and Figure 16, and were used in the design of a crashworthy test airplane and in the full-scale crash test of that airplane conducted by the AGATE ACG in the summer of 2001 [12].

Table 1 AGATE-determined impact conditions [12] .

Impact Velocity	V_{so}
Impact Angle	-30 deg (down)
Attitude	MTOW consisting of: • A 170-lb occupant in each seat • Fuel up to MTOW or capacity • Baggage up to MTOW, if fuel is at capacity (Other scenarios may be used if they can be justified, e.g., seats designed with restricted occupant weight should be tested at the maximum restricted weight)
Impact Surfaces	Hard (concrete) Soil (Defining parameters TBD)

It should be noted that the AGATE impact conditions are for the whole airplane and take into account the stall speed (that is, the vehicle's minimum operating speed) and weight of the airplane. These whole-airplane conditions acknowledge that different airplane designs will have different initial crash conditions based on the performance and size of the airplane. These conditions also do not presume the structural response of the airplane; the structural response is defined by the crashworthiness of the design and the ingenuity of the designer. The two different impact surfaces specified recognize that the impact surface also influences the airplane response. At 30 deg nose down, the hard-surface impact typically produces sliding impact with deformation in the lower nose structure and sometimes the front-seat footwells, a whole airplane pitch-up rotation that aligns the airplane with the impact surface, and a higher vertical (relative to the airplane) component of acceleration. The hard-surface condition forces the designer to address energy absorption primarily in the subfloor structures and also, to a certain extent, in the nose of the airplane; the designer is also induced to address the strength of the lower forward occupant compartment, and the bending strength of the fuselage. An impact on soil at 30 deg nose down produces a very different response. For airplanes that are not designed to be crashworthy, the airplane structure will typically dig into the soil, stopping abruptly, thereby producing a very high longitudinal (relative to the airplane) deceleration. The soil-impact condition forces the designer to address energy absorption primarily in

the nose or engine mount, the longitudinal strength of the occupant compartment and firewall, and the use of anti-plowing features. Based on the data compiled during the AGATE study, the average impact velocity and the angle at which at least one occupant survived and at least one occupant was fatally injured was 71 kts and 31 deg. Comparing the results from the AGATE study to the design pulses recommended in the 1967 Crash Survival Design Guide required calculating the longitudinal and vertical changes in velocities from the average impact conditions of 71 kts and 31 deg [12].

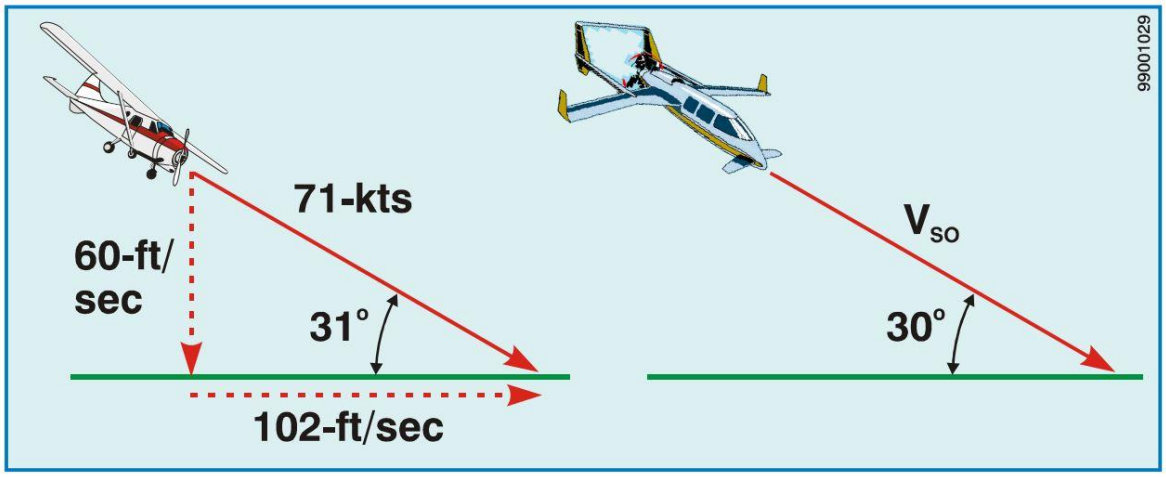

Figure 16 AGATE-determined impact conditions

3.2.5. Energy Content of Aircraft at Impact

The total energy that the complete aircraft system possesses immediately prior to impact is the sum of several energy terms. This energy includes the following:

• translational kinetic energy, $(K.E.)_T$;

• rotational kinetic energy, $(K.E.)_R$;

• potential energy, P.E.;

• strain energy, S.E.

The total energy input during the crash sequence, T.E., is:

$$T.E. = (K.E.)_T + (K.E.)_R + P.E. + S.E. \quad (9)$$

This is this total energy which must be absorbed or dissipated in the crash sequence. Follows a detailed examination of the mentioned quantities:

- the Translational Kinetic Energy, $(K.E.)_T$, component is a direct function of the aircraft mass and the velocity of the mass center at impact. If:

  M = the aircraft mass;

V = resultant velocity of the mass center;

V_X = longitudinal component of velocity;

V_Y = lateral component of velocity;

V_Z = vertical component of velocity;

then:

$$(\text{K.E.})\text{T} = 0.5 * \text{MV}^2$$
$$(\text{K.E.})\text{T} = 0.5 * \text{M}(V_X^2 + V_Y^2 + V_Z^2) \quad (10)$$

Thus, the total kinetic energy of the aircraft is the summation of the kinetic energy for all mass elements of the aircraft. Generally, the translational kinetic energy, or $(\text{K.E.})_T$, will be the predominant contribution to the total energy content of the aircraft [12].

- The Rotational kinetic energy, $(\text{K.E.})_R$, may be associated with the total aircraft and with aircraft elements such as the engine(s) and propeller(s). Selective assessment of rotational kinetic energy contributions to the crash energy balance must be made. In general, rotational kinetic energy is calculated using the expression:

$$(K.E.)_R = 0.5 * I_\theta \varpi_\theta^2 + 0.5 * I_\phi \varpi_\phi^2 + 0.5 * I_\psi \varpi_\psi^2 \quad (11)$$

Where:

ϖ_θ = angular velocity component in the X-Z plane (pitch);

ϖ_ϕ = angular velocity component in the Y-Z plane (roll);

ϖ_ψ = angular velocity component in the x-y plane (yaw).

While I_θ, I_ϕ e I_ψ are the mass moments of inertia of the vehicle with respect to the pitch, roll, and yaw axes, respectively, at its mass center [12].

- For the crash sequence, the total potential energy (P.E.) input into the system equals the summation of the vertical displacement (ΔZ) contribution of each mass (belonging to the aircraft) from the instant of first contact until the time of completion [12].

$$\text{P.E.} = \Sigma(\text{mg}\Delta Z) \quad (12)$$

- Structural strain energy (S.E.) may exist due to in-flight loading. One example of strain energy is the upward bending of the aircraft's wings due to lift loading. This energy is released quickly upon contact with the ground and the resulting rapid loss of forward velocity. In addition, pressurized systems may have stored strain energy. However, stored strain energy due to pressurization is usually insignificant to the crash event [12].

3.3. Aircraft Seat Structural Design

Aircraft seats play a crucial role in crashworthiness. They are constructed with materials and structures that can withstand the forces of a crash. The seat's ability to restrain passengers and minimize injury is a key aspect of their design. Seats must accommodate a range of occupant sizes, both male and female, be designed to withstand crash loads, provide comfort, and be lightweight. The following paragraphs, taken from the *Small Airplane Crashworthiness Design Guide* [12] will focus on various feasible solutions for absorbing vertical energy generated in an impact, which is the primary subject of interest for the purpose of this thesis work.

3.3.1. Vertical Energy Absorption Solutions

Since human can better withstand impacts in the forward (X) and lateral (Y) directions rather than vertical (Z) ones, it has been concluded that limiting the load along Z leads to minimizing potential spinal damage, significantly increasing the occupants' chances of survival. Various devices have been proposed, tested, and developed to dissipate energy and limit loads. It is known that applying a force over a specific distance allows for the absorption of kinetic energy from a moving mass. Therefore, the longer the distance over which force can act, the lower the load transmitted to the mass. In aircraft, energy absorption mechanisms that transfer stopping forces to the occupant must limit the loads to tolerable values for human health and safety. Over the years, it has been demonstrated that plastic deformation of materials, primarily metals, is reasonably efficient for energy absorption. Overall, these devices are designed to:

- Efficiently decelerate the occupant while keeping load conditions within human tolerance limits.
- Withstand loads in the opposite direction of travel (rebound) or achieve equivalent deformation performance in both load directions, i.e., anti-rebound.
- Be cost-effective, lighter, and as compact as possible.
- Be reliable and durable for the entire lifespan of the aircraft, ensuring a lifespan of at least 10 years or 8,000 flight hours without requiring maintenance.
- Not be affected by vibrations, dust, dirt, heat, cold, or other environmental factors, including corrosion.

Among the solutions developed to meet the crashworthiness criteria, there are those proposed below.

- Guided-Stroke seat: Figure 17 shows a schematic representation of a guided-stroking seat. The guided stroke is often provided through a set of linear bearings attached to the seat bucket, and a pair of guide tubes attached to the aircraft structure (or to a frame that is attached to aircraft structure). One advantageous crashworthy feature of this particular design that is the restraint can be anchored directly onto the seat bucket, thereby maintaining optimum restraint geometry

during full seat stroke. In addition, since the seat stroke is guided, the occupant's forward motion can be well controlled, even during high stroking distances or high longitudinal loads. The guided-stroke design concept is often used for military helicopter seats, where the stroking distance can exceed 12 in [12].

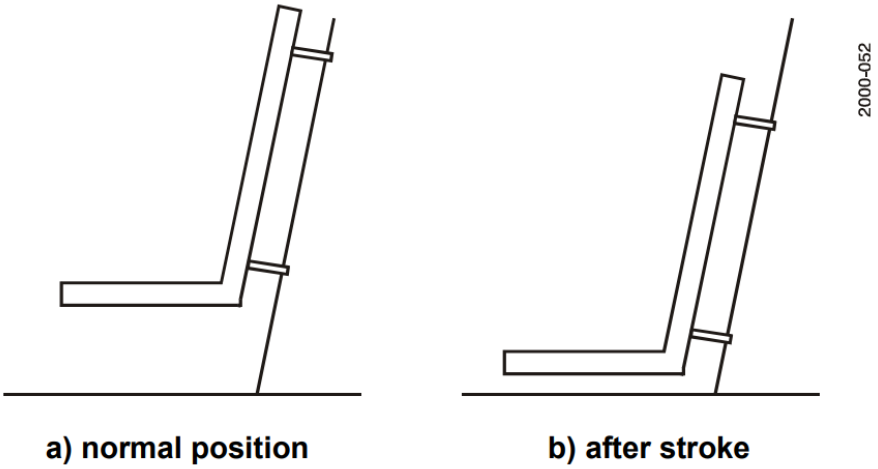

Figure 17 Schematic for a guided-stroke energy-absorber design [12].

- Deformable Seat Structure: for this concept, a carefully designed deformable seat structure is typically located under the seat pan, as shown in Figure 18. This concept utilizes plastic structural deformation to limit the vertical load. This particular seat concept is commonly referred to as the "S"-leg seat, named after the shape of the deformable structure. However, the deformable structure can be formed in various shapes to provide the best combination of vertical load attenuation and longitudinal retention. One of the challenges of this design is to provide a structure that deforms vertically at a relatively low and constant load, but still provides tightly limited longitudinal deformation [12].

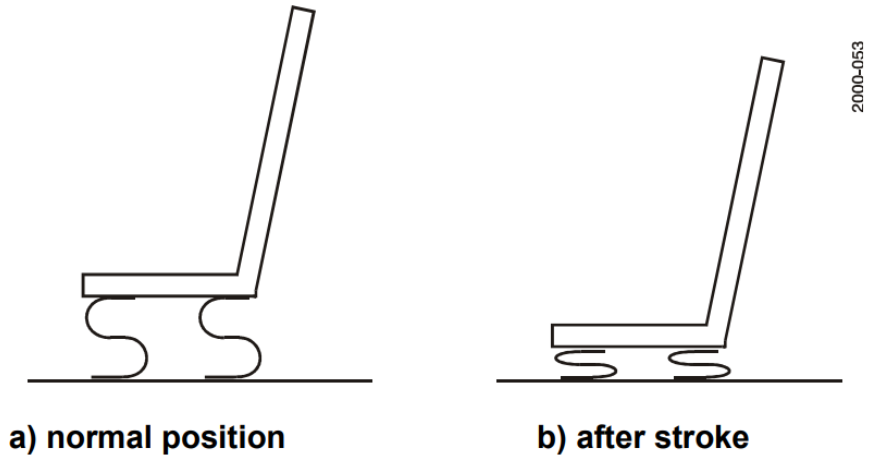

Figure 18 Schematic for a deformable seat structure energy-absorber design [12].

- Pivoting Seat Pan: for this concept, a hinge point is located near the front of the seat pan, and the back of the pan deforms downward, as shown in Figure 19. The seat back is normally attached to a bulkhead. This type of design has been incorporated into some commercial helicopter seats. The main challenge of this design is to maintain proper restraint geometry as the seat pan pivots.

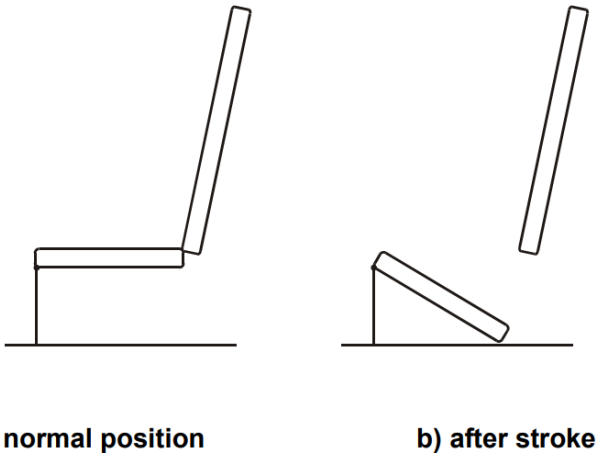

Figure 19 Schematic for a pivoting seat pan energy-absorber design [12].

- Crushing Seat Pan: this design concept is shown in Figure 20, and is also referred to as an energy-absorbing seat pan cushion. This design concept uses a crushing material located directly under the seat pan surface. The seat pan needs to be designed to distribute the load to the energy absorber crushable material, and to prevent damage to the energy absorber material under normal use (i.e., stepping on the cushion with hard heels). Since most crushing materials will not hold high shear loads after crushing, the restraint will most likely need to be anchored to aircraft structure. Thus, it is difficult to maintain the optimal lap belt restraint geometry as the seat pan strokes. For this reason, **this design concept should only be utilized when minimal vertical**

stroke is required. One advantage of this design is there is minimal stroking mass, so dynamic overshoot will be minimized [12].

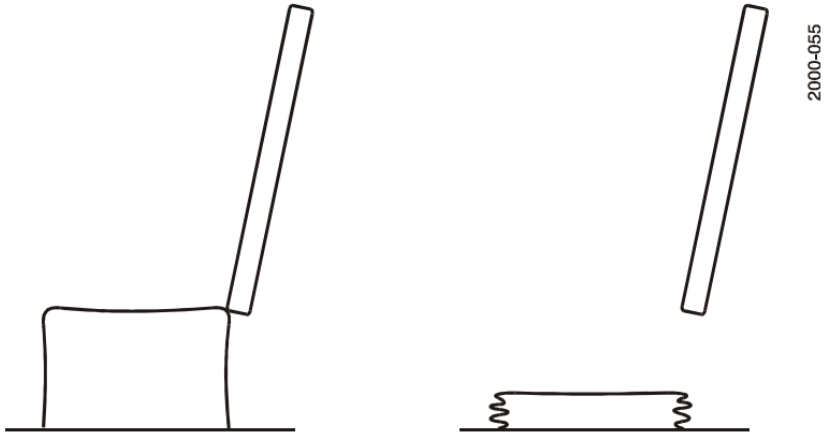

Figure 20 Schematic for a crushing-seat-pan energy-absorber design [12].

In conclusion, the seat must be designed to provide the maximum amount of vertical stroke within the aircraft structure's boundaries. The amount of seat stroke and the required amount of absorbed energy to limit the load on occupants are based on various factors, including:

- type of deceleration pulse (frequency, magnitude, and duration);
- total velocity change;
- energy absorber load profile;
- seat travel direction relative to the acceleration caused by the impact;
- seat travel angle relative to the occupant's seating angle;
- seat mass;
- occupant mass;
- seat cushion design;
- geometry of the entire seating apparatus.

Calculating seat stroke and defining the load that must be absorbed can be complex, requiring experience of the designer constructing the model. Depending on the aircraft class, if required by regulations, dynamic testing is indispensable for optimal design development and validation.

3.3.2. Seat Cushion

The seat bottom and seat back with which the occupant is in constant contact should be designed for comfort and durability. Well-designed cushions should provide comfort for the occupant, as well as complement the crashworthiness of the seat. The seat bottom cushion can have a significant effect on the comfort and crashworthiness of the seat. The problem is one of developing a compromise design that will provide both comfort and safety. In general, comfort is provided by providing

relatively thick and soft foam cushions, which distribute the load and decrease localized point loading. However, an excessively thick/soft cushion can promote dynamic overshoot during a high vertical acceleration crash, thus increasing the occupant's spinal load. In addition, a thick/soft cushion may not assist in providing the occupant lower torso with longitudinal restraint. A design approach that has been successfully employed is a contoured cushion, which approximates the shape of the occupant's buttocks. Thus, the cushion thickness can be reduced with minimal effect on comfort. The contour can be provided by the seat pan structure (recommended) or by an insert between the seat pan and the soft cushion material. To minimize dynamic overshoot, the compressed cushion thickness under the buttocks (specifically, the ischial tuberosities) should be no more than 0.75 in. thick. Thicker cushioning can be provided in the occupant thigh region to accommodate various thigh angles, especially for crewmembers who operate the rudder pedals of the aircraft. Use of rate-sensitive foams has also demonstrated increased crashworthiness and comfort. In general, rate-sensitive foams will deform slowly to accommodate comfort, but "stiffen" during high compression rates. This rate-sensitive stiffening helps to couple the occupant to the seat energy-absorbing system and reduces dynamic overshoot. However, rate-sensitive foams are generally more dense and less durable than conventional polyurethane foams. The seat bottom cushion can also be designed as a floatation device. This is normally accomplished by providing a layer of semi-rigid closed-cell foam under the comfort cushion. This layer can double as the contoured interface between the seat pan and the occupant's buttock contour.

In summary, the seat cushion should be used to attenuate the load on the pelvic and lumbar areas. For light aircraft, starting from the aircraft class of more than 780 kg, concerning dynamic requirements, it is essential to follow the approach of CS 23.562 Amdt 4 or equivalent FAR. Materials that disintegrate or compact to allow energy dissipation must be used. The sole use of a cushion as a device for energy absorption, as is the case with a rigid seat (e.g., the seat of the BK 160 aircraft), is justified when both the available vertical travel and the dynamic overshoot to be dampened are minimal. In general, if possible, it is preferred to avoid relying solely on the cushion for energy absorption, also because foam performance can vary depending on the aircraft's operating temperature.

3.4. Emergency landing conditions

Emergency landing conditions refer to the circumstances and situations in which an aircraft may be forced to perform a landing outside of a designated airport or landing strip due to unforeseen events or emergencies. These conditions can vary widely and can result from a range of factors, including mechanical failures, adverse weather, medical emergencies, or other critical situations. In all these situations, the primary goal of an emergency landing is to ensure the safety and well-being of passengers and crew members. Emergency landings happen during takeoff and landing (in Figure 21

which shows the generic flight's phases), critical phases of a flight when the aircraft is closer to the ground, and there are generally higher chances of survival compared to emergencies at higher altitudes. This explains why forces and accelerations are calculated in the conditions already seen in §3.2.4.

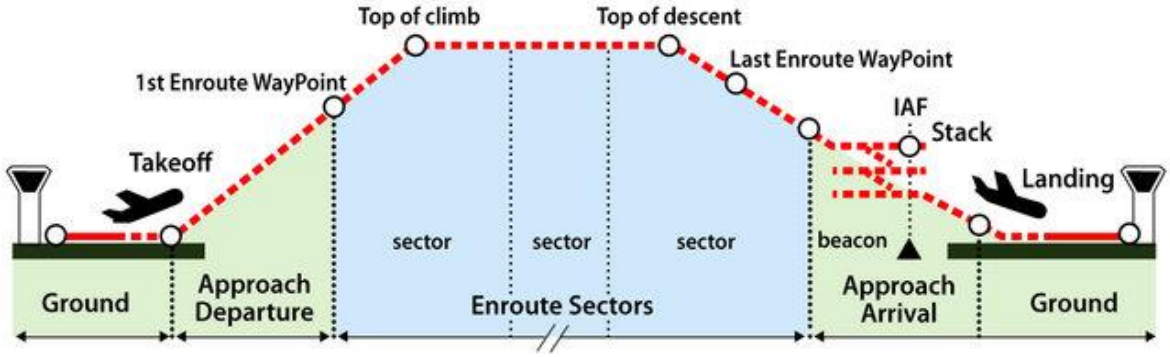

Figure 21 Schematic of phases of flight [13].

Considering the purpose of this study, the effectiveness of an aircraft seat is evaluated through dynamic tests, specifically designed by aviation authorities to quantify the load on the pelvic and lumbar regions using anthropomorphic test dummies (ATDs) positioned on the seats and equipped with proper sensors. These tests, essential for developing the correct design, are clearly expensive both in terms of experimental equipment and because the seats and other elements are deformed by the test loads and must be replaced after each test. Currently, the FAA (Federal Aviation Administration) and EASA (European Union Aviation Safety Agency) in the section related to "*Dynamic Emergency Landing Conditions*" (FAR 23.562 and CS 23.562) specify that, in the event of an emergency landing, the lumbar load measured between the pelvic and lumbar region should not exceed 1,500 lb (680 kg). Preserving the spinal column is of fundamental importance as it protects the spinal cord, provides support and structure to the body, and enables the movement of the head, neck, and chest. Section 23.562 of CS and FAR specifies impact conditions, test procedures, and human tolerance criteria that must be used for the design and testing of the seat and restraint system to demonstrate that the occupant will be protected during an emergency landing.

Dynamic tests are conducted with specialized anthropomorphic test dummies (ATDs) designed to simulate the presence of the occupant. They are equipped with measurement sensors to quantify the actual applied loads and verify that they do not exceed the prescribed limits for human safety. The regulations require the execution of two tests, which will be explained in the following paragraphs. The first, commonly referred to as "*Test 1*," simulates an emergency landing with predominantly vertical impact. The second test, commonly referred to as "*Test 2*", simulates an emergency landing with predominantly horizontal impact.

3.4.1. Emergency landing dynamic conditions "Test 1"

Test 1, referred to as the "down test", determines the protection provided when the crash environment is such that the crash impact load component is directed along the spinal column of the seat occupant, in combination with a forward component.

Table 2 Dynamic Test Requirements for CS 23.

TEST 1	CS 23	TEST 2	CS 23
Min velocity (m/sec)	9.5	Min velocity (m/sec)	12.8
Max time to peak (sec)	0.05/0.06	Max time to peak (sec)	0.05/0.06
Peak Deceleration (G's)	19/15	Peak Deceleration (G's)	26/21
Seat pitch angle (deg)	30	Seat pitch angle (deg)	N/A
Seat yaw angle (deg)	N/A	Seat yaw angle (deg)	10
Roll (deg)	0	Roll (deg)	10
Pitch (deg)	0	Pitch (deg)	10

The test sled fixture used to conduct *Test 1* is illustrated in Figure 22. By changing the direction of the velocity vector, this test can also be conducted on a drop tower, as shown in Figure 23 [12]. The testing requirements to comply with FAR or CS 23 are displayed in Table 2. The CS 23 Amendment 4 regulations and the related AMC (Acceptable Means of Compliance) provide all the details regarding the execution of experimental tests.

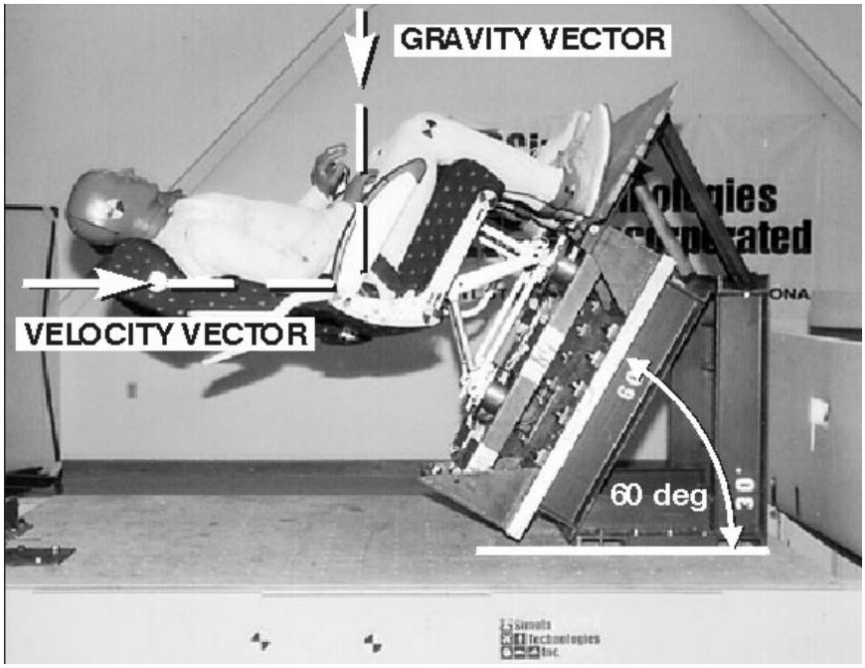

Figure 22 Dynamic Impact Test 1: As conducted on a horizontal sled, with the seat positioned 60-deg above horizontal [12].

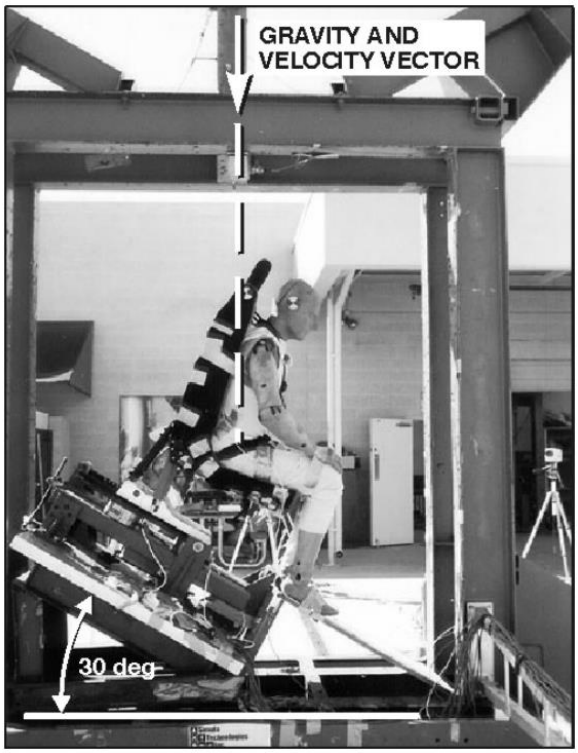

Figure 23 Dynamic Impact Test 1: As conducted on a drop tower with the seat tilted 30-deg nose-down [12].

3.4.2. Emergency landing dynamic conditions "Test 2"

Test 2, referred to as the "sled test," determines the protection provided when the crash environment is such that the crash impact load is in the longitudinal direction, with a lateral component. The sled test fixture used to conduct Test 2 is illustrated in Figure 24 [12].

The seat/restraint system apparatus and occupants are once again oriented in their normal position relative to the aircraft and rotated with a yaw of 10 degrees from the horizontal impact vector. In practice, by misaligning the test sled tracks by 10 degrees, the condition of a deformed floor is created in order to achieve the condition of the highest load on the shoulder harness and verify the likelihood of head impacts. The testing requirements to comply with FAR or CS 23 are displayed in Table 2.

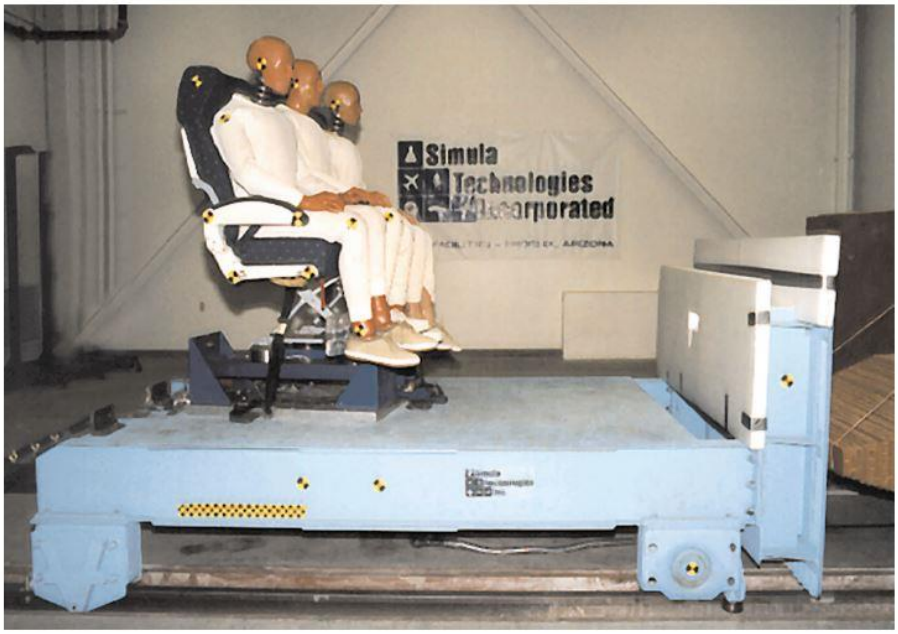

Figure 24 Dynamic Impact Test 2: Longitudinal sled test [12].

3.4.3. Occupant Injury Criteria

In aviation safety, the term "*Occupant Injury Criteria*" refers to the specific standards and criteria used to assess and mitigate the risk of injury to occupants of an aircraft during emergency landings. These criteria are crucial in the design, testing, and certification of aircraft seats and restraint systems to ensure the safety of passengers and crew in the event of an accident. The 14 CFR 23.562 as well as CS 23.562 refers to a section that outlines the requirements for dynamic testing of seats and restraint systems during emergency landings. It is a key regulation that sets the standards for occupant injury criteria in small transport category airplanes. These criteria are primarily related to the loads experienced by the occupants, particularly in the lumbar and pelvic regions, but also for head and chest, as it can be seen in Table 3. The criteria take into account human tolerance levels to various loads and accelerations. These levels are determined through extensive research and testing to

establish the maximum forces that the human body can withstand without sustaining severe injuries. The criteria specified in these regulations, as was said in the airworthiness section (§ 2.2) are not static. They are subject to ongoing research and development to improve occupant safety. As technology advances and more data becomes available, the criteria may be updated to reflect the latest safety standards.

Table 3 Occupant Injury Criteria Specified in 14 CFR 23.562 and CS 23 Amdt 4 [12].

Description	Injury Criteria	Instrumentation
HIC (Head Injury Criterion)	1,000	Triaxial linear accelerometer installed at the c.g. of the ATD's head
Shoulder harness strap loads	7787 N for single straps; 8900 N for dual straps.	Load cell(s) attached directly to the shoulder harness straps
Lumbar compression load	6675 N	Load cell installed between the lumbar spine and pelvis
Abdominal lap belt loading	Lap belt must remain on ATD's pelvis	None required

4. SEAT CUSHION MATERIAL PERFORMANCE EVALUATION

Aircraft seat cushion evaluation is a multifaceted process that encompasses safety, fire resistance, crashworthiness, comfort, durability, material selection, and regulatory compliance. The goal is to provide passengers with a safe and comfortable flying experience while meeting strict safety standards.

In the following paragraphs, the experimental activity for the mechanical characterization will be detailed, which was conducted to obtain the tensile, shear and cyclic compression characteristics of the materials chosen for the seat cushion. Color maps obtained by DIC have highlighted a potential auxetic behavior of these ordinary foams. To investigate this phenomenon a comprehensive study has been conducted from both an experimental and numerical perspective. This part of the study is essential for deriving the properties and performance of the selected materials, which can then be implemented in numerical models. For the seat, soft open-cell polyurethane foams containing fire-resistant graphite particles were selected, ensuring compliance with the flammability requirements specified in CS-23.853. Given the nature of these materials, the measurement technique used during the tests, namely Digital Image Correlation (DIC) [14], also holds value for the research activity. It is indeed known that traditional measurement techniques (i.e., strain gauges) cannot be used on soft materials. This and other issues will be addressed in the following paragraphs, based on the research activities conducted by Casavola et al. [15–17].

4.1. Polyurethane foams: an innovative full-field measurement approach

Polyurethane (PU) is a versatile material that can be used for different engineering applications: civil construction, marine, air and land transportation, thermal insulation and textiles industry [18]. The peculiarity of this material, mainly commercialized as a foam [19], consists of a good energy absorption capability combined with its lightweight. Foams, indeed, are widely used as energy absorbing devices in automotive and aeronautical industry to prevent injuries to the occupants, as well as in packaging industry to protect fragile objects from damages when subjected to a crash [20–23]. Soft polyurethane foams, required for the crashworthiness design, must comply with stringent regulatory requirements aimed to human health safety and requiring, for this purpose, the use of flame-retardant components for surfaces in contact with the human body.

Based on these premises, in this study a particular foam containing expanded graphite has been developed and its mechanical characteristics are analyzed. Common foams consist of two phases, a solid material and a fluid-filled cellular porous structure. Polyurethane foams, instead, can be found in different combinations and many factors influence their property, like: the rigid or soft nature of

the base material, the morphological structure of the cell walls, the fact that they can be open or closed and the nature of the fluid inside contained [24–27]. All these features allow analyzing the material at several hierarchical scales: a macro-scale level, corresponding to the entire specimen, a meso-scale level, which is related to the only several pores and, finally, a micro-scale level in which single struts are analyzed [28]. The present study focuses on the macro behavior of low density soft open-cell polyurethane foams. The extremely soft nature of this material reduces the list of techniques to be used to observe its deformation in terms of strains. For example, the use of extensometers should be excluded because they cannot be directly applied on the material as they would deform it. To this purpose, Daniel and Cho [29] tucked a semi-rigid polymeric foam between two metal plates, cut ad hoc according to the different tests (tensile, shear and compression), with the extensometers applied on the metal plates. However, also in this case, the available strain range is often not sufficient to cover the entire measurement due to very large deformations of the foam specimens. Nevertheless, it must be noticed that this kind of measurement gives an overall information about the strain experienced by the material that, for such complicated structures, results to be poorly representative of its complete mechanical behavior. Many authors in the past considered the displacement of the testing machine actuator [30–36], anyway it can be not considered as the best solution. In fact, it is proven that strains deriving from crosshead displacement lead to gross underestimation of the elastic modules [37]. Other authors [38] tried to quantify the compressive response of a low-density soft PU foam using a laser extensometer, but above a given level of deformation, exceeding the extensometer measurement range, they had to rely on piston displacement measurements.

Some difficulties can be overcome by using full-field strain measurement methods. Digital image correlation (DIC) is a non-contact, non-destructive method which provides high-accuracy deformation measurement from a microscopic level [39] to a macroscopic one [40]. This method is implemented by painting a random pattern on the surface of the specimen. This pattern is imaged at different times during the test. Then, the correlation between subsets of two images recorded at two different stages of the specimen's load history is studied and, given a preliminary set-up calibration, the field of displacements of the analyzed surface can be determined [41].

As the DIC application on foams is concerned, according to the nature of the material and to the characteristics to be identified, in addition to 2D-DIC analysed in this study, also studies based on 3D-DIC [42–44] and digital volume correlation (DVC) [28,45,46] may be found. Basically, if the 2D DIC provides the in-plane displacement and deformation information's, 3D-DIC also allows to detect the out of plane components or allows to know the shape of a body. Many of the works in literature were carried out on rigid foams, such as the successful comparison of the results obtained from strain gages and DIC [47], the nonlinear response under compressive loading of hard open-cell PU foam

used for protection helmet shell [48], the response analysis of metal/polymer hybrid foams [49], the comparison of the compressive mechanical properties of Al foam-polymer composites to Al foam without any polymer [50].

Although DIC on rigid materials shows an excellent ability to measure deformations, the same cannot be found on soft materials: events such as large deformations, severe illumination variations or other reasons can cause serious decorrelation effects in the deformed images and the measurement can fail. To overcome these issues, Bing et al. [51] adopted an incremental DIC technique based on an automatic reference image updating scheme which makes correlation between two consecutive images if the deformation reaches a certain threshold value. This method was successfully tested on a polypropylene sample foam up to 36% of its deformation during compression. However, paint coating, particularly on soft material, could increase the local stiffness reducing the surface deformation. The idea of exploiting the natural texture of the specimen has been implemented by other authors on other materials. For example, Wang and Cuitiño [52] decided to take advantage of the voids present on the specimen to obtain correlation for an ultra-light rigid open-cell PU foam. Hild et al. [53] studied, in compression, mineral-wool samples by a multiscale approach to increase the maximum detectable displacement compared to conventional DIC techniques. Being involved large displacements, they looked for the maximum correlation between the reference images and deformed ones, working on a discretization of the field of view into small zones. The few papers found in literature about this topic however do not present neither data about tensile and shear test nor data about behavior under cyclic loadings.

More specifically, the study presented in this chapter is aimed to identify the mechanical characteristics of three soft open-cell polyurethane foams of different densities, comparing them each other. One specific challenge of this work is to apply full-field 2D-DIC to detect great deformations (80% - 90%) of very soft materials exploiting not only the presence of voids of the cellular material but also the random presence of the small black fireproof particles that enhance the contrast and certainly allow to obtain better data. Indeed, thanks to the presence of a natural random pattern, given by the expanded graphite particles, foams can be explored by full-field 2D-DIC technique without applying any coating, to not modify the surface response. At the same time, this allows avoiding possible local cracks of the painting when high strains are reached, which can imply loss of decorrelation. In order to achieve a full mechanical characterization of the materials, a complete experimental campaign has been carried out, including tensile, shear and cyclic compression tests. For all these tests, the full displacement fields have been calculated by DIC software INSTRA 4D using an incremental correlation approach (reference image updated at each loading step) because of the very large deformations occurring in the foam [15].

4.1.1. Material Properties

For the experimental analysis three combustion modified soft open-cell polyurethane foams with the same manufacturing process but different densities were considered. These foams are particularly suited to the requirements of the aeronautic industry because of the presence of expanded graphite, visible as a random pattern of black dots (Figure 25), that makes them compliant to the flammability requirements for the human health safety. Type A, type B and type C cubic sample with a density respectively of 76÷94 kg/m3 (higher density), 60÷65 kg/m3 (medium density) and 43÷49 kg/m3 (lower density) are reported in Figure 25a from left to right, while their characteristics are schematized in Table 4. Foams are two-phase materials, consisting of a solid phase occupying a volume fraction φ:

$$\varphi = \frac{\rho_f}{\rho_s} \tag{13}$$

where ρ_f is referred to the foam bulk density, derived from the ratio of the mass of a known geometry foam sample to its volume (m_f / V_f), and ρ_s is the density of the fully dense constituting the matrix [26]. A comparison among the microstructures of the three types of foam is illustrated by the stereoscopic images shown in Figure 25b, c, d obtained using a Nikon SMZ-800 stereoscope.

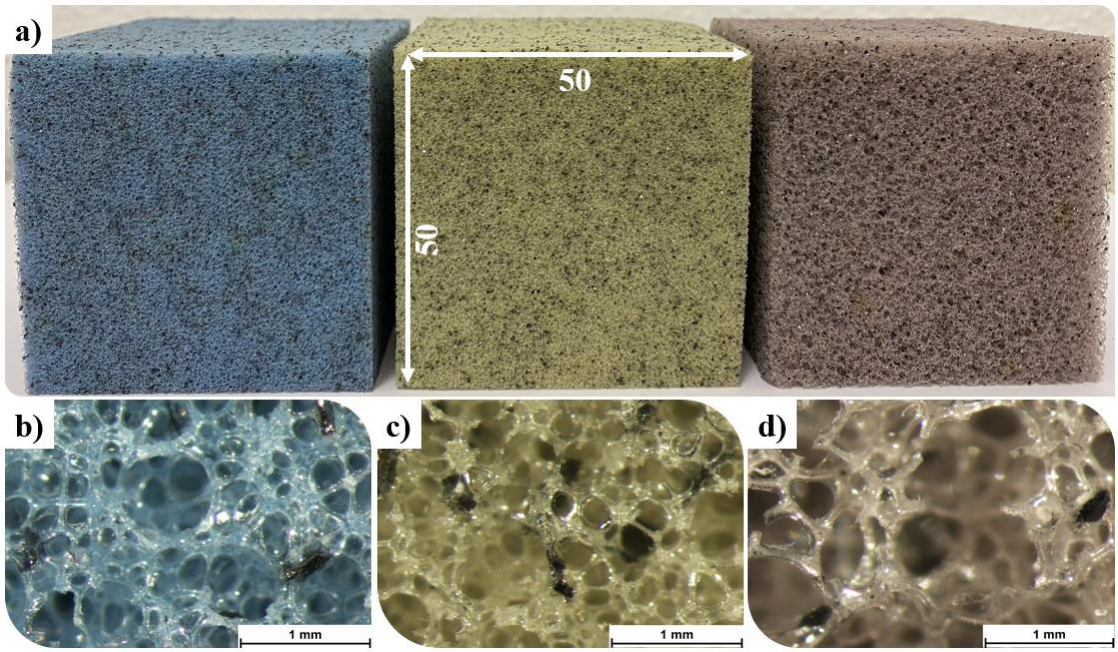

Figure 25 From left to right cubic simple of type A, type B and type C foam (a) and their microstructure obtained by Nikon SMZ-800 stereoscopic microscope with a 20x magnification for type A (b), type B (c) and type C (d) foams [17].

In order to characterize the cellular structure, the images were processed by the software NIS-Element and average measurements (Table 4) were obtained for the cell size and the percentage of voids presents in the material.

Table 4 Designation and characteristics of the tested materials [16].

Designation	Type A	Type B	Type C
Foam type	Flexible PU foam	Flexible PU foam	Flexible PU foam
Cells type	open	open	open
Density [kg/m^3]	76 ÷ 94	60 ÷ 65	43 ÷ 49
Cell size [mm]	0.145 ± 0.018	0.210 ± 0.076	0.315 ± 0.064
Cell wall size [mm]	0.044 ± 0.008	0.043 ± 0.006	0.041 ± 0.011
Void ratio %	35 ± 0.024	53 ± 0.113	65 ± 0.081

As it can be seen, the cells' size and the voids' percentage of the material increase with decreasing density. The average size of a cell is 145 μm for type A, 210 μm for type B and 315 μm for type C, while the percentage of voids in the material increases from 35 % to 65 %. Observing the measurements reported in Table 4 it can be deduced that the thickness of the cell wall does not undergo to significant variations as the density decreases. At a higher magnification scale, expanded graphite particles (Figure 25) appear like dots, clearly showing irregular shapes with an average length of 0.478 mm. Geometry, topology and spatial structure play a crucial role for the deformation behavior and the mechanical properties of cellular materials. Conventional foams behave differently depending on the load type they are subject to. During a tensile stress, the cell walls initially bend, then rotate towards the tensile axis and the lateral section of the cell became thinner; once the cell walls are perfectly aligned the stress continues to grow up until the cell walls break. In case of compression the cell walls bend and the lateral section of the whole cell structure becomes wider; as the load increases, the cell walls buckle and once the critical stress is reached, the cells collapse so that facing cell walls touch each other [26].

4.1.2. Planning Of the Experimental Campaign

After defining the scope of the study and the analysis methodology to be followed, now the testing campaign to determine the mechanical characteristics of the various foams under investigation is presented. It is necessary to obtain data related to stress-strain curves that define, for each material, the behavior under:

- Uniaxial Tensile Test (UNI EN ISO 1798) [54];

- Cyclic Compression (UNI EN ISO 3386**)** [55];
- Shear:
  - Block Shear setup:
    - ASTM C 273 [56];
    - BST (British Standard Test, BS 4370) [57];
  - IOSIPESCU setup (ASTM D 5379) [58]:
    - Notched specimen;
    - Unnotched specimen.

Since there is no dedicated standard for obtaining shear characteristics for this type of material, this type of test has been thoroughly investigated, and the results of different configurations have been compared. The total number of tests, as shown in Table 5, for tensile and the Iosipescu shear setup were also higher than those specified by the standards. As for the ASTM and BST shear configurations, only one type of test could be performed due to material quantity limitations; in any case, the reference standard does not specify a minimum number of tests to be conducted. Cyclic compression, not having a specific reference standard, was addressed based on the provisions related to simple compression, but following the guidelines provided in the finite element software Abaqus [59]. Indeed, the Abaqus guide provides all the necessary instructions for numerically modeling the foam and incorporating stress softening effects (i.e., the Mullins effect [60]). Given the four load cycles performed for each specimen, it was deemed appropriate to test only one specimen per type.

Table 5 Number of tests conducted on each specimen for each type of test.

				N° performed test for each density foam		
Test Type				**Type A**	**Type B**	**Type C**
Uniaxial Tensile Test				6	6	6
Cyclic compression				1	1	1
Shear test	setup	ASTM	25mm	1	1	1
			50mm	1	1	1
		BST	25mm	1	1	1
			50mm	1	1	1
		IOSIPESCU	Notched	6	6	6
			Unnotched	6	6	6

4.2. Digital Image Correlation

When soft materials are tested, such as low-density polyurethane foams, large deformations occur so traditional measurement systems fail. A solution to avoid contact with the specimen's surface can be obtained by performing Digital Image Correlation (DIC) analysis, which allows full-field displacement and strain maps determination. DIC is based on the comparison of the differences between the speckle pattern generally acquired at zero load (reference image) with speckle pattern captured subsequently to the body's deformation, in order to find the maximum correlation among given pixel subsets within the images. In conventional DIC technique a fixed reference image is used so that all the elaborations are performed in relationship with this first reference stage. In this study, instead, in order to avoid serious decorrelation due to large deformation and detrimental illumination fluctuations, the incremental DIC approach was adopted [51]. In the incremental DIC, the speckle pattern corresponding to the n^{th} displacement step is correlated with the speckle pattern recorded from the image of the previous displacement, $(n-1)^{st}$ step. By this way, although large deformations occur, even up to 90% for a flexible foam, the problem connected with lack of correlation is greatly diminished. The main components of the adopted DIC measurement system are summarized in Figure 26. Only a camera was used since, being interested to in plane deformation, the 2D technique was applied. In fact, for the materials analyzed in this study in-plane displacements are more important than the out-of-plane plane ones, the surface of the specimen is flat and the camera can be placed perpendicular to the surface of the object [61]. Furthermore, due to the isotropic behavior of the material and to the axial symmetry of the cubic specimen and load conditions, the out-of-plane component can be estimated. The setup was optimized in order to set the proper distance between the specimen and the pinhole (Table 6,Table 7) [61,62]. The capture system is equipped with ISTRA 4D software (Dantec Dynamics A/S, Skovlunde, Denmark), which receives data from the GigE CCD Manta camera (1628 x 1436 pixels) AVT (Allied Vision Technologies GmbH, Stadtroda, Germany), equipped with XENOPLAN 1.4/ 23-0902 or RICOH FLCC1614-2M lens. Further details about hardware and analysis parameters are listed in

Table 6 and Table 8 for tensile and cyclic compression test, in Table 7 and Table 9 for three different setup of the shear test. The camera is mounted on a support bar to prevent acquisitions from being disturbed by vibrations. To obtain a good correlation, a LED source with high emission stability was used to illuminate the analyzed area. All experiments were performed in optimized lighting conditions founded by arranging the light to be grazing to the surface's specimen to avoid unwanted reflections and light peaks generated. Before starting the measurements, the calibration of the DIC system was performed to take into account the parameters of the acquisition system.

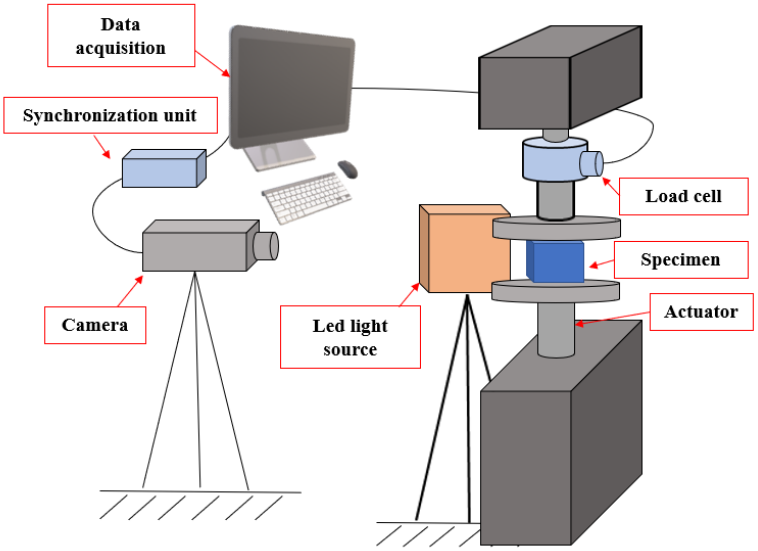

Figure 26 Schematic of the DIC set-up used to follow cyclic compression mechanical tests.

Table 6 DIC Hardware Parameters for tensile and Cyclic compression test [16].

	Uniaxial tensile test	**Cyclic compression test**
Camera	Manta camera AVT	
Image Resolution	1628 x 1436 pixels	
Lens	XENOPLAN 1.4/ 23-0902 F.L. = 23 mm	
Aperture	f/5.6	
Field-of-View	153 x 135 mm	120 x 106 mm
Image Scale	13.6 pixel/mm	10.6 pixel/mm
Stand-off Distance	850 mm	800 mm
Image Acquisition Rate	17 Hz	10 Hz
Patterning Technique	Natural Texture of the specimen	

Table 7 DIC Hardware Parameters for ASTM, British Standard and Iosipescu shear test.

	ASTM	**BST**	**IOSIPESCU**
Camera	Manta camera AVT		
Image Resolution	1628 x 1436 pixels		
Lens	RICOH FLCC1614-2M F.L. 16 mm		
Aperture	f/4	f/4	f/3.9
Field-of-View	400 x 353 mm	400 x 353 mm	148 x 114 mm
Image Scale	4 pixel/mm	4 pixel/mm	11 pixel/mm
Stand-off Distance	800 mm	800 mm	470 mm
Image Acquisition Rate	1 Hz	1 Hz	1Hz
Patterning Technique	Natural Texture of the specimen		

Table 8 DIC Analysis Parameters for tensile and Cyclic compression test [16].

	Uniaxial tensile test	Cyclic compression test
DIC Software	ISTRA 4D software v. 4.4.3.497 by Dantec Dynamics	
Image Filtering	None	
Subset Size	19 pixels	
Step Size	17 pixels	
Subset Shape Function	Affine	
Matching Criterion	Square differences	
Interpolant	None	
Displacement Noise-Floor	13.50 μm	14.00 μm

Table 9 DIC analysis parameters for ASTM, British Standard and Iosipescu shear test.

	ASTM	BST	IOSIPESCU
DIC Software	ISTRA 4D software v. 4.4.3.497 by Dantec Dynamics		
Image Filtering	None		
Subset Size	19 pixels		
Step Size	17 pixels		
Subset Shape Function	Affine		
Matching Criterion	Square differences		
Interpolant	None		
Displacement Noise-Floor	18.00 μm	18.00 μm	19 μm

4.2.1. Natural Pattern Preliminary Evaluation

In order to evaluate the feasibility of adopting the natural texture of the specimens given by the presence of the graphitized particles, some preliminary analyses of the pattern quality were done taking into account the Shannon Entropy (SE) values [63], the black/white ratio and the speckle size of the images to be processed. The speckle pattern quality assessment is an important aspect to consider in order to obtain good texture correlation and reliable measurements. Some authors [64] investigated the relationship between the errors of the displacement measurements and the Shannon Entropy (SE) of the speckle pattern proving that a speckle pattern with large SE produces a small mean error. In the specific case, since the analysis concern a grayscale image, the Shannon Entropy (H) quantifies the normalized probability of gray level occurrence, $(p(GL_i))$, for each gray level GL_i [64]:

$$H = \sum_i p(GL_i)\log\left(p(GL_i)\right). \quad (14)$$

In this study, using a specifically developed Python routine, values of the images of a generic low-density soft open-cell PU foam were compared with those of the surface of the three foams containing the black particles of fireproof graphite scattered randomly in the material. The obtained results, Type A = 7.07; Type B = 7.21; Type C = 7.18; Generic PU foam = 6.22 (see Table 10) are consistent with those obtained by other authors [64,65]. The second analysis aimed to evaluate the speckle density

of the pattern and the average speckle size. To this purpose, a Matlab® routine was implemented transforming the 8-bit image acquired by the camera into a binary image through a greyscale filter and then operating a color inversion as shown in Figure 27 Speckle pattern image acquired by the camera and correspondent binary images obtained by Matlab® for type A, type B, type C and for a generic open-cell PU foam [16].Figure 27. For types A, B and C and for the generic PU foam the black/white ratio output are respectively 58.6%, 59.8%, 63.6% and 19.1%. It worth reminding that a good analysis is achieved with a pattern that presents a black/white ratio of about 50%. Concerning with the speckle size analysis it was found that speckles are mainly distributed from 2 to 4 pixels, also this analysis shows that the graphite fireproof particles allow to improve the contrast and to obtain better results compared to a surface in which only the empty/full contrast of the pores is exploited.

Table 10 Black/White ratio and Shannon Entropy values comparison.

	Type A	**Type B**	**Type C**	**Generic Foam**
SE	7.07	7.21	7.18	6.22
Black/White ratio [%]	58.6	59.8	63.6	19.1

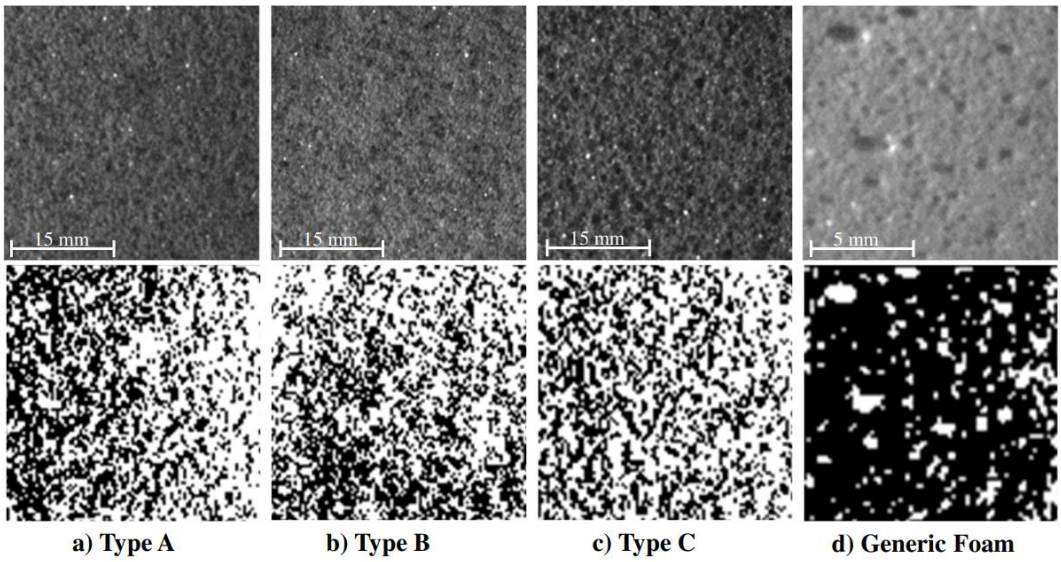

Figure 27 Speckle pattern image acquired by the camera and correspondent binary images obtained by Matlab® for type A, type B, type C and for a generic open-cell PU foam [16].

4.2.2. Strain Measurements

Once the images were recorded, they were processed to obtain chromatic map containing the information about displacements and strain distribution. For the data analysis it has been assumed

that the Y-axis coincides with the direction of the load and the X-axis coincides with the in-plane direction transverse to the load. Placing virtual strain gauges on the map all the material strain information needed to extract the stress-strain curves, the stiffness and the Poisson's function of the examined foams has been taken out.

Starting from the undeformed configuration, the coordinates of two virtual reference points, P1 and P2, taken on the X-Y plane, were considered close to the lines which delimitate the useful section for the tensile test (Figure 28a), close to the central area near the plates for the shear test (Figure 28b) and close to the contact with the plates for the cyclic compression test (Figure 28c).

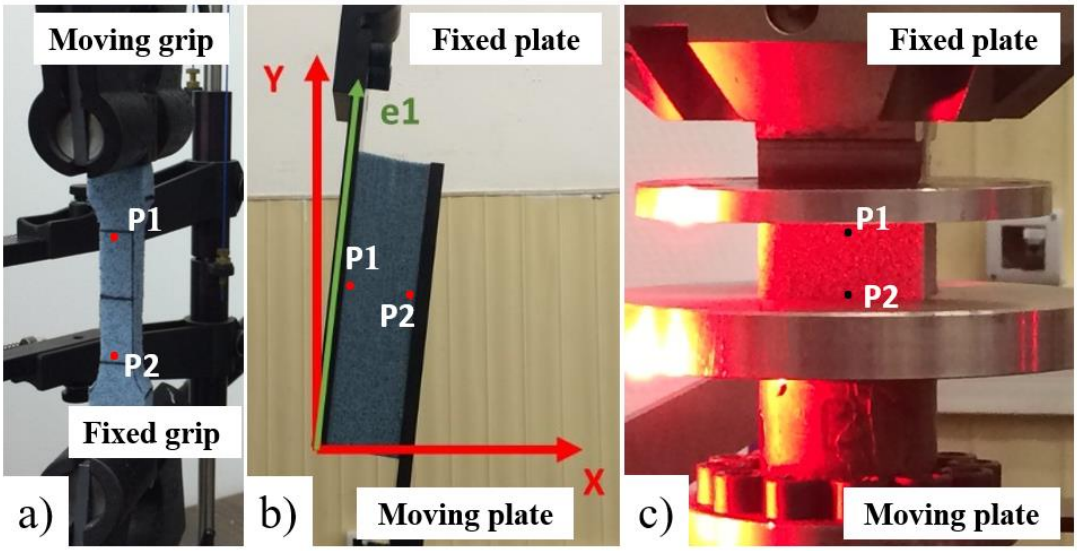

Figure 28 Reference for the measurements points for a) tensile test, b) ASTM block shear test and c) cyclic compression test.

The distance between the two points along the Y axis was then measured as:

$$L_0 = Y_{P1} - Y_{P2} \tag{15}$$

were L_0 is the distance between the two points of the undeformed configuration.

Once the two points have been set, the software is able to associate a given pixel to that position and to record the displacement during the test:

$$L_i = Y_{P1_i} - Y_{P2_i} \qquad 0 \leq i \leq t \tag{16}$$

where i is the time step of the total time duration of the test t.

Then, through the ratio between the deformed configuration L_i and the undeformed L_0, the entire engineering or Cauchy strain, e, along the Y direction, in the time span t of the test is obtained:

$$e_{y_i} = \frac{Y_{P1_i} - Y_{P2_i}}{L_0} = \frac{L_i}{L_0} \qquad 0 \leq i \leq t \tag{17}$$

The same procedure was carried out to calculate the strain in the direction transverse to load, namely along X, taking two other reference points respectively on the right and left sides of the specimen. Facing with great deformation the true or Hencky strain, ε_i it should be taken into account. This is defined as the ratio of the extension to the instantaneous length:

$$\varepsilon_i = \frac{L_i - L_{i-1}}{L_i} = \ln(1 + e_i) \qquad 0 \leq i \leq t. \tag{18}$$

The true strain component ε_i can be calculated by the logarithm of the engineering strain e_i, as shown in Eq. 18. Furthermore, the accuracy of the measurements was assessed, so the average error, in percentage, was calculated considering all the values recorded during a single test, for each material. In order not to burden the discussion and given that the found values are very similar, the average of the three foam types is reported. For the displacements along Y direction the average maximum error is 0.12% and 1.65% respectively for the tensile and the cyclic compression test. For the displacements recorded along the direction transverse to the load (X axis) the errors are higher. Considering a point taken near the right edge and another taken near the left edge of the specimen, the error percentage values are 1.14% and 3.12% for the tensile test, 2.91% and 2.05% for the cyclic compression test. For the shear test the good quality speckle pattern allows measurement uncertainties always lower than 3%. Considering each value of the measurement uncertainties it can be said that the errors are higher in correspondence of the first loading and last unloading phases (only present in cyclic compression). For large deformations, as also found by other authors [66], errors are negligible, especially considering that the displacements are of the order of 40 millimeters and the uncertainties are of the order of the micrometer. Furthermore, for the specific case, in face of possible errors in the calculation of the displacement field, there is the advantage of not painting the specimen, a fact which is not negligible considering a soft material with great elastic behavior.

4.3. Numerical Modeling

Finite element model was built using Abaqus 6.13-1 in order to reproduce the uniaxial and compression experimental tests and the material response. Since the foam is homogeneous, 2-D models are implemented for both cases. The tested specimens were discretized using 948 and 2601 four-node plane stress element CPS4 respectively for dog-bone sample and for square sample.

To describe accurately the mechanical response of the hyperelastic foam (e.g., isotropic; nonlinear behavior; very large volumetric changes, elastic deformation up to 90%; energy dissipation), the

hyperfoam model was used [59]. The strain energy function **U** for this type of materials, originally purposed by Ogden [67], is written as:

$$U = \sum_{i=1}^{N} \frac{2\mu_i}{{\alpha_i}^2}\left[\hat{\lambda}_1^{\alpha_i} + \hat{\lambda}_2^{\alpha_i} + \hat{\lambda}_3^{\alpha_i} - 3 + \frac{1}{\beta_i}\left((J^{el})^{-\alpha_i\beta_i} - 1\right)\right] \tag{19}$$

where N is the order of the strain energy potential ($N \leq 6$), μ_i is related to the initial shear modulus, α_i specifies the shape of the stress-strain curve, while β_i determines the degree of compressibility and is directly related to the Poisson's ratio, ν_i, by the expression:

$$\beta_i = \frac{\nu_i}{1-2\nu_i}, \qquad \nu_i = \frac{\beta_i}{1+2\beta_i}. \tag{20}$$

The principal stretches λ_j represent the ratios of the current length to the length in the original configuration in the principal directions and are related to the principal nominal strains, e_j, by:

$$\lambda_j = 1 + e_j \ . \tag{21}$$

More practically, λ_j are used to express the deformation gradient:

$$\boldsymbol{F} = \begin{bmatrix} \lambda_1 & 0 & 0 \\ 0 & \lambda_2 & 0 \\ 0 & 0 & \lambda_3 \end{bmatrix}, \tag{22}$$

whose determinant represents the total volume ratio $J = \det(\mathbf{F}) = \lambda_1\lambda_2\lambda_3 \neq 1$ for a not incompressible elastomeric foam. Specifically, the elastic volume ratio, J^{el}, used in Eq. 19 is related to the total volume ratio, J, by the equation:

$$J^{el} = \frac{J}{J^{th}} \ , \tag{23}$$

where J^{th} is the thermal volume ratio, used to define the principal stretches components in Eq. 19:

$$\hat{\lambda}_j = (J^{th})^{-\frac{1}{3}}\lambda_j \ , \qquad J^{el} = \hat{\lambda}_1\,\hat{\lambda}_2\hat{\lambda}_3. \tag{24}$$

To investigate the relevance of the Poisson's ratio (§ 4.6) in defining the mechanical response of hyperelastic foams, alternatively ν = 0, ν = a constant value and ν equal to the nominal transverse strain data point by point were implemented into the FE models.

4.3.1. Mullins Effect

The actual behavior of elastomers under cyclic loading conditions is quite complex. Some simplifications have been made to facilitate modeling. Essentially, these simplifications translate into two main components related to material behavior: the first describes the response of a material point (from an undeformed state) under monotonic stress, and the second is associated with damage and describes the load-unload behavior. When an elastomeric specimen is subjected to tension from its initial state, unloaded, and then reloaded, the stress required to reload is lower than that on the initial loading for segments up to the maximum reached during the initial loading. This stress attenuation phenomenon is known as the Mullins effect and reflects the damage incurred during the previous loading. This type of material response is qualitatively represented in Figure 29.

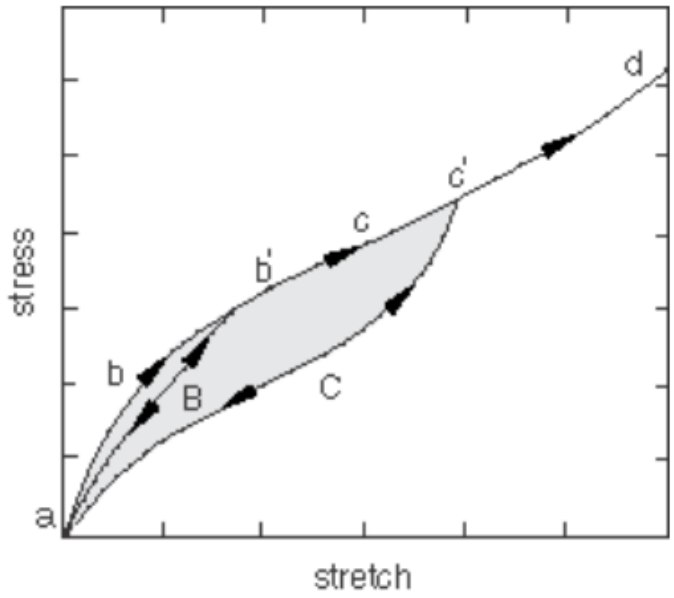

Figure 29 Idealized response of the Mullins effect model [59].

This figure and the accompanying description are based on the work of Ogden and Roxburgh [68], which forms the basis of the model implemented in Abaqus. Consider the loading path abb' of a material that has never been subjected to any type of load before, loaded up to an arbitrary point b'. When unloading from b', the path followed is b'Ba. When the material is loaded again, it follows the *softened* path aBb'. If an additional load is applied, the path b'c is followed, where b'c is a continuation of the primary loading path abb'cc'd (which is the path that would be followed if there were no unloading). If the load is now held at c', the path c'Ca is followed during unloading, and then c' is reached again when the same specimen is reloaded. If no additional load is applied beyond c', the curve aCc' represents the subsequent material response, which is elastic. To load beyond c', the main path is followed again, and the described pattern is repeated [59]. This is, of course, an ideal representation of the Mullins effect as there are also hysteresis effects. The *softening* of the material,

known as stress softening, has been interpreted as being due to damage at the microscopic level. When the material is loaded, the damage is caused by the breaking of bonds between filler particles and rubber molecular chains. Different bonds between chains are broken at different levels of deformation, resulting in continuous macroscopic deformation. An equivalent interpretation is that the energy required to cause the damage is non-recoverable. In particular, for the Mullins effect model implemented in Abaqus, the constitutive equation related to the total strain energy density has a deviatoric and a volumetric part [59].

$$U = U_{dev} + U_{vol} \tag{25}$$

4.4. Uniaxial Tensile Test

4.4.1. Experimental setup

Quasi static uniaxial tensile tests were carried out in accordance with the UNI EN ISO 1798 [54] , at a room temperature equal to 23 °C. *Dog bone shaped* specimens were used having a useful section area of 10 mm x 12 mm (Figure 30a). Samples were tested using an electro-mechanic INSTRON 3340 machine instrumented with 1kN load cell. The deformation was recorded by a DIC system as described in § 4.2. According to the standard, a crosshead speed of 500 mm/min was applied. For each foam type at least five specimens were tested. To guide the grabbing of the samples between the grips, horizontal lines were drawn at 25 mm from both the top and bottom edge of the specimen, as shown in Figure 30b. In addition, reference for the useful section and for the central area were traced (see Figure 30b) to verify that the break occurred in the useful portion of the specimen. Pre-load conditions were checked to be within the norm (0.1 kPa).

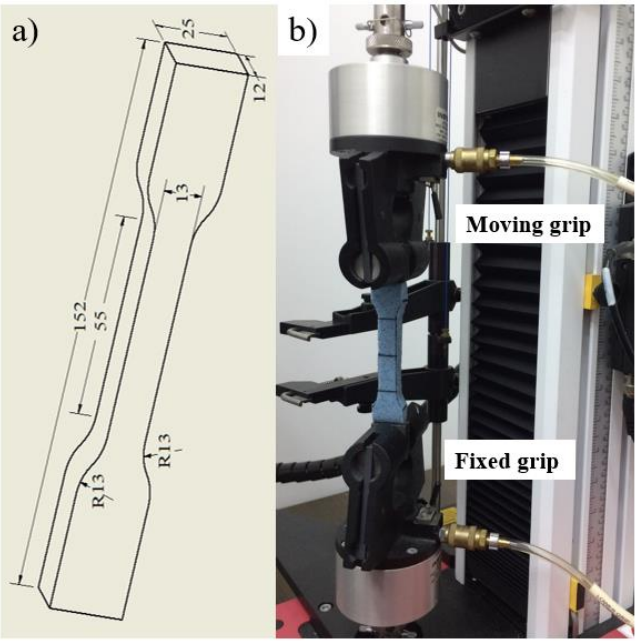

Figure 30 a) Tensile test specimen (measures are expressed in mm), b) detail of tensile test fixture system.

4.4.2. Experimental Results and discussion

Tests were carried out until the failure's achievement of more than five specimens for each material, ensuring that the break occurred in the useful section of the specimen. The entire test's duration for all samples was recorded by the camera, in order to obtain the images sequences to be processed through the DIC and obtain the surface's points displacement. The sequence of images in Figure 31 shows the chromatic map of the unloaded sample (Figure 31a), which has a random appearance and indicate the amount of the displacement noise floor. This map is obtained by the correlation between the reference image, taken at zero load, and a subsequent image taken just a moment later, keeping the zero load conditions.

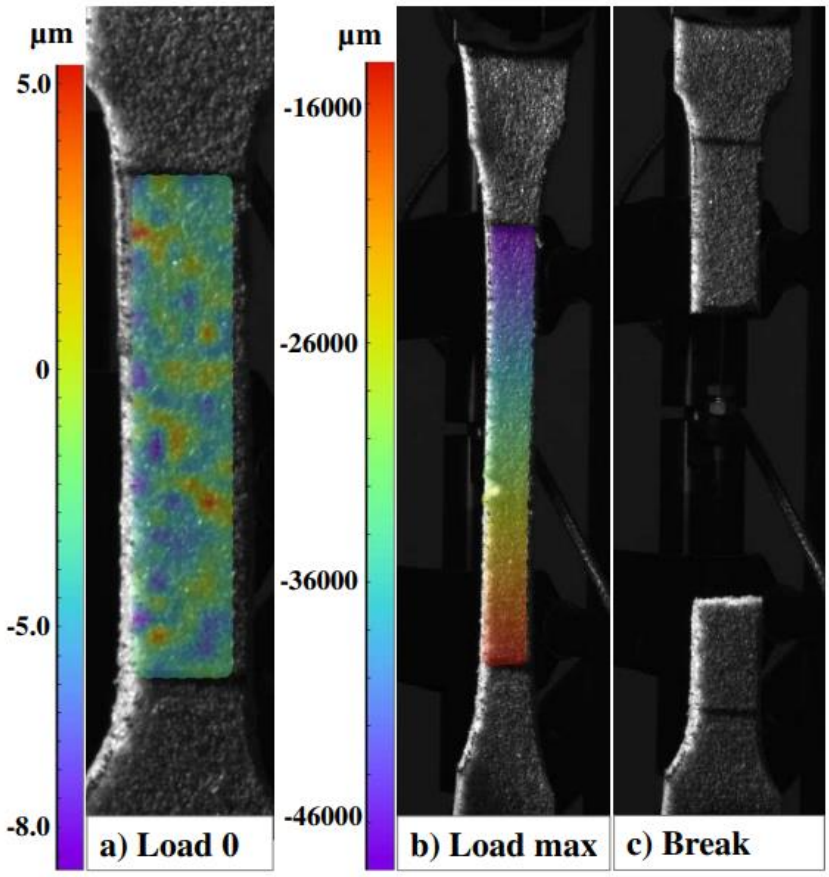

Figure 31 Tensile test chromatic map (expressed in µm) of the displacement field before the loading (a), at the maximum load (b) and at the broken instant [15].

This map differs a lot from the configuration of the various colors bands that the sample assumes while it is loaded, as shown in the moment of maximum load (Figure 31b) just before the break (Figure 31c), which is the critical moment in which the correlation is lost and, consequently, the map disappears. Coherently with what is expected, the chromatic map, in this case, shows the major displacements in purple (48 mm), in correspondence of the upper movable clamping, and the minor displacements in red (16 mm), in correspondence of the lower fixed clamping. After the data processing stress-strain curves were obtained for each material, the one that approximates the average trend of the entire set was considered, while values reported in Table 11 were calculated considering the results' average obtained by the tests performed for each foam density. The stress-strain curves (Figure 32) show the same trend of those obtained by Gibson and Ashby [26] for elastomeric honeycomb materials tested in tension, considering in-plane deformation. Assuming that cells have a general hexagonal cells shape, initially the cell walls bend, then rotate towards the tensile axis and, as a consequence, the stress rises until the breakage. Observing the images in Figure 31 and the curves in Figure 32 it is clear that in tension these soft open cell polyurethane foams are elastic until

they tear. Following Gibson and Ashby [26] and other studies [24,37,48,69] the experimental values of the linear elastic modules of the foams, E*, were measured from the slope of the first part of the tensile stress-strain curves until 5% of strain. The obtained modules were then compared to those obtained following the analytical expression (eq. 26) and taking into account the base material values given by Gibson and Ashby for open cell foam, considering a flexible polyurethane density of ρ_s = 1200 kg/m^3 and a Young modulus E_s = 45 MPa [26]:

$$\frac{E^*}{E_S} = C_1 \left(\frac{\rho^*}{\rho_S}\right)^2 ; \tag{26}$$

where subscript s referred to the solid base material while the apex * to foamed material. The constant C_1, that includes the geometric constants of proportionality, is assumed to be equal to 1 in accordance with Gibson and Ashby [26].

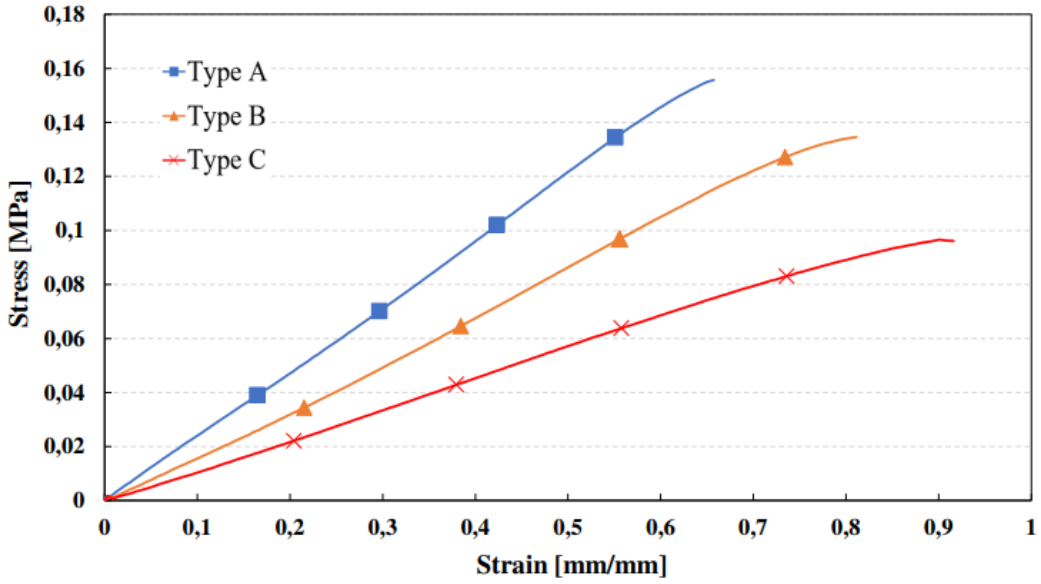

Figure 32 Tensile stress-strain curve for Type A, Type B and Type C soft polyurethane foam [15].

Considering the values averaged, the higher density foam, type A, has a curve slope greater than the other two foams, a lower break elongation, close to 62%, and a higher medium breaking load of 144.2 kPa. Type C foam, with a very low density, compared with foam A and B, shows the minor slope with a higher elongation at break (above 90%) and a lower breaking load which reaches on average 94.5 kPa. Type B foam, consistently with its density characteristics, exhibits an intermediate behavior between A and C, with an elongation at break of almost 75% and a breaking load of 124.6 kPa. As reported in Table 11 the denser type A foam exhibits a more rigid behavior with an experimental Young's modulus of about 237 kPa, followed by type B with a modulus of 154 kPa; finally, type C foam has a lower slope which corresponds to a lower stiffness of 106 kPa. For all

tests, the values of the predicted modules are always lower than those evaluated by the tensile experimental data and can be reasonably considered similar for the denser type A foam with a difference of 12 kPa.

Table 11 Predicted elastic modulus, tensile elastic modulus and stress outputs at 5% strain, UTS limits and maximum strain [15].

Foam Sample	E* predicted [kPa]	E* measured at 5% strain [kPa]	Stress at 5% strain [kPa]	Ultimate Tensile Strength UTS [kPa]	Max Δl/l %
Type A	225.8	237.1 ± 9.7	11.8 ± 1.3	144.2 ± 17.6	62.4 ± 4.5
Type B	124.0	154.0 ± 7.1	7.7 ± 0.4	124.6 ± 11.4	74.4 ± 5.2
Type C	66.1	105.7 ± 4.3	5.2 ± 0.1	94.5 ± 12.0	91.8 ± 8.2

It is noteworthy that the values of the predicted linear elastic modules of the less dense foams, type B and C, are more similar to those obtained for the first compression cycle, as shown in Table 13 (§ 4.6.2), for which there is a deviation of respectively 1 kPa and 7 kPa, while the difference is greater in respect to the tensile data, 30 kPa and 40 kPa for type B and type C foam. Unlike the other predicted values, which are always lower than those obtained from the first compression cycle (20% strain), the predicted elastic value of the denser type A foam is 66 kPa larger than the one obtained in compression at first cycle.

4.5. Shear test: a critical comparison among experimental approaches

Polyurethane foams find widespread use in various industries, including aerospace, aeronautics, automotive, and packaging. They are particularly suitable for designing essential sacrificial components in the event of impact [18]. Several standards can be found for the shear testing of rigid materials, allowing for different test setups based on material properties, including block shear tests [70–73] , V-notched rail shear test [74], Iosipescu [75–79], Arcan shear test [80], three- or four-point bending test [81,82]. On the contrary, when it comes to extremely soft materials, such as open-cell polyurethane foams, no specific standards for shear testing can be referred. Generally, existing standard for sandwich structures, such as ASTM C 273 [56], are used. In literature, a study by Nazari et al. [83] can be found investigating the response of an elastomeric foam applied as a core for composite sandwich beams, while in of Li et al. [84] the development of a rate-sensitive constitutive model for anisotropic cellular materials can be found. It is worth noting that all the cited studies utilize traditional measurement techniques rather than full-field optical techniques. However, given the complexity of open-cell flexible foams, proper mechanical characterization requires the use of full-field optical measurement techniques, such as Digital Image Correlation (DIC) [85]. Nevertheless, the morphology of their surface makes it hard to apply a speckle pattern, and the high

level of deformation exhibited by these foams compromises their integrity and proper visualization. In fact, most studies on polymeric foams using DIC have been conducted on rigid foam materials. Marsavina et al. [86] investigated the shear and fracture of PUR foam; Taher et al. [87] studied bidirectional thermo-mechanical properties of foam core materials; Daiyan et al. [88] studied crack propagation by comparing V-notched and Iosipescu shear tests; Escusa et al. [89] observed shear strain evolution during the block shear test; finally, Kalina et al. [90] who studied the use of experimental optical techniques for investigating shear strains of samples exposed to shear stress beyond the yield point. In this study, stress-strain curves and shear moduli were obtained through the following test methods, using different specimen geometries and thicknesses: ASTM C 273 [56] with specimens of 25 mm and 50 mm, BS 4370 [57] with specimens of 25 mm and 50 mm, ASTM D5379 (Iosipescu) [58] with notched and unnotched specimens [91]. The first two standards are related to sandwich structures and have different test setups, with inclined and straight specimens, respectively. The last one is primarily used for characterizing rigid composite materials. The aim is to compare the stress-strain behavior and investigate the presence of secondary effects, such as bending, edge effects, and undesired normal stresses. Furthermore, the elastic moduli, obtained up to 5% strain, were compared among the different tests and with engineering moduli derived from linear relationships using known moduli for compression and tension.

4.5.1. Block Shear ASTM and BST

In the absence of a specific standard aimed at determining the shear characteristics of soft hyperelastic foams, different types of setups and specimens with different aspect ratios (AR) were compared to investigate parasitic effects such as bending moment, undesired normal stresses, and the effect of free edges [70]. Frequently, the material is supplied in sheets of 25 or 50 mm and the testing must be performed with the available material geometries. It was decided to compare the results obtained from the ASTM standard, which has an inclined configuration, clearly visible in Figure 33a, with those obtained from the BST standard (Figure 33b), along with details regarding the gripping system and the geometry of the tested specimens. While the ASTM C 273 standard is intended for the analysis of sandwich structures regardless of the core material, the BS 4370 is specific for testing the core of sandwich structures made of rigid cellular materials. The tests were conducted in tension using the INSTRON 1342 testing machine equipped with a 10 kN load cell, the actuator speed, as indicated in the ASTM standard, was set at 50 mm/min, and data acquisitions for load and crosshead displacement were set at a frequency of 20 Hz. Due to limited material availability, one specimen per test type and geometry was analyzed.

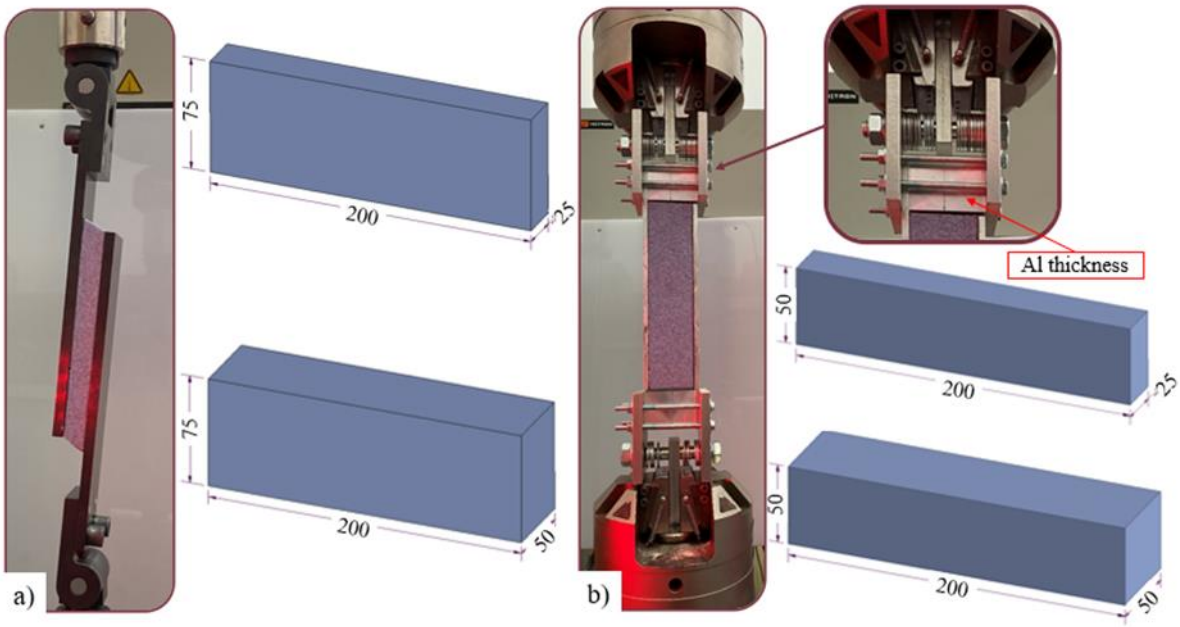

Figure 33 a) ASTM C 273 Setup and dimensions of tested specimens, b) BST BS 4370 setup with gripping system detail and dimensions of tested specimens.

4.5.2. ASTM D 5379 (Iosipescu)

Since performing the Block Shear tests requires large blocks, up to 200 mm long and 70 mm wide, and 200 mm long and 50 mm wide respectively for the ASTM and the BTS standard; the results obtained from a shear setup that allows for much less material waste, namely ASTM D 5379, also known as Iosipescu, were investigated. The setup utilizing aluminum grips for the ASTM D 5379 (Iosipescu) test allows for the analysis of relatively small specimens, measuring 26 x 20 x 13 mm, as shown in Figure 34. The aluminum grips are used to securely hold the foam specimens during the testing process.
For the Iosipescu test, two types of specimens were investigated:

- notched Specimen: the specimen has a 90° notch in the central area, as required by the standard for studying shear behavior in rigid materials. The 90° notch in the central area allow to achieve as uniform a shear condition as possible [75];

- unnotched Specimen: the unnotched specimen does not have a notch, and this setup was tested to address concerns about potential premature failure with notched specimens, especially considering the soft nature of the foam.

Normally, this setup is used in compression, but in this case, that approach would not work since the specimen would touch the bottom of the setup. Therefore, the lower plate of the setup was anchored to the fixed base of the MTS Alliance RT/30 testing machine using clamps, and the tests were also performed in tension. The testing machine utilized was equipped with a 1 kN load cell. Even if the standard specifies an actuator speed of 20 mm/min, an additional test was conducted at 50 mm/min, as those related to the block shear test, to investigate if the rate of load application could influence the results. Data acquisitions for load and crosshead displacement were set at a frequency of 10 Hz. In total, at least 5 specimens were tested for each foam type and specimen geometry: notched and unnotched.

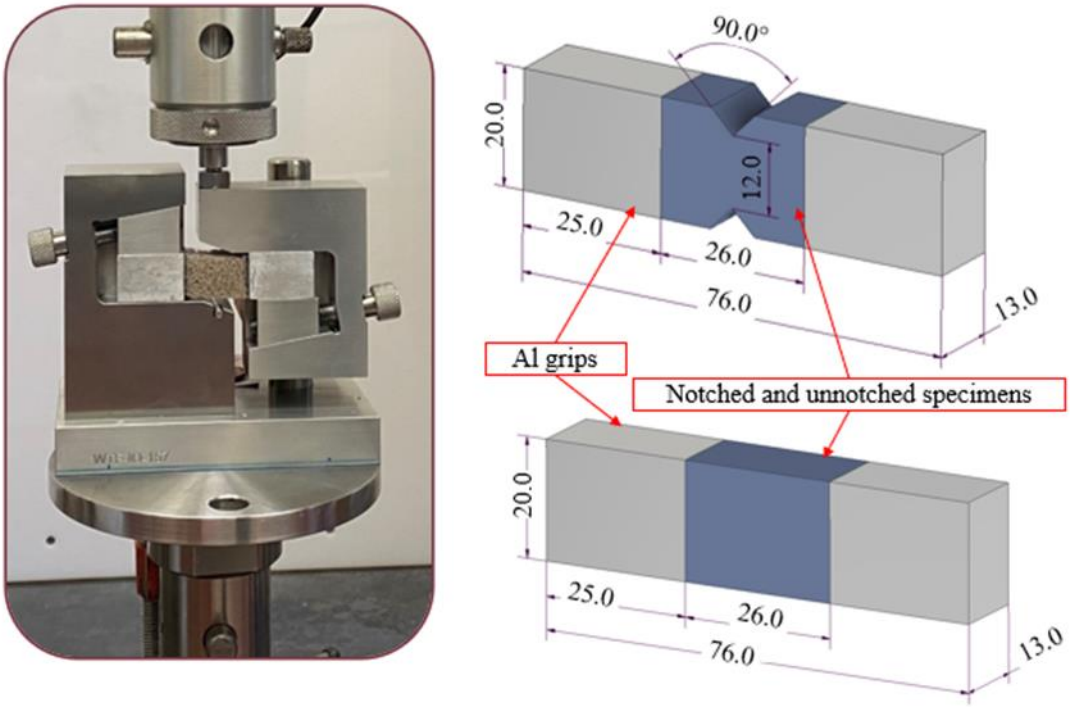

Figure 34 Setup ASTM D 5379, aluminium grips and dimensions of notched and unnotched specimens.

4.5.3. Experimental setup and measurements

Figure 35a and Figure 35b show the experimental setup including the DIC instrumentation respectively for the bloc shear and the Iosipescu test. Normally, the ASTM C 273 standard requires measurements to be taken through an extensometer placed on the steel plates in the central region of the specimen. On the other hand, the BST standard requires data acquisition related to the displacement of the crosshead, while the Iosipescu standard calls for the use of two strain gauges positioned at ±45° in the central area of the specimen, at the location of the notch. Since DIC is a full-field technique, it allows for versatile measurement acquisition. Therefore, the strain was calculated for all tests, considering two points near the plates in the central section of the specimen and using two virtual extensometers arranged at ±45° in the central section of the specimen, as shown in Figure 35c and Figure 35d, respectively, for the ASTM block shear test and the Iosipescu test. The strain $\gamma_{y_i}$was computed from the displacements of points P_1 and P_2, i.e., Y_{P1_i} e Y_{P2_i} for each time instant *i*, considering the initial distance between the two points, denoted as d_0, as shown in equation 27. The strain γ_i, for each time instant *i*, was calculated using two virtual extensometers positioned at ±45°, measuring the two principal strains ε_{L_1} ed ε_{L_2}, as described in equation 28.

$$\gamma_{y_i} = \frac{Y_{P1_i} - Y_{P2_i}}{d_0} = \frac{L_i}{d_0} \tag{27}$$

$$\gamma_i = |\varepsilon_{+45}| + |\varepsilon_{-45}| = |\varepsilon_{L_1}| + |\varepsilon_{L_2}| \tag{28}$$

$$\tau = \frac{P_i}{Lb} \tag{29}$$

The stresses τ were calculated by dividing the load P_i, recorded by the testing machines for each time instant i, by the cross-sectional area of the specimen, which is given by the product of its length L and width b, as shown in equation 29. For the inclined ASTM C 273 configuration, the data were projected along the vector e_1, which is parallel to the inclination of the plates (Figure 28b).

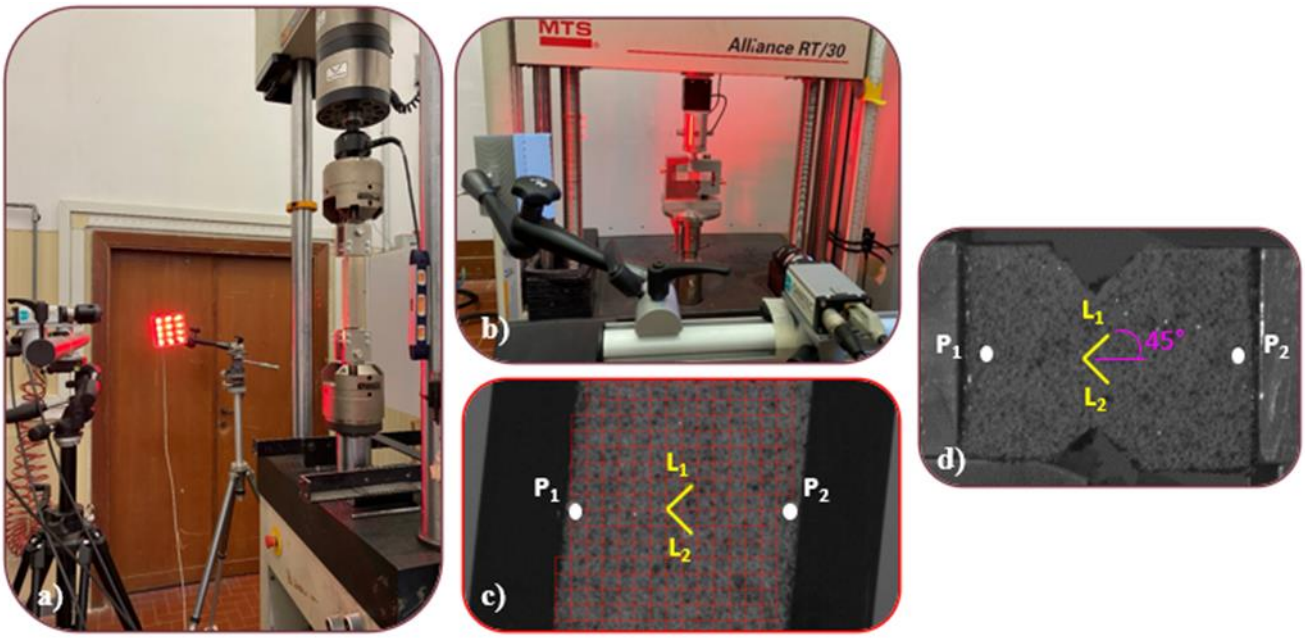

Figure 35 a) DIC setup used for ASTM and BS block shear tests, b) DIC setup used for ASTM D 5379 (Iosipescu) test, c) Measurement method using two points and two virtual extensometers on ASTM block shear test specimen, d) Measurement method using two points and two virtual extensometers on notched Iosipescu test specimen.

4.5.4. Results and discussion

The results of the stress-strain curves were analyzed first, as shown in Figure 36, Figure 37, Figure 38, respectively for Type A, Type B, and Type C foam for each test type considering all geometries and measurement methods. Test types are block shear test, which include ASTM and British Standard Test; and Iosipescu with notched specimen (indicated as *NOTCH* in the legend) and unnotched specimen (indicated as *IOS* in the legend). Measurement methods refer to using two reference points (Figure 36a, Figure 37a, Figure 38a, Figure 39a, Figure 40a) and considering virtual strain gauges at 45° (Figure 36b, Figure 37b, Figure 38b, Figure 39b, Figure 40b) as was already clarified in § 4.5.3. The reference results for all tests are those obtained from the ASTM 25 mm block shear strain test, shown in red, which, according to the literature studies, is considered to be the configuration least affected by secondary parasitic effects [92]. In the graphs, the best curves have been shown. Having

conducted an experimental campaign that includes numerous tests, it is advisable to consider the values reported in Table 12 for the elastic moduli.

Taking into consideration the measurements taken with two points for Type A, Figure 36a, it can be observed that for the same type of block shear test, ASTM and BST, after approximately 20% strain, the curves for thicknesses of 25 mm and 50 mm diverge a bit. The unnotched Iosipescu specimen traces well the BST test with a 25 mm specimen and the ASTM test with 50 mm specimen. The unnotched Iosipescu specimen tested at a strain rate of 50 mm/min (A_IOS) closely matches the ASTM test with a 25 mm specimen. It is evident that the notched specimen (A_NOTCH) provides a curve that deviates completely from the others. In the zoomed-in detail of Figure 36a, it is observed that the slope of the curves up to 5% strain is nearly the same for all specimens except for the notched Iosipescu specimen. The bundles of curves obtained using virtual strain gauges placed in the central part of the specimen at 45° are very close to each other, except for the notched Iosipescu specimen, which deviates significantly. In comparison to the measurements taken with two points, it is interesting to note that in this case, the elongations are much greater. Considering the measurements taken with two points for Type B, Figure 37a, the curves obtained with the ASTM and BST block shear tests match for the considered thicknesses of 25 mm and 50 mm. In this case, the curves for the unnotched Iosipescu specimens, B_IOS and B_IOS*, match perfectly despite the two different test execution speeds. The notched Iosipescu specimen leads to significantly different results in this case as well. The slope of the bundles of curves up to 5% strain is almost the same, except for the notched specimen. The same considerations can be made regarding the measurements taken with virtual strain gauges in Figure 37b. In this case, the elongation values are greater compared to those of the measurements obtained with two points for the specimens tested with the block shear test. Type C foam's results, the softest one, are interesting because when observing the measurements taken with two points in Figure 38a and those taken with virtual strain gauges at 45° in Figure 38b, it can be noticed that in the first case, the curves follow the same bundle, while in the second case, Figure 38b, the Iosipescu and block shear groups diverge after approximately 40% strain. The observed deviation in the curves is likely because the virtual extensometers are not fixed at 45° during the measurement but become distorted to follow the direction of the principal strains, as will be evident from the qualitative analysis of the DIC maps. In this case as well, the results of the notched Iosipescu specimens do not follow the other bundles of curves.

Overall, it can be stated that for the same test type and measurement method, the curves match quite well even though the specimens have different thicknesses, respectively 25 mm and 50 mm. However, for the Iosipescu test, the results obtained with the notched specimen, which deviate significantly from the others, should be excluded. For this type of material, the notched Iosipescu specimen is not suitable because stress concentrations can occur at the notch root, compromising the

results, and the material tends to tear at the notch, significantly thinning the section. It is interesting to note that the block shear test specimens reach very high deformations, even exceeding 100% considering the measurements at 45°, while in all other cases, the elongation limits are relatively similar.

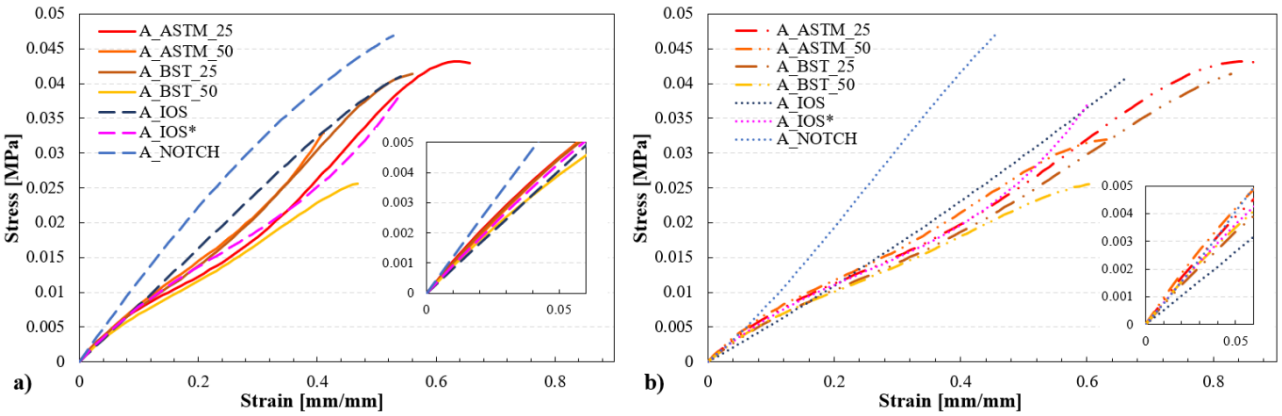

Figure 36 Type A foam comparison among stress-strain curves obtained from shear ASTM, BST and Iosipescu for each specimen geometry: a) measurements obtained by two points, b) measurements obtained by two virtual strain gauges.

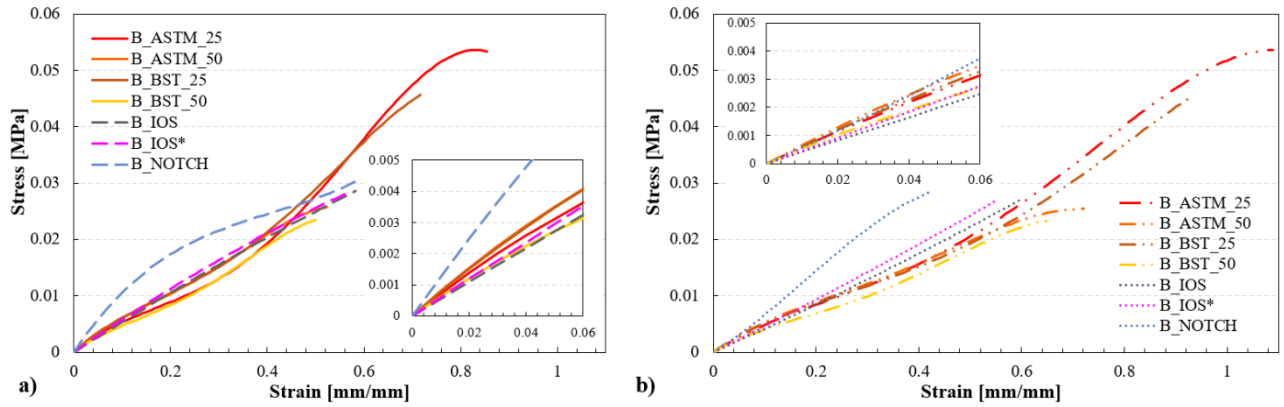

Figure 37 Type B foam comparison among stress-strain curves obtained from shear ASTM, BST and Iosipescu for each specimen geometry: a) measurements obtained by two points, b) measurements obtained by two virtual strain gauges.

Figure 39 and Figure 40 represents the comparison among type A, B, and C foams for ASTM C273 configuration with respectively 25 mm and 50 mm specimen versus the unnotched Iosipescu configuration. Measure obtained by two points (Figure 39a, Figure 40a) and by virtual strain gauges (Figure 39b, Figure 40b) are considered. Unlike the results of the block shear test, the results obtained with two-point and 45° measurements for the Iosipescu test align quite well. The unnotched Iosipescu configuration shows excellent results, as the curves obtained from this test closely resemble those of the ASTM C273 configuration for both thicknesses.

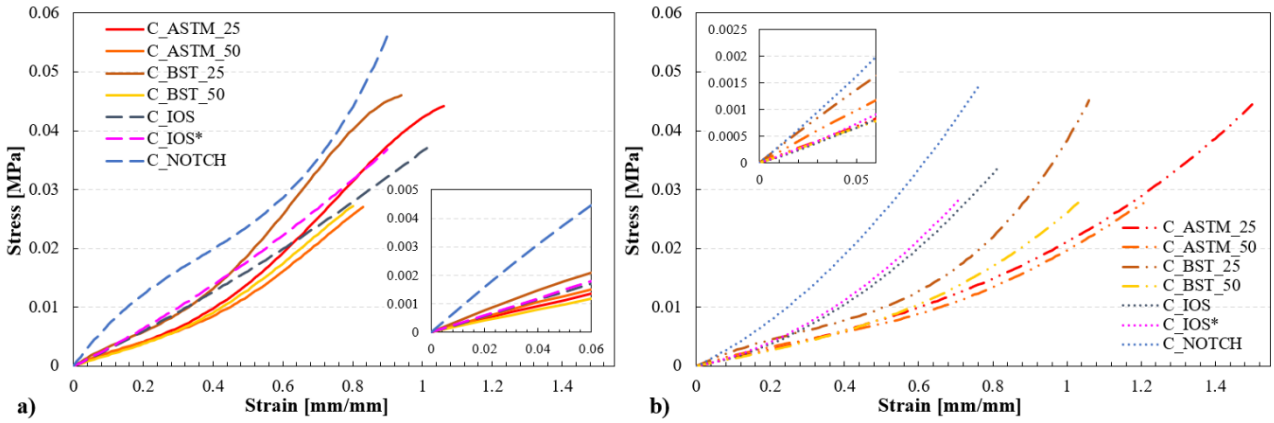

Figure 38 Type C foam comparison among stress-strain curves obtained from shear ASTM, BST and Iosipescu for each specimen geometry: a) measurements obtained by two points, b) measurements obtained by two virtual strain gauges.

This is also shown by the shear modulus results obtained up to 5% deformation reported in Table 12. The experimental shear moduli, $Gexp$, were calculated as described in equation 30 up to 5% strain, as the linear elasticity of this material type is limited to small deformations. As known, elastomeric foams can undergo tensile deformations exceeding 100% and compressive deformations exceeding 80%. The engineering shear modulus $Geng$, in equation 31, was calculated following the relation given by Gibson and Ashby in Cellular Solids [26], where the constant C_2 = 3/8, E_s is the elastic modulus of solid polyurethane that is around 45 MPa from Cellular Solids, ρ_s is the density of solid polyurethane that is around 1200 kg/m^3, and ρ^* refers to the density of the foam, which varies for the three considered foams. Table 12 also reports the elastic moduli obtained by testing the unnotched specimens with the Iosipescu configuration at a crosshead speed of 50 mm/min (IOS*). As mentioned earlier in the previous section, this type of test was necessary to assess any significant variations due to the strain rate. In fact, according to the standards, the block shear tests are performed at 50 mm/min, while the Iosipescu tests are performed at 20 mm/min. By comparing the column of results obtained with the unnotched specimens at 20 mm/min (IOS) and the column of the same specimens tested at 50 mm/min (IOS*), it can be stated that there are not significant differences considering the range of standard deviations.

$$Gexp = \frac{\tau}{\gamma} \tag{30}$$

$$\frac{G\,eng}{E_s} = C_2 \left(\frac{\rho^*}{\rho_s}\right)^2 \tag{31}$$

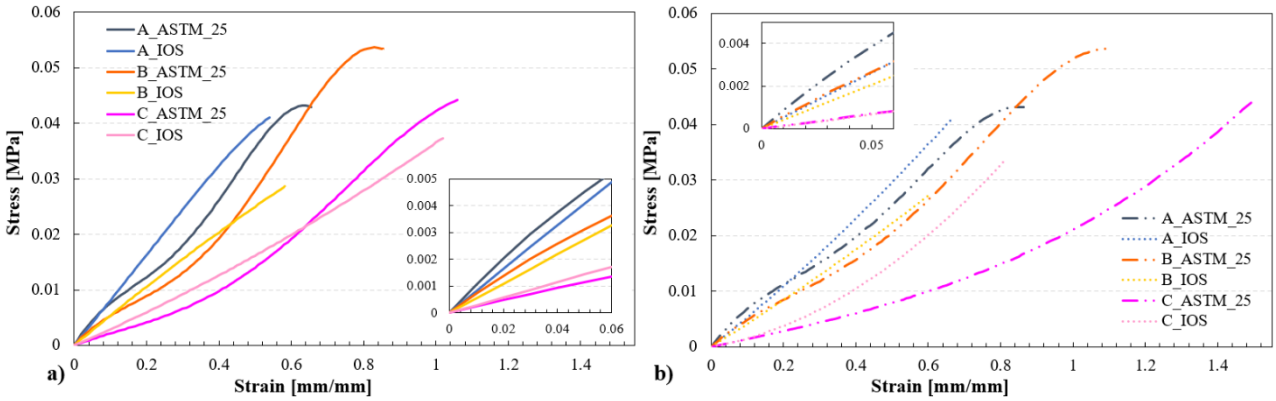

Figure 39 Comparison between stress-strain curves of the three foam types obtained from measurements obtained by points (A) and by strain gauges at 45° (b) for ASTM C 273 test with 25 mm thick specimen and for ASTM D 5379 (Iosipescu) test with unnotched specimen.

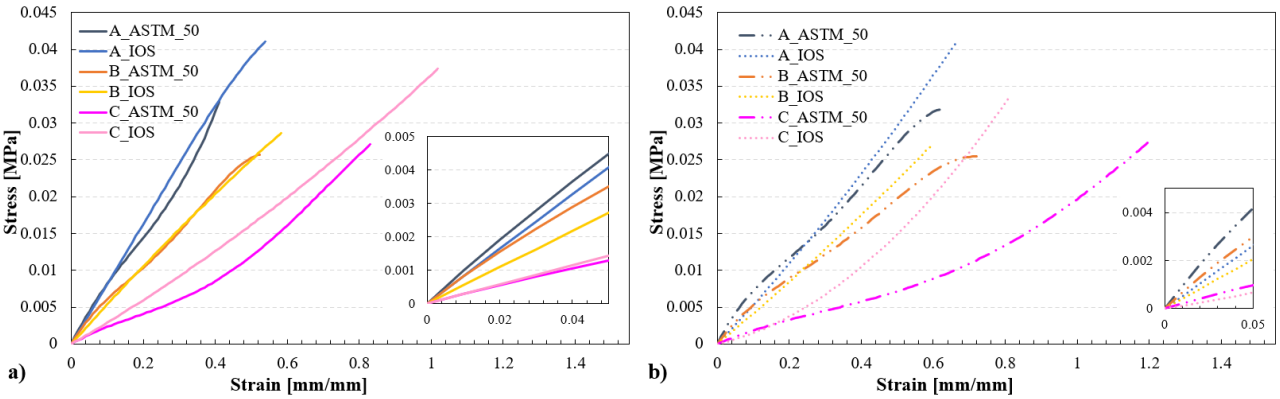

Figure 40 Comparison between stress-strain curves of the three foam types obtained from measurements obtained by points (A) and by strain gauges at 45° (b) for ASTM C 273 test with 50 mm thick specimen and for ASTM D 5379 (Iosipescu) test with unnotched specimen.

In Figure 41 Displacements along the Y-axis for: a) ASTM C273 with a thickness of 25 mm; b) ASTM C 273 with a thickness of 50 mm; c) BS 4370 with a thickness of 25 mm; d) BS 4370 with a thickness of 50 mm; e) ASTM D5379 with a non-notched specimen, f) ASTM D5379 with a notched specimen., the displacements along the Y-axis are shown for: a) ASTM C273 with a thickness of 25 mm; b) ASTM C 273 with a thickness of 50 mm; c) BS 4370 with a thickness of 25 mm; d) BS 4370 with a thickness of 50 mm; e) ASTM D5379 with a unnotched specimen; f) ASTM D5379 with a notched specimen.

Table 12 Elastic moduli calculated up to 5% deformation for ASTM and BS block shear tests and for ASTM D 5379 (Iosipescu) test considering different specimen geometries and measurements taken with two points and virtual strain gauges at 45°.

		G exp [kPa] 5% strain							Geng [kPa]
		ASTM 25	ASTM 50	BST 25	BST 50	IOS	IOS*	IOS_NOTCH	
Type A	**P**	90.1	95.8	88.8	78.5	98.8 ± 24	87.6	125.5 ± 23	84.7
	45°	79.2	86.0	67.9	71.7	72.9 ± 12	73.6	94.2 ± 19	
Type B	**P**	64.3	72.6	71.1	55.9	85.8 ± 33	59.0	100.9 ± 20	46.5
	45°	54.5	61.3	57.1	47.7	64.1 ± 20	45.9	75.9 ± 13	
Type C	**P**	23.1	19.6	36.5	19.9	23.8 ± 8	29.9	59.2 ± 16	24.8
	45°	13.8	20.0	27.8	13.2	11.5 ± 1	20.3	21.5 ± 11	

For the block shear tests, the larger displacements are marked in red, corresponding to the mobile crosshead moving downwards due to the tensile test. For the Iosipescu test, the major displacement is shown in purple since the mobile crosshead moves upwards due to the tensile test. It is interesting to note the formation of chromatic bands ranging from the largest to the smallest displacement, which are vertical for all configurations except the inclined one. A first influence of free edge effects can be observed in the ASTM C273 configuration with a thickness of 50 mm in Figure 41b. Indeed, the color bands at the ends fan out, as found in the study by G'Sell et al. [93].

In Figure 42, the displacements along the X-axis are represented for: a) ASTM C273 with a thickness of 25 mm; b) ASTM C 273 with a thickness of 50 mm; c) BST 4370 with a thickness of 25 mm; d) BST 4370 with a thickness of 50 mm; e) ASTM D5379 with a unnotched specimen; f) ASTM D5379 with a notched specimen. The map of displacements along the X-axis clearly shows the influence of undesired normal stresses (normal to the load direction), which are especially evident for specimens with a thickness of 50 mm. For instance, in Figure 42b, in the upper region, there is a large area subjected to compression shown in purple, while in the lower part, there is a large area subjected to tension marked in red. This phenomenon occurs similarly for the BST configuration in Figure 42d, although the map is less pronounced because the same scale was used for all block shear test configurations. In the 25 mm configurations, shown in Figure 42a and Figure 42c, a more extensive uniform area is observed in the central part, as indicated by the parallel color's bands. Regarding the Iosipescu test, there are edge effects in the unnotched specimen, as shown in Figure 42e, both in the upper and lower parts, but overall, the green region indicates a large uniform area devoid of normal stresses. For the notched Iosipescu configuration (in Figure 42f), large displacements are observed near the notch due to the rotation of the ends, making the uniform zone very small. The vector map of total displacements shown in Figure 43 is particularly interesting as it allows to verify the load

alignment conditions. In the ASTM setup (Figure 43a and b), the load axis is required to pass through the two upper and lower grips.

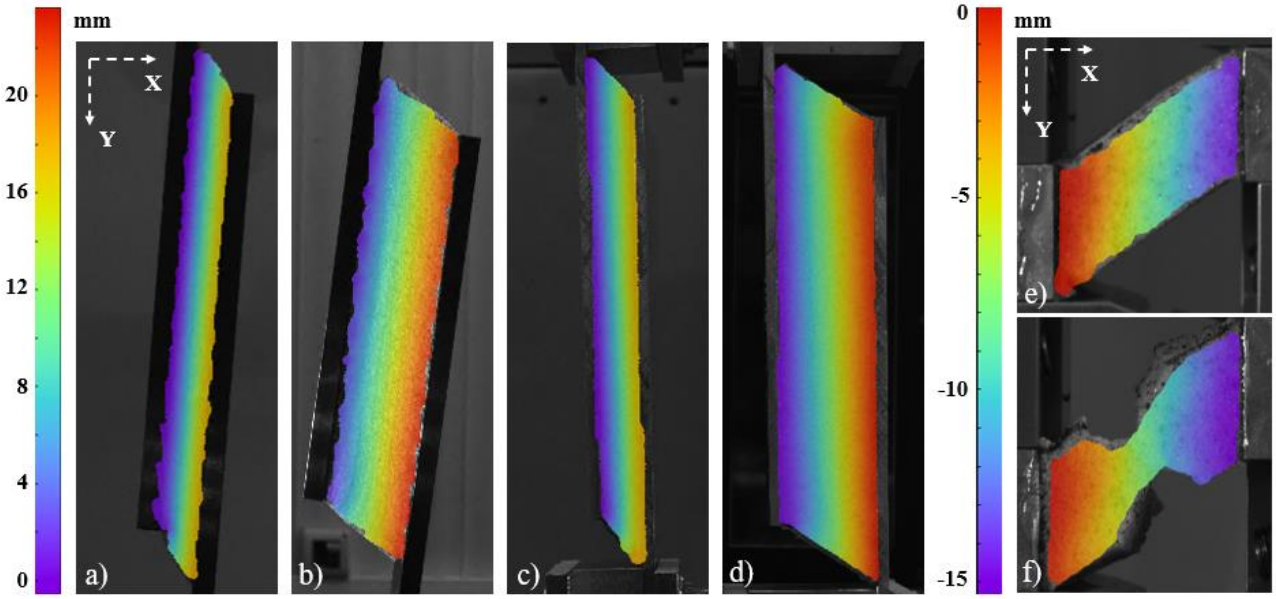

Figure 41 Displacements along the Y-axis for: a) ASTM C273 with a thickness of 25 mm; b) ASTM C 273 with a thickness of 50 mm; c) BS 4370 with a thickness of 25 mm; d) BS 4370 with a thickness of 50 mm; e) ASTM D5379 with a non-notched specimen, f) ASTM D5379 with a notched specimen.

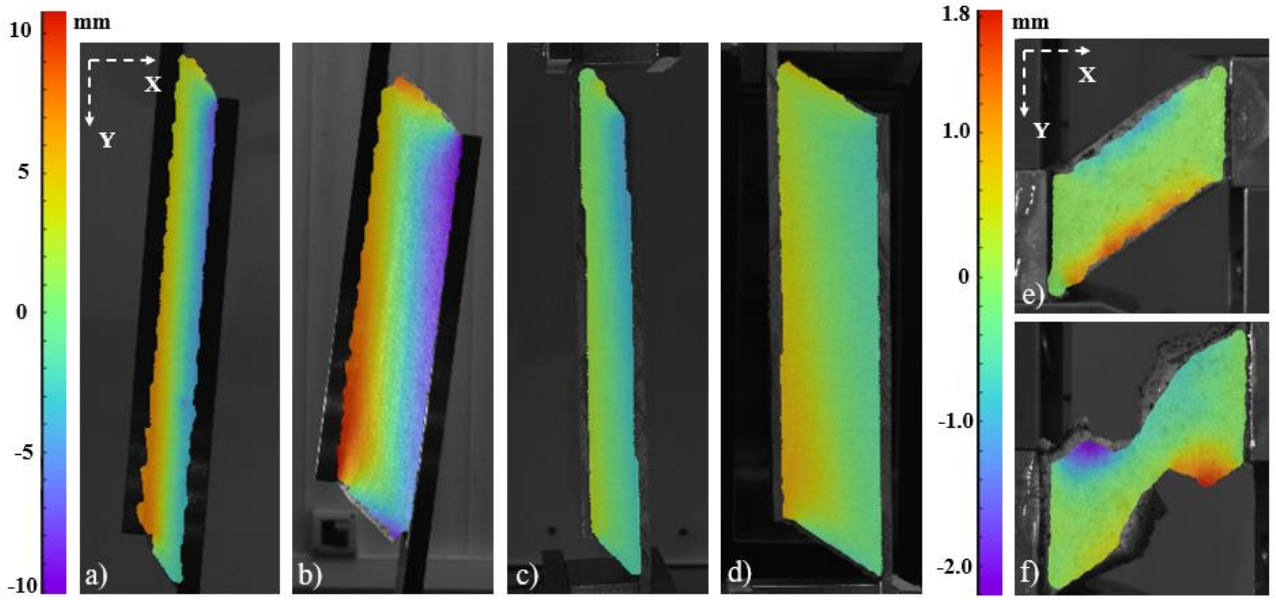

Figure 42 Displacements along the X axis for: a) ASTM C273 with a thickness of 25 mm; b) ASTM C 273 with a thickness of 50 mm; c) BS 4370 with a thickness of 25 mm; d) BS 4370 with a thickness of 50 mm; e) ASTM D5379 with an unnotched specimen, f) ASTM D5379 with a notched specimen.

This condition is satisfied for the ASTM specimen with a thickness of 25 mm, where the field of maximum displacement lies perfectly along this vertical. However, this condition is not satisfied for the 50 mm configuration (Figure 43b). For the BST configuration (Figure 43c, d) and the Iosipescu configuration (Figure 43e, f), the major total displacements occur at the mobile grip.

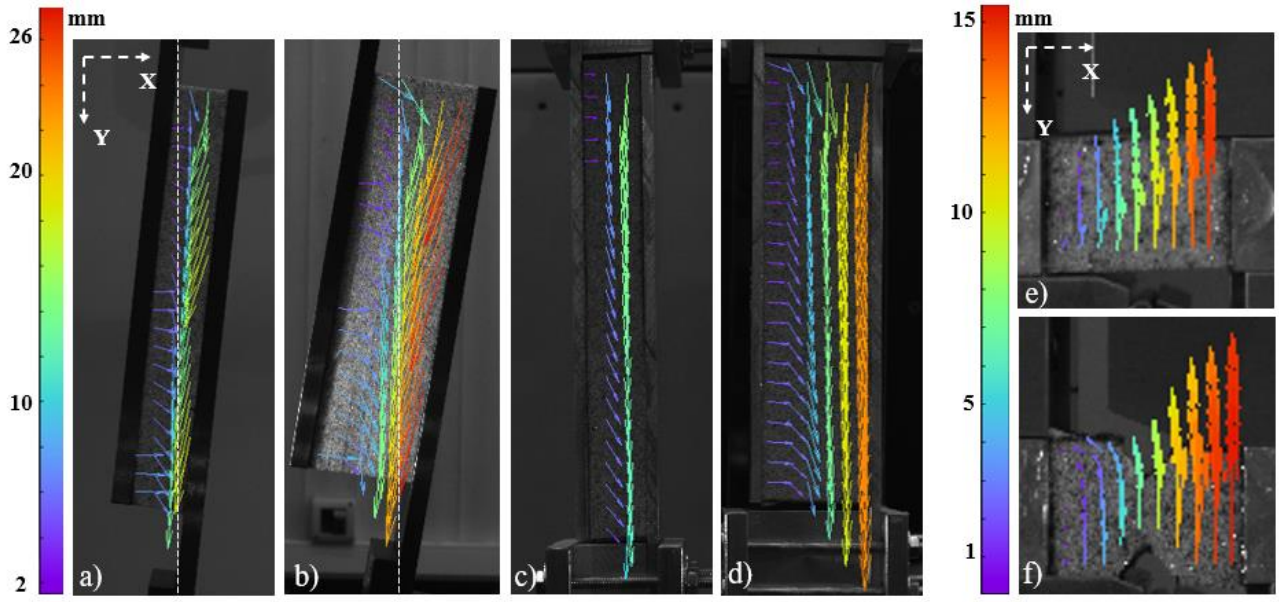

Figure 43 Vector map of total displacements for: a) ASTM C273 with a thickness of 25 mm; b) ASTM C 273 with a thickness of 50 mm; c) BS 4370 with a thickness of 25 mm; d) BS 4370 with a thickness of 50 mm; e) ASTM D5379 with an unnotched specimen, f) ASTM D5379 with a notched specimen.

Using the smoothing spline filter, local gradients were calculated, and the principal strains were represented along direction 1, as shown by the +45° hatching in Figure 44 for: a) ASTM C273 with a thickness of 25 mm; b) ASTM C 273 with a thickness of 50 mm; c) BST 4370 with a thickness of 25 mm; d) BS 4370 with a thickness of 50 mm; e) ASTM D5379 with an unnotched specimen, f) ASTM D5379 with a notched specimen. These maps are crucial for identifying areas with uniform gradients to determine the most appropriate measurement points. All edge effects are clearly identified in all configurations. Figure 45 (a) ASTM C273 with a thickness of 25 mm; (b) ASTM C 273 with a thickness of 50 mm; (c) BS 4370 with a thickness of 25 mm; (d) BS 4370 with a thickness of 50 mm; (e) ASTM D5379 with an unnotched specimen, (f) ASTM D5379 with a notched specimen, shows the principal strains along direction 2, represented by the -45° hatching. The principal strain 2 corresponds to the previously analytically calculated e_2 at -45°. In Figure 45a, a broader uniform zone is evident for the ASTM configuration with a thickness of 25 mm, and a uniform strain zone is also noticeable in the central part of the unnotched specimen in Figure 45e. The same considerations apply to the shear strain map represented in Figure 46 for: a) ASTM C273 with a thickness of 25 mm; b) ASTM C 273 with a thickness of 50 mm; c) BS 4370 with a thickness

of 25 mm; d) BS 4370 with a thickness of 50 mm; e) ASTM D5379 with an unnotched specimen, f) ASTM D5379 with a notched specimen. It is worth noting that for the unnotched specimen, the uniform shear zone extends from the region where the two points P_1 and P_2 were taken to the central area, explaining why the two measurements are almost overlapping.

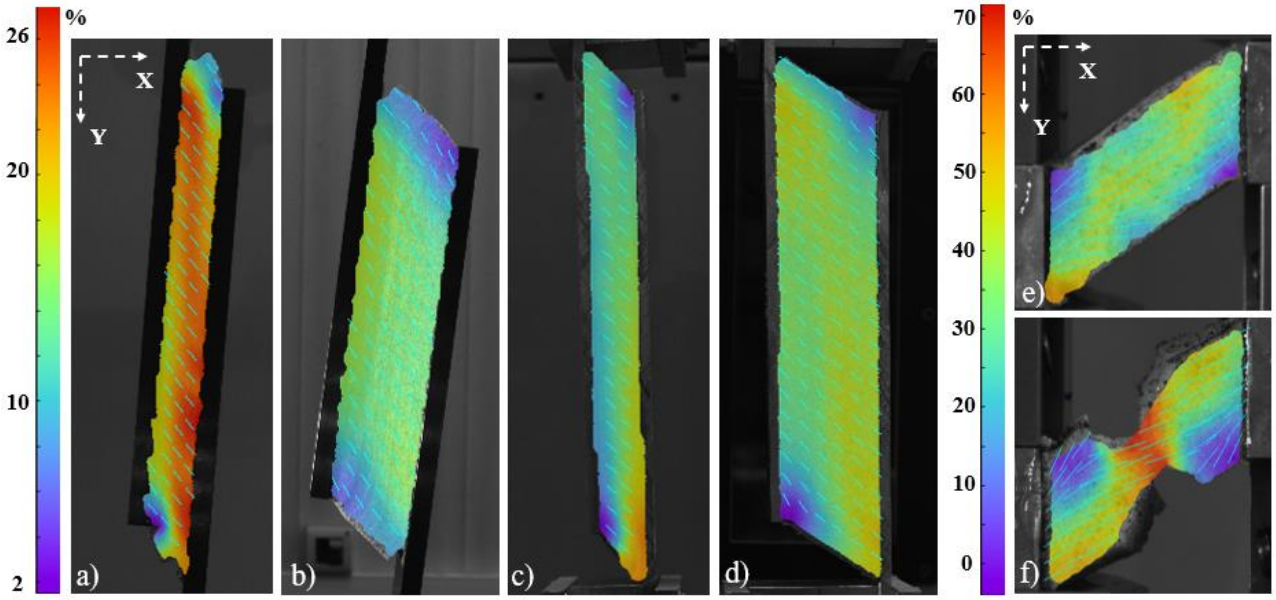

Figure 44 Principal strain 1 for: a) ASTM C273 with a thickness of 25 mm; b) ASTM C 273 with a thickness of 50 mm; c) BS 4370 with a thickness of 25 mm; d) BS 4370 with a thickness of 50 mm; e) ASTM D5379 with an unnotched specimen, f) ASTM D5379 with a notched specimen.

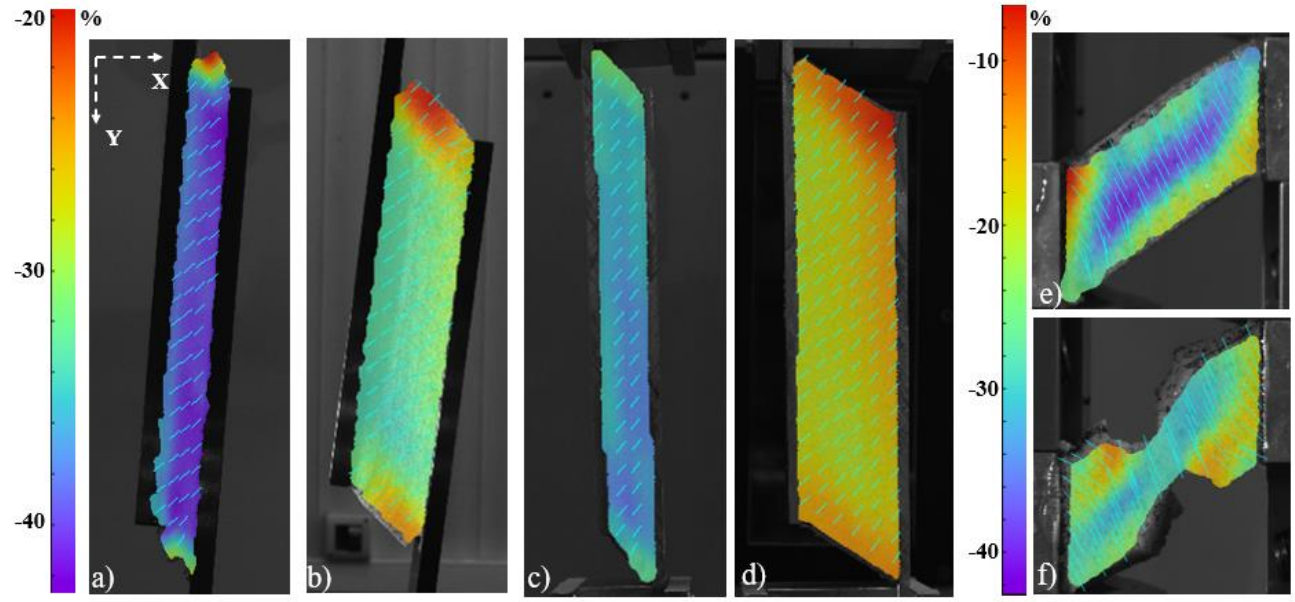

Figure 45 Principal strain 2 for: a) ASTM C273 with a thickness of 25 mm; b) ASTM C 273 with a thickness of 50 mm; c) BS 4370 with a thickness of 25 mm; d) BS 4370 with a thickness of 50 mm; e) ASTM D5379 with an unnotched specimen, f) ASTM D5379 with a notched specimen.

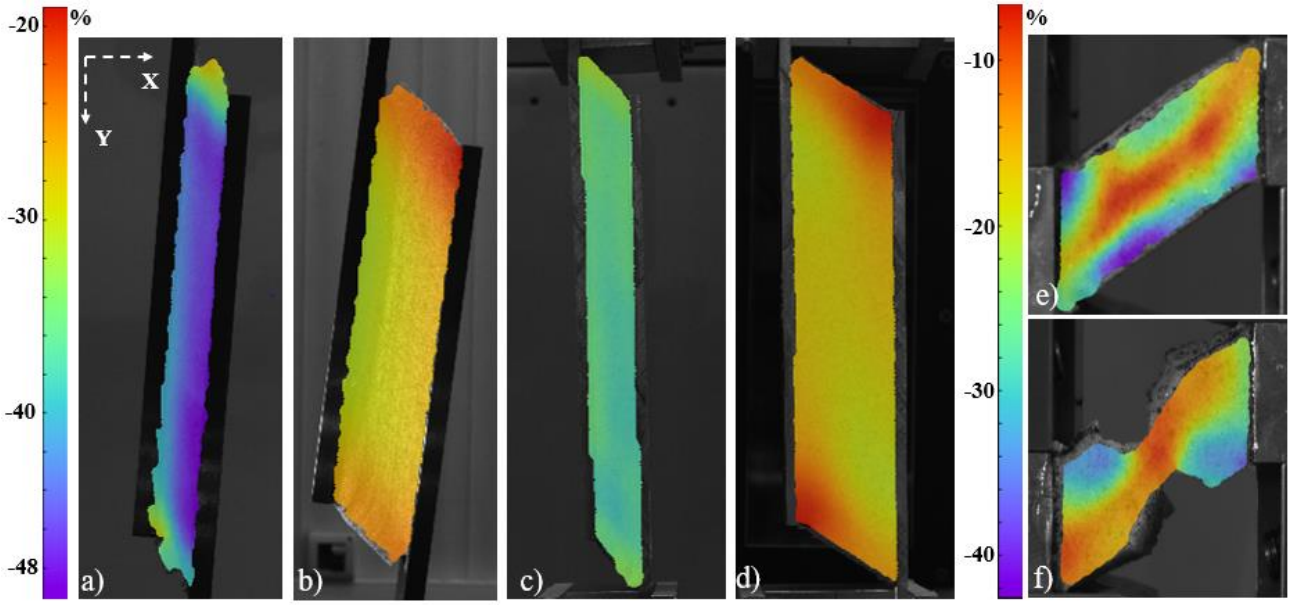

Figure 46 Shear strain for: a) ASTM C273 with a thickness of 25 mm; b) ASTM C273 with a thickness of 50 mm; c) BS 4370 with a thickness of 25 mm; d) BS 4370 with a thickness of 50 mm; e) ASTM D5379 with an unnotched specimen; f) ASTM D5379 with a notched specimen.

4.6. Cyclic Compression Test

4.6.1. Experimental setup

Cyclic compression tests were carried out in respect of UNI EN ISO 3386 [55] at room temperature. Cubic samples of 50 mm x 50 mm x 50 mm, shown in Figure 47a, were tested by the universal hydraulic test machine INSTRON 1342, equipped with a 10 kN load cell. Due to the limitations of available material, unfortunately only one test was conducted for each material. Specimens were compressed between the plates, as shown in Figure 47c, with a crosshead speed of 50 mm/min for the loading phase and of 10 mm/min for the unloading phase, to allow the sample always being in contact with the plates. Four deformation steps were set, respectively of 20%, 40%, 60% and 80% compared to the initial height of the specimens. Tests were conducted in displacement-controlled mode, so, before the test, the apparatus was calibrated and the distances to reach deformation levels of 20-40-60-80% were set. Stress-strain relations were carried out from loading data captured from the test machine at a frequency of 20 Hz and from displacement data obtained through the DIC technique at a frequency of 1 Hz. As for the other test, pre-load conditions were checked to be as low as possible.

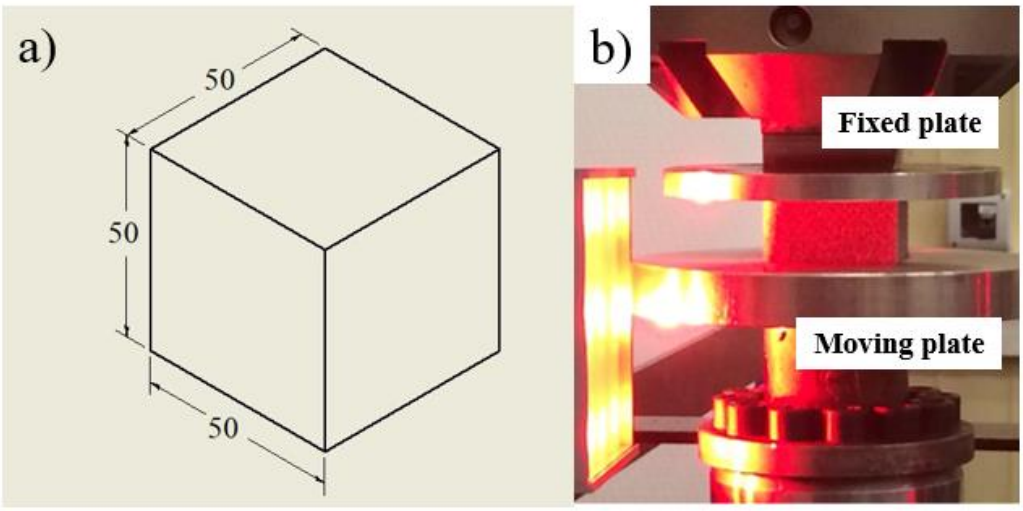

Figure 47 a) Cyclic compression test specimen (measure are expressed in mm), b) detail of tensile test fixture system.

4.6.2. Experimental Results and Discussion

As foams are mainly used as energy-absorbing devices, their compression behavior is surely the most studied one. Some authors [32,94–97] observed several relevant phenomena such as hysteresis loop and softening phenomenon, consisting in a gradual decrease of strength during the first cyclic loading [34] and known as the Mullins effect [60,98] already introduced in § 4.3.1. The Mullins effect indicates a stress softening phenomenon that takes place in primary loading and unloading cycles of a virgin specimen and manifests itself with a minor stress required to reach the same stretch of the previous loading cycle. A total of four loading and unloading cycles, in displacement-controlled mode, were carried out increasing the distance run by the actuator to determine the foam's behavior. Displacement map along the load direction (top row in Figure 48) and the transverse direction (bottom row in Figure 48) were obtained through 2D-DIC technique for a total of four compression steps, respectively for 20% step (Figure 48a and e), 40% step (Figure 48b and f), 60% step (Figure 48c and g) and 80% step (Figure 48d and h). The experiment was set in such a way that the piston ran 10 mm for the first step, 20 mm for the second step, 30 mm for the third and 40 mm for the fourth step, as consistently reported by the displacement map, considering a 50 mm cubic specimen. Due to the progressive cells' collapse, mostly in correspondence of the movable plate and progressively smaller getting closer to the fixed plate, horizontal bands are formed and they are clearly visible in the top row in Figure 48 for displacement in the load direction (Y). This bands have uniform color along the horizontal direction, appearing on the specimen in purple for greater displacements, while gradually fades in bands of the same color along the horizontal direction and becomes red at last, which corresponds to lower displacement according to the displacement color scale. The data

acquired by the camera and elaborated through INSTRA 4D software are reported in Figure 50 in form of stress-strain curves. Images in the bottom row of Figure 48 show that for 20% and 40% step the foam expands in both right and left direction while there is a diagonal, from the lower left corner to the upper right corner where the material seems to have zero deformation. As compression progresses, two symmetric bulges are formed for 60% (Figure 48g) and 80% (Figure 48h), one at the top left and one at the bottom right showing that not all cells collapse in the same direction, but they balance each other giving areas where the transverse deformation is zero, as shown by the color map. Furthermore, if in the first loading steps the foam expanded laterally, in the last steps the foam contracts. This effect is defined as an auxetic behavior of the material [48,62,99] which, as find out by some authors [100–102], is manifested by negative values of the tangent Poisson's function, that quantify the tendency of a material to distort and change volume. This topic will be deepened in the next paragraph. Displacement map show that the transverse contribution is very poor with respect to axial one. Due to the isotropy of the sample this clearly confirm that also out of plane component is negligible.

Full-field 2D-DIC is a powerful tool that permits to obtain not only the strain map of the entire surface of the specimen, but also the component of the deformation gradient tensor F defined as:

$$F_{ij} = \frac{\partial x_i}{\partial X_j} \qquad \text{(i, j = 1, 2, 3)} \qquad (32)$$

were X_j are the Cartesian coordinates and x_i are the deformed position coordinates.

For surface measurements the diagonal values, the principle stretches λ_1 and λ_2, are considered. Results at each measurement point are shown in Figure 49 for the axial (top row) and transversal (bottom row) direction, which are the main uniaxial compressive stress loading area of interest. In both axial and transversal direction, localization phenomena are clearly visible, especially in Figure 49a, b, g and h, in form of narrow bands or hot spots of different colors, indicating that the deformation fields are not homogeneous. This phenomenon takes place due to the collapse of the cell's structures while some neighboring cells do not change. A more uniform coloring is visible in Figure 49d and e, meaning that in the last step and in the first step, respectively for displacements in Y and in X directions, cells seem to collapse and flex slightly all in the same way in the entire specimens surface, while in Figure 49c and f an intermediate situation arises.

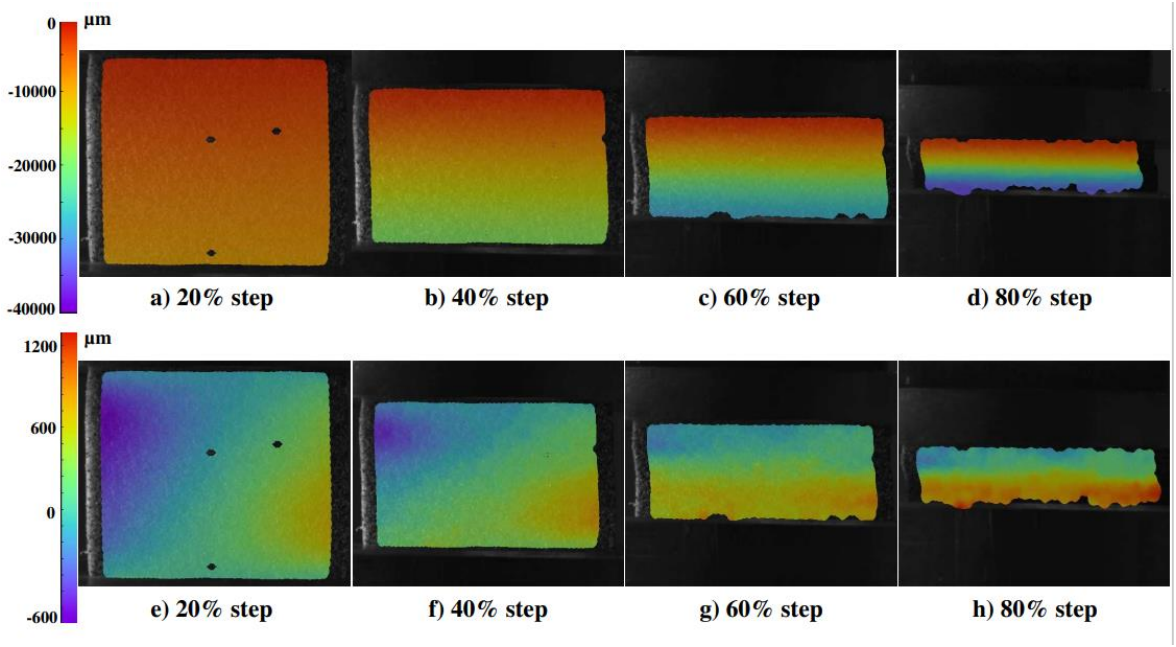

Figure 48 Compression load step of deformation and chromatic map (expressed in µm) for type A foam along the load direction Y (top row) and transverse direction X (bottom row)[15].

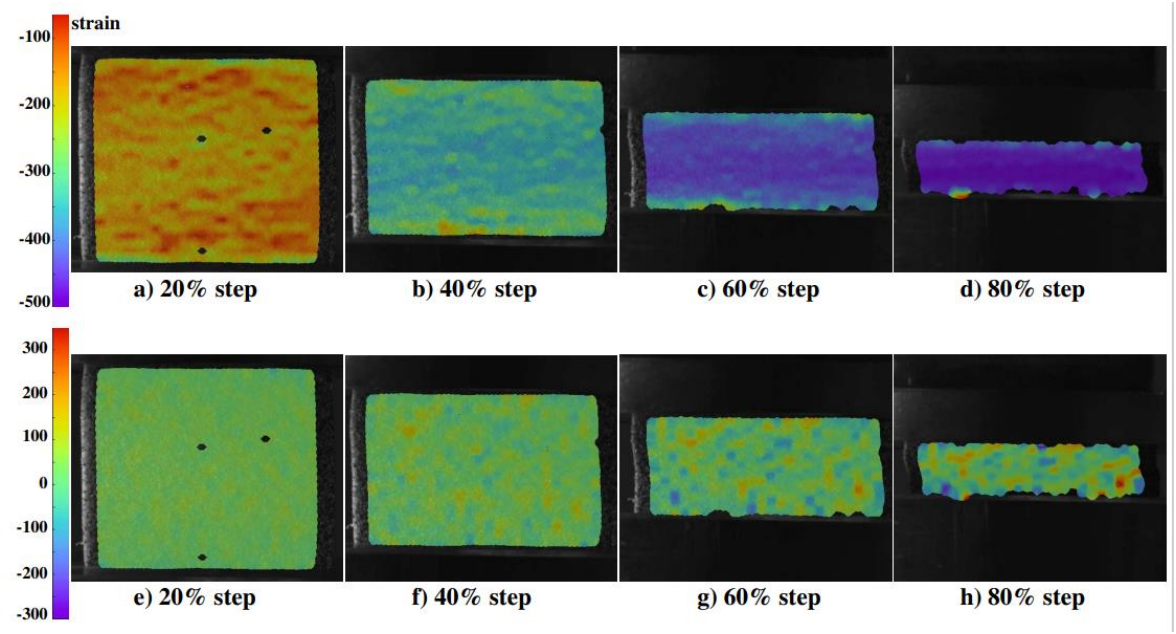

Figure 49 Principal deformation gradient component obtained in compression and chromatic map (expressed in strain) for type A foam along the load direction Y (top row) and the transverse direction X (bottom row) [15].

Overall chromatic maps in Figure 48 and Figure 49 clearly show that the deformation field is inhomogeneous, and the deformation gradient is not constant across the whole field at a given load step. These results are consistent with what is expected for a heterogeneous two-phases foam material

having different distribution of sizes, orientations, and cell wall thicknesses. By the subsequent analysis of compression loading phase in Figure 50 for type A (a), type B (b) and type C (c), three typical regions in cellular materials are observed, in particular a linear elastic branch is followed by a stress plateau characterized by a line roughly parallel to the horizontal strain axis; finally, an ascending branch is detected, in which the stress steeply rises (densification) [26,27]. The mechanisms associated with the collapse of the foam are differently depending on their nature. In detail, for a hyperelastic foam the first elastic region is given by the cell walls bending at low stresses; as the load increases, the cell walls begin to collapse due to a recoverable elastic buckling that presents a high strain level against a not significant stress increase. At higher stress levels the cells collapse sufficiently to oppose cell walls touch, giving the last region in which, the stress increases rapidly without an appreciable increase in strain. Focusing on different amplitudes of loading-unloading cycles it can be observed that during the unloading phase the curve does not follow the initial path but describes a large hysteresis loop in addition to a significant strength reduction between the first and subsequent cycles; finally, a progressively higher residual deformation was observed.

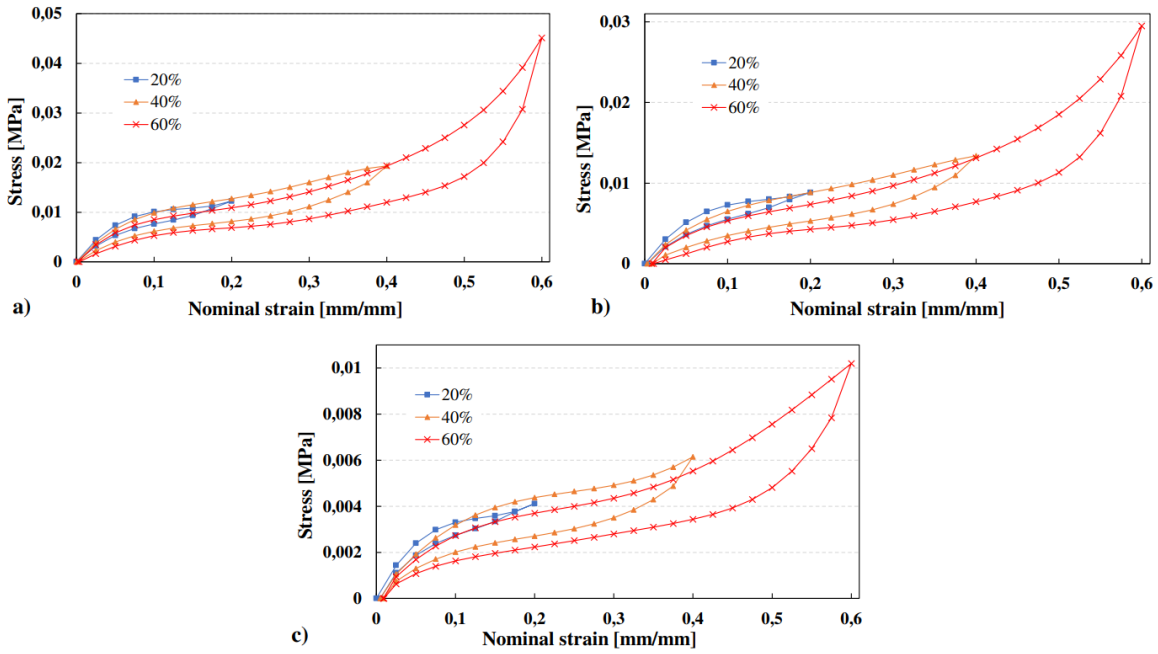

Figure 50 Loading and unloading curves for type A (a), type B (b) and type C (c) foam [15].

For clarity, taking type B foam as example, and considering only its load curves at 15% strain, stress values of 8 kPa, 7.8 kPa, 6.4 kPa and 5.1 kPa were recorded for the first, the second, the third and the fourth cycles respectively and residual strain values of respectively 0.28%, 0.87% and 1.1% for the second, the third and the fourth cycle. This happened due to a softening phenomenon that resembles the Mullins effect different from hysteresis, attributed to foams structure damage during

the first cycles compression (i.e., rupture of cell wall membranes, fracture of cell edges). Some studies [36,103,104] show that these effects tend to stabilize after subjecting the foam to numerous loading and unloading cycles. Curves in Figure 50 a, b and c are polynomial representations of appropriate order, the fourth cycle is omitted the allow good visibility of the other three cycles.
Observing the cyclic compression curves, it can be noted that the first part of each loading cycle presents progressively a minor slope, which corresponds to a lower value of E*. To examine this behavior the linear elastic modulus is computed following the same consideration and the same relation (eq. 19) exposed in § 4.4.2 for the first and the fourth compression cycle, namely 20% and 40% of strain. Results are summarized in Table 13, in which the plateau modules, E^*_{pl}, and the collapse plateau stress values, σ^*_{pl} for the two mentioned loading steps are also reported.

*Table 13. Plateau stress σ*pl and elastic modulus E*5% until 5% of strain and plateau modulus E*pl for the first and the fourth compression cycle (20% and 80% of strain).*

Specimen	σ_{pl} 20% [kPa]	$E_{5\%}$ 20% [kPa]	E_{pl} 20% [kPa]	σ_{pl} 80% [kPa]	$E_{5\%}$ 80% [kPa]	E_{pl} 80% [kPa]
Type A	10.3	159.5	23.7	7	110.7	24.1
Type B	7.2	125.7	14.3	4.4	87	16.4
Type C	3.4	73.7	6	2.3	38.7	5.8

The collapse plateau stress is obtained by the intersection point of the two linear approximations of the initial linear elastic region until 5% and of the plateau region, which slope is properly the plateau modulus [24]. From the first to the fourth cycle loading, the Young modules decrease of the 30% for type A and type B foam and of the 47% for type C foam, the plateau stress values decrease of the 32% for type A and C and of the 38% for type B, while the plateau modules differ slightly for all foams types. Although the Young's modulus of the material in tensile and in compression cycle should be very similar, in this study as well as in other authors' ones, the tensile modulus is higher than the compression one [105].

4.6.3. Energy absorbing characteristics

As stated in the previous paragraph, the foams' main purpose is to absorb a considerable amount of energy while keeping the force below some limit by undergoing to very large deformation. The area subtended by stress-strain curve represents the energy density per unit volume W, expressed in J/m^3, absorbed by the foam, as given by the relation (21):

$$W = \int_0^{\epsilon} \sigma d\epsilon \tag{33}$$

With reference to Figure 51, the maximum energy absorption of the foam under compression is represented by the plateau region, while a very low quantity of energy is absorbed in the linear elastic regime.

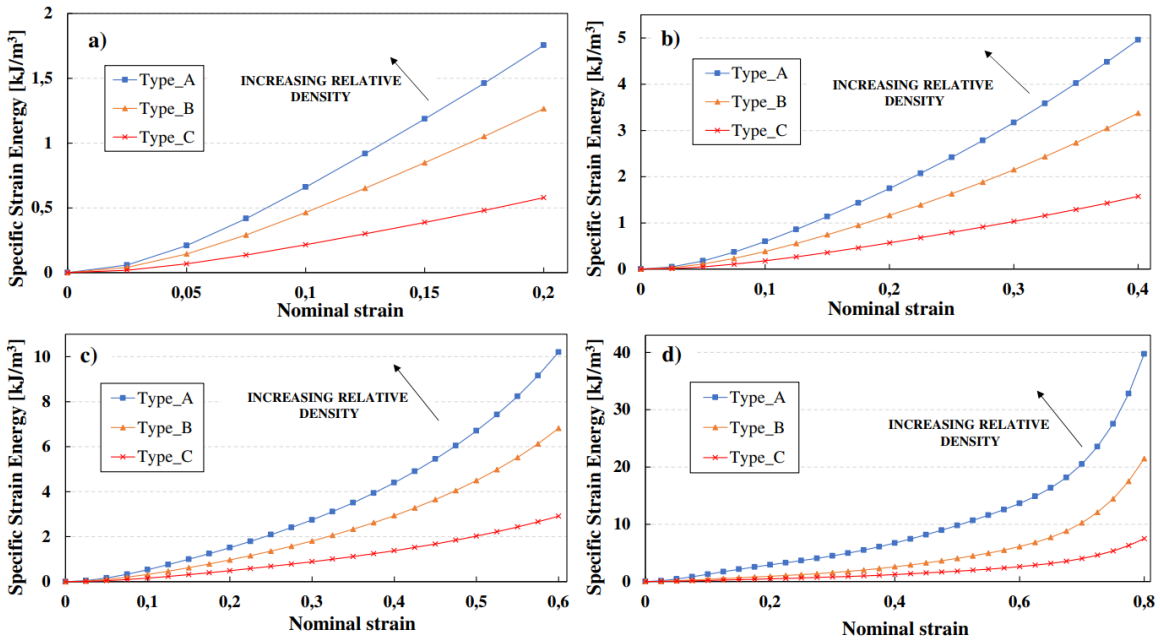

Figure 51 Strain energy density absorbed by each foam material for a) 20% strain, b) 40% strain, c) 60% strain and d) 80% strain [15].

The difference between the area subtended by the loading curve and the area subtended by the unloading curve gives the amount of hysteresis, which is the energy lost by the foam due to structural damage and heat dissipation. Of course, high hysteretic characteristic makes PU foams desirable for applications requiring low rebound and high energy absorption [106]. By observing the above cyclic compression curves and images in Figure 51, in which energy absorbing capability for each foam types are compared for a 20%, b 40%, c 60% and d 80% of strain step, it is clear that the material density has a significant influence on foams energy absorbing properties. The denser type A foam absorbs a considerable amount of energy compared to the least dense type C foam, while type B, of intermediate density, has intermediate characteristics. Furthermore, the absorbed energy always increases with the amount of deformation. In this regard, to choose the right combination of foam layers to absorb a certain amount of energy, a comparison between other foams type has to be made. For a hard open-cell polyurethane foam, with a density of 57.3 kg/m3, utilized as a ballistic protection helmet shell, the specific strain energy until 40% of the compression is 30 kJ/m3 [48]. This result is much higher than those reported in Figure 51 for the low-density flexible foam analyzed, it means that the hard foam can absorb higher amount of energy, consistent for its intended use. An interesting

comparison can be made also with a 3D printed thermoplastic foams used in packaging and tested in cyclic compression until 87% of strain. For this structured material the energy density reported values are 5.51 Mpa and 6.64 MPa respectively for the first and the second cycle [20], higher than those obtained in the present work. As can be deduced from the shown data, it is possible to choose the foam with the most suitable absorption characteristics depending on the use for which the material is intended. More generally, it is important to know the amount of energy that a foam can absorb and the maximum stress peak to be reached to choose the most appropriate one.

4.7. Can ordinary polyurethane foams be auxetic? Evaluation of the Poisson's ratio

Determination of Poisson's ratio of foams, particularly for the hyperelastic ones, has challenged analytical and experimental techniques due to the large deformations involved and their nonlinear behavior [101,107]. Poisson's ratio, ν, is a constant defined in the classical linear elasticity theory as the negative ratio of the lateral engineering strain to the axial engineering strain and it must satisfy $-1 \leq \nu \leq 0.5$ [100]. Based on this definition, ordinary materials which contract laterally when stretched and expand when compressed exhibit a positive Poisson's ratio. If a material expands under tension or contracts laterally under compression, its Poisson's ratio is negative and its behavior is defined auxetic [102,108]. More generally, Poisson's ratio is the primary metric for quantifying the tendency of a material to distort, rather than changing volume [100]. Embracing the mechanical properties of every isotropic material, from the most incompressible to the most extendable ones, Poisson's ratio has provided inspiration for creating new solids and liquids, and challenges in understanding existing ones [100]. Sometimes, as it happens with some biological and recently synthesized materials, ν is not constant and changes from positive to negative and vice versa. Literature review shows that for low-density polymeric foams, the Poisson's ratio varies strongly with the strain level. To adequately represent the instantaneous behavior of such highly nonlinear material, some authors propose the idea of a Poisson's function [48,62,102]. The description of the foams behavior through the Poisson's function can be advantageous for applications that require the use of auxetic materials, to optimize their use in mechanical applications with high impact loads or when a recovery of their original cellular structure and dimensions, with a return to a positive Poisson's ratio, is required [99]. Indeed, materials with negative Poisson's ratio are particularly suited for body armors, protective equipment or to improve crashworthiness of seats due to more uniform pressure distribution as well as better vibration protection [99,109–111]. The use of full-field deformation measurements on soft, open-cell, low-density polymeric foam to investigate the Poisson's ratio effect during tensile and cyclic compression loads, under great deformations, is still a topic to be explored [16]. As well as there is a lack of studies exploring the variation of the Poisson's ratio when the material undergoes to large deformations (up to 90% in traction and 80% in compression) implementing FEM analysis[16]. In

this section the study is aimed to characterize the Poisson's ratio of three soft open-cell polyurethane foams of different densities, comparing them each other and with those analyzed by other investigators. The analyzed foams are intended to be used for aeronautical seats, so that auxetic behavior of the foams should be assumed as an advantage both for the seats' comfort and for costs' reduction reasons, as it would avoid further processing for making them auxetic. It is well known that cellular materials behave differently depending on the way they are stressed. Studies on standard (untreated) foams report positive values of the Poisson's ratio in tensile test [112] and marginally negative values in compression [62,113]. No one has reported the trend of the Poisson function in case of cyclic compression, nevertheless this is important for this kind of materials used mainly in compression and exhibiting effects such as hysteresis and stress softening phenomena that take place in primary loading and unloading cycles of a virgin specimen [32,34,95]. For the tensile behavior, the most detailed work is that of El-Ratal and Mallick [112] who traced the curves for an apparent Poissons's ratio versus the major stretch ratio (λ).

The evolution of the Poisson's ratio in uniaxial tensile and cyclic compression test can be identified thanks to the data available transverse and along the load direction. Due to the nonlinear behavior of the analyzed materials a Poisson's function and a tangent Poisson's function formulation were used [102]. The stress-strain curves and the lateral versus axial strain ones have been proposed in engineering form and considering the true data. The numerical models reproduce the trend of the experimental curves up to 90% of strain and 80% of strain for the tensile and the cyclic compression test in both forms considering or not the transverse or lateral strain data of the specimens.

4.7.1. Poisson's function

The Poisson's ratio, ν, is a material constant ruling the transverse deformation of an isotropic material during the linear elastic regime of deformation. It is defined as the negative ratio of the lateral engineering strain, e_x, to the axial engineering strain, e_y:

$$\nu = -\frac{e_x}{e_y}. \tag{34}$$

Equation 6 must satisfy $-1 \leq \nu \leq 0.5$ [100] according to the thermodynamic considerations of strain energy in the elasticity theory [114]. While the Poisson's ratio is strictly defined for linear elastic materials under small deformations, on the contrary for nonlinear materials, such as hyperelastic foams, a rigorous definition does not exist [102,113]. Furthermore, for low-density soft polymeric foams the Poisson's ratio is not constant but it varies strongly with the strain level. So, for such type of materials the expression in Eq. 34 will represent the secant Poisson's ratio when the trend is obtained for every small increment of load as a function of the global strain [48]. In contrast to the secant modulus, some authors [48,102] proposed a tangent Poisson's function defined as:

$$\nu_{tan} = -\frac{de_x}{de_y} \tag{35}$$

able to highlight the instantaneous value of the Poisson's ratio. The expression in Eq.35 is given by the tangent of the lateral-axial strain curve, expressed as a function of the global strain, for every load increment. For more details on the computation of the strain see Ref. [102,112]. Dealing with large deformations and with a non-linear behavior, true stress data, σ_T, referred to the actual cross-sectional area of the specimen, were calculated using a relation which considers point by point the engineering stress and strain data (σ_i, e_i), and the actual value of the Poisson ratio ν_i [115,116]:

$$\sigma_{T_i} = \frac{\sigma_i}{(1-\nu_i e_i)^2} \qquad 0 \leq i \leq t. \tag{36}$$

4.7.2. Tensile Text: experimental and numerical results

Experimental tests results were already discussed in § 4.4.2, in this section the focus is on the evolution of the Poisson's ratio during the tensile test and on the numerical modeling of the material behavior considering or not the Poisson's ratio.

The evolution of the Poisson's function, namely the ratio between the lateral on the axial engineering strain plotted against the global tensile nominal strain, is reported in Figure 52a. The reported best curves show a similar trend for the three foams, starting from zero the function grows and then settles at almost constant values. In particular, the higher density foam shows a behavior almost identical to the softer one. However, the last one displays a greater striction and for this reason the related curve is shifted upwards. Considering the average of the entire approximately horizontal curves of Figure 52a, ranging from 20 to 40% of strain, values of ν = 0.262 for type A, ν = 0.316 for type B and ν = 0.314 for type C foam can be found. As already seen by other authors for compression, the tangent Poisson's function, which is presented in Figure 52b for the tensile test, marks the instantaneous behavior of the material by placing itself as a magnifying glass allowing a discussion on deformation mechanism.

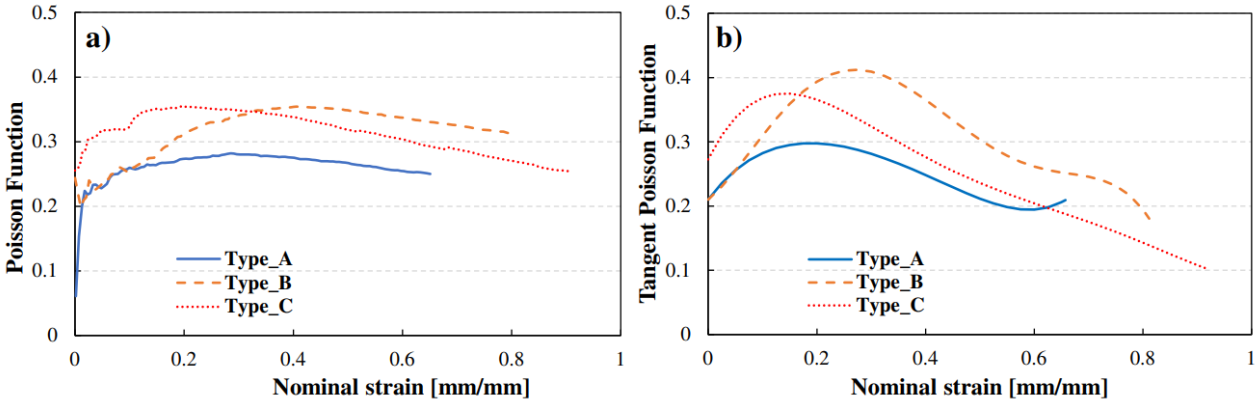

Figure 52 Evolution of the Poisson's function (a) and of the tangent Poisson's function (b) with nominal tensile strain for Type A, Type B and Type C soft polyurethane foam [16].

Starting from the undeformed configuration as the load increases the cell-edge bends, from a macroscopic point of view, it means that the lateral section of the specimen becomes thinner. This results in an increasing trend of the tangent Poisson's function curves. In particular, Gibson and Ashby [26] reported that the cell walls are substantially aligned with the tensile axis after a strain about 30%. This is confirmed by the trend of the ν_{tan} curves, in fact, for type A and type B foam, after the 20-30% strain the tangent function decreases while for the softest foam this behavior can be observed before 20% of strain. By now the cell walls have aligned and further strain requires the plastic extension of the cell walls themselves until they tear. Curves in Figure 52b, unlike those shown in Figure 52a, have a maximum value of ν_{tg} = 0.298 for type A, ν_{tg} = 0.412 for type B and ν_{tg} = 0.374 for type C foam.

Table 14 Finite element model constants obtained using tensile stress-strain curves considering ν = 0, ν = const and the lateral strain data, ν, for N=1 [16].

		μ [MPa]	α	ν
	ν = 0	1.1886e-01	2.8217	0.0000
Type A	**ν**	8.9402e-02	3.6232	0.3094
	ν = const	9.2108e-02	3.3814	0.2980
	ν = 0	7.1251e-02	3.3356	0.0000
Type B	**ν**	5.0767e-02	4.4099	0.3017
	ν = const	5.3827e-02	3.9331	0.4120
	ν = 0	5.3280e-02	2.8636	0.0000
Type C	**ν**	3.8802e-02	3.6140	0.3854
	ν = const	3.9852e-02	3.4229	0.3740

To better understand that aspect a numerical model was implemented in Abaqus 6.13-1 considering three different cases: $\nu = 0$, a constant value of ν equal to the maximum value identified by the tangent Poisson's function and, finally, providing the lateral experimental strain data point by point. In the latter case the software, through an algorithm, calculates one or more Poisson's ratio according to the order N of the strain energy potential (§ 4.3). For the tensile tests the best fit was obtained with N = 1 and the *hyperfoam* material constants, including a single value of the Poisson's ratio (ν) as summarized in Table 14.

Observing the ν values shown in Table 14, for type A and type C the values obtained considering the nominal lateral strain point by point is quite similar to the value corresponding to the maximum point of the tangent Poisson's function while for type B the two values differ completely. However, these values differ completely from $\nu = 0.33$ suggested in the *Mechanical behavior of elastomeric foams* section of Abaqus CAE guide [59] for this kind of materials.

The sequence of images in Figure 53 shows the comparison between the chromatic maps (Figure 53a and b) as obtained by DIC and the corresponding output obtained by the numerical simulation considering $\nu = 0$ (Figure 53c and d) and ν = const (Figure 53e and f). The images of the numerical simulations obtained using point by point the nominal lateral strain data have not been reported because they are very similar to those obtained considering ν = const. The chromatic maps in Figure 53a and b represent the Y and X displacement maps of the specimen under loading. Concerning the load direction, coherently with what is expected, the experimental chromatic map shows the major displacements in purple (54 mm), in correspondence of the upper movable clamping, and the minor displacements in red (16 mm), in correspondence of the lower fixed clamping. Observing the experimental results for the direction transverse to the load is possible to see that the material is shrinking and that there is a zero-displacement area in correspondence of the vertical axis of the specimen. By comparing experimental and numerical displacement results, it is clear that the numerical model predicts with high accuracy the displacements along Y and X direction, obviously excluding the displacements along X when $\nu = 0$, where the section remains constant (Figure 53d).

The experimental best curves in Figure 54 were presented considering the engineering and the true stress-strain data, computed through the relations reported by equations 18 and 36. Regarding the numerical results, the default stress measure used in Abaqus is Cauchy or true stress while it is possible to directly extrapolate the logarithmic strains (LE) or to calculate the engineering strains considering the displacements of the nodes in points similar to those taken on the real specimen through the DIC. For the case $\nu = 0$, since there are no section's variations, the engineering data were considered. Observing the stress-strain curves in the top row of Figure 54 it is possible to note that the experimental engineering curve is faithfully reproduced by $\nu = 0$, with a difference for the maximum reached stress of 5.2%, 6.2% and 8.4% respectively for type A, type B and type C. The

trend of the true stress-strain curves both in the experimental and in the numerical case (ν = const, ν) well overlaps those of the engineering results up to just before 20% of strain for all three foam types. Beyond this limit, given the extremely non-linear behavior of the material, true data are more accurate.

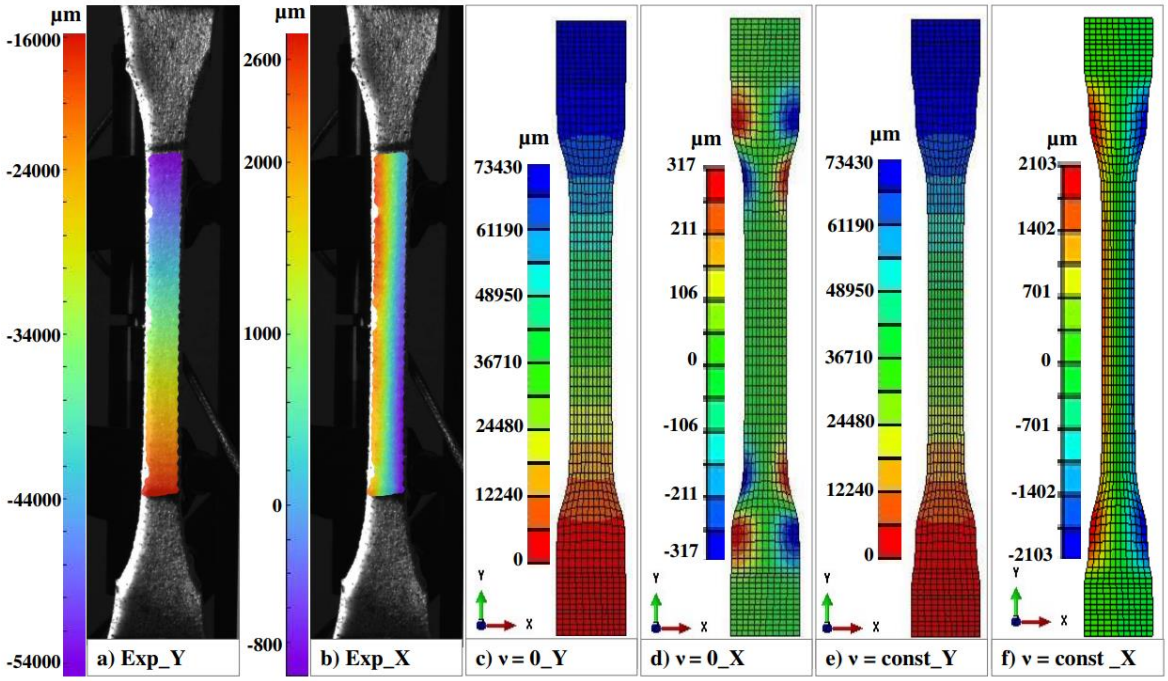

Figure 53 Experimental tensile test chromatic map of the displacement field for type B foam at the maximum load along Y(a) and X(b) direction, corresponding FEM results along Y(c) and X(d) direction considering ν = 0 and FEM results along Y(e) and X(f) direction obtained considering a constant value of the Poisson's ratio [16].

Overall, it can be stated that the true experimental stress-strain curve is well reproduced both considering the nominal lateral strain data point by point and considering ν equal to the maximum point of the tangent Poisson's function.

Specifically for type A, the numerical curve obtained considering all the nominal lateral strain data perfectly overlaps the experimental one. The maximum stress value reached considering the true experimental data differs by 1.1% from that obtained considering the nominal lateral strain data and by 3.1% from that obtained considering ν = 0.298. For type B, the true experimental curves differ slightly from the corresponding numerical ones only between 35% and 45% of deformation. The maximum stress value reached considering the true experimental data differs by 1.0% from that obtained considering the nominal lateral strain data and by 0.5% from that obtained considering ν = 0.412. Even for the softer type C foam, the true experimental curve slightly deviates only around 40% of strain. The maximum stress value reached considering the true experimental data differs by

8.7% from that obtained considering the nominal lateral strain data and by 3.4% from that obtained considering ν = 0.374.

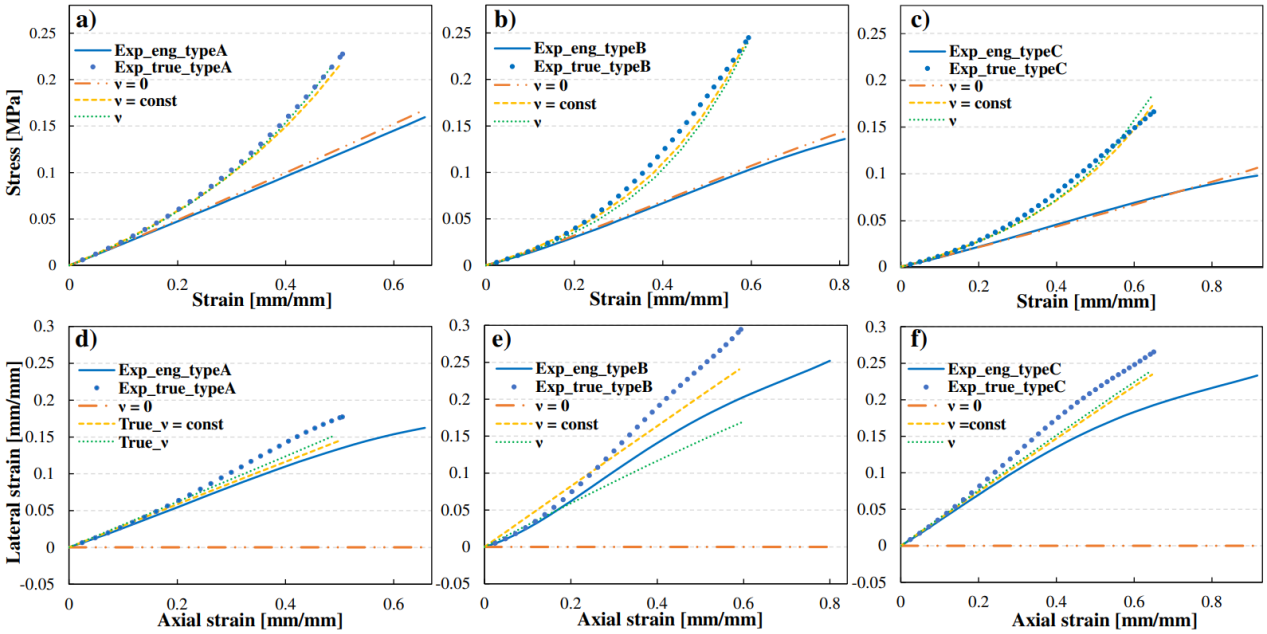

Figure 54 (Top row) Comparison of the experimental engineering and true tensile stress-strain curves with those obtained by numerical simulations considering ν = 0, ν = const and the lateral nominal strain point by point for Type A (a), Type B (b) and Type C (c) soft polyurethane foam. (Bottom row) Comparison of the experimental engineering and true axial versus lateral tensile strain curves with those obtained by numerical simulations considering ν = 0, ν = const and the lateral nominal strain point by point for Type A (d), Type B (e) and Type C (f) soft polyurethane foam [16].

The graphs in the bottom row of Figure 54 for type A (d), type B (e) and type C (f) foam show the reproducibility of the true lateral strain versus true axial strain data. For the sake of completeness, the experimental curve obtained considering the engineering strains is also shown, whose slope allows obtaining the tangent Poisson's function. Overall, for type A and type C the true experimental curve is well approximated by the two numerical formulations, with a slightly greater correspondence for curves obtained by considering the lateral strain. For type B, on the other hand, the curve obtained with ν = const is closer to the experimental one. In all the three cases it is shown that considering ν = 0 leads to a complete loss of information on the strain in the direction transverse to the load. Concerning the Poisson's ratio, it is interesting to compare the results obtained in this study with those of other authors. El-Ratal and Mallick [112] tested in uniaxial tension two different flexible polyurethane foams up to about 40% of strain, founding, for the seat foam, ν = 0.260 at 22% of strain and 0.387 at 29% of strain, comparable to those obtained in this study. Subsequently, Murphy and Rogerson [117] developed a finite elasticity theory which, through a power law relationship, successfully reproduces the experimental data of El-Ratal and Mallik up to 40% of tensile stain.

4.7.3. Cyclic compression test: experimental and numerical results

Since foams are mainly used as energy-absorbing devices, their compression behavior is surely the most studied one. Some authors [48,111] studying polyurethane foams in simple compression, found that they behave in an auxetic way and that there is an inversion of the material behavior after 20% of the nominal axial strain of the material. In this study the cyclic compression behavior of soft polyurethane foams was deeply analyzed to understand the incidence of phenomena such as hysteresis loop and softening (gradual decrease of stiffness during the first cyclic loading) [32,34,94,96,97] on a possible auxetic behavior of these foams. From this point of view, it is interesting to understand what happens to the displacements occurring in the transverse direction of the specimen when foams are subjected to a cyclic load. In this regard, Figure 55 represents the experimental transverse nominal strain against the image frame number during the four cyclic compression steps for the three foam types. To keep the image understandable each load cycle (20, 40, 60 and 80% of compression) was annotated with curly brackets that enclose the start and the end of the image frames, the end of the loading phase was indicated by a red star placed in correspondence of zero lateral strain, while the transition point was indicated by a red triangle in correspondence of 0.02 lateral strain. The first part of the curves represents the first loading and unloading phase until 20% of Y-strain in which with the application of low compressive axial strain the foams start to expand laterally, behaving in a conventional manner. The three foams, at the end of the first loading phase, present a similar lateral expansion, just below 2%. When the load is released, the foam recovers its initial shape, while maintaining a residual deformation, in fact at the end of the first cycle the curve does not return to zero. As it can be seen from the graph, the residual deformation along X becomes increasingly marked as the level of deformation increases. In the second cycle a deformation of 40% is reached along Y, it can be noted that in the same loading phase, at about 2% of the lateral strain value, there is a trend reversal, indicated by the transition point. This phenomenon similarly occurs at the same lateral strain level also for the third (60% Y-strain) and the fourth (80% Y-strain) loading cycle. This means that at the beginning of each load phase the lateral strain increases as the foam is compressed and that the transition point appears surely after 20% of nominal compression axial strain (in fact it is not well evident at the first cycle). So, after 20% of compression, the lateral strain decreases with the same slope of the conventional part, which indicates that the specimen contracts with further increase in compression. This behavior, reported by Koumlis and Lamberson [48] for a hard foam tested in simple compression until 80% of axial strain and by Brincat et al. [111] for a standard open cell PU foam tested in simple compression until 75% of axial strain, demonstrates the auxetic behavior of the foam.

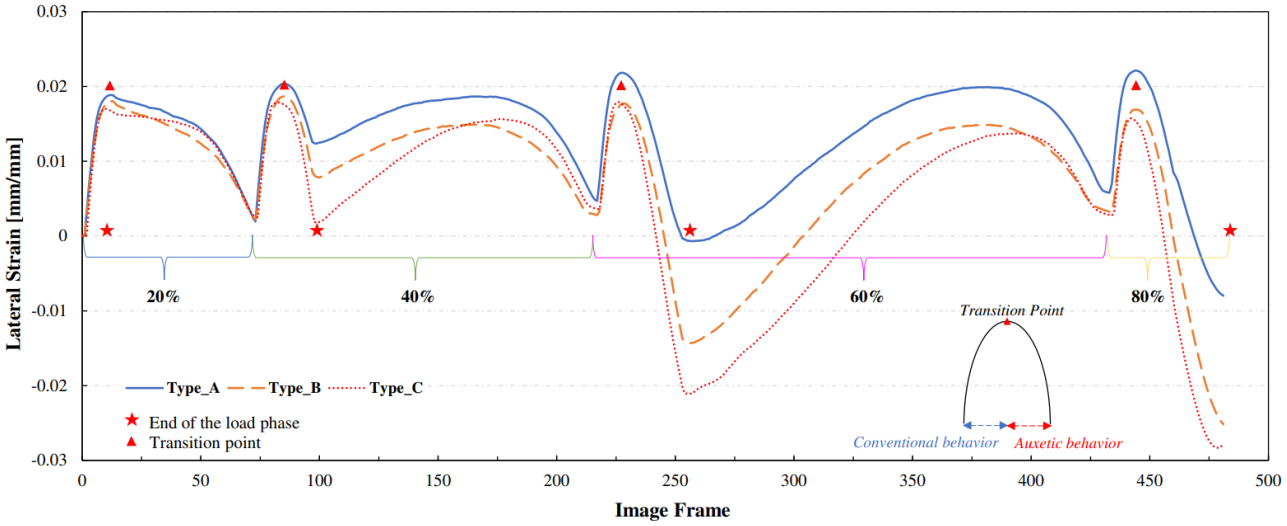

Figure 55 Experimental lateral nominal strain against the image frame obtained in cyclic compression for the loading and unloading phase of 20%, 40% and 60% of strain and for the load phase of 80% of strain [16].

The Poisson's function (curves in the left column of Figure 56 for type A (a), type B (c) and type C (e)) and the tangent Poisson's function (curves in the right column of Figure 56 for type A (b), type B (d) and type C (f)) also supports what has been identified by the trend of the lateral strain shown in Figure 55. For simplicity, a positive nominal strain axis was considered. From the comparison of the curves obtained for the same material in Figure 56, in respect to the classical definition of the Poisson's ratio, namely the secant Poisson ratio in the study of Koumlis and Lamberson [48], the tangent formulation (Eq.35) highlights the instantaneous tendency of a material to distort and change volume. It is interesting to note the differences between the denser type A foam and the other types B and C. As the density decreases, the foam reaches negative values of the Poisson function at increasingly lower strain values, in fact this occurs at 56%, 46% and 40% of axial strain respectively for type A, type B and type C foam. In the tangent formulation, type A foam begins to behave in an auxetic way at 16% of strain for all load cycles, consistently with what is shown by the trend inversion of the curve in Figure 55 which has already been discussed. For type B and type C foam there is a small deviation for the tangent formulation with respect to foam A. Indeed, the first and the second cycle curves both reach negative values after 16% of strain (type B) and the 12% of strain (Type C). The third and fourth cycles become negative at different times, which deviate by a $\Delta = 4\%$ of strain for both type B ($\nu < 0$ at 14% of strain at the third cycle and $\nu < 0$ at 18% strain at the fourth cycle) and for type C ($\nu < 0$ at 10% of strain at the third cycle and $\nu < 0$ at 14% strain at the fourth cycle). Once densification is reached, towards 80% of strain the three foams come back towards $\nu = 0$. Physically it happens that for the first two cycles the foam starts to deform by bending of the ribs, acting in a conventional manner, then the cells subjected to compression expand but beyond a certain

threshold, the ribs around the void adopt a re-entrant conformation. After the loading phase the foam recovers its initial shape, although showing a slight residual deformation along both X and Y axis (Figure 56). As the compression increases, in the third and fourth cycles, the foams, especially the softer ones, seem to be most affected by the softening phenomena, furthermore it happens that the elongated cell pull itself in, leading to the observed incrementally negative Poisson's ratio. Alternatively, as highlighted by other authors [111], the observed auxetic behavior may be caused by the apices of the elongated cells rotating in response to the additional compressive strain. Approaching densification, the foam is totally compressed without the possibility to undergo to further transversal deformation, so the Poisson's ratio returns to zero.

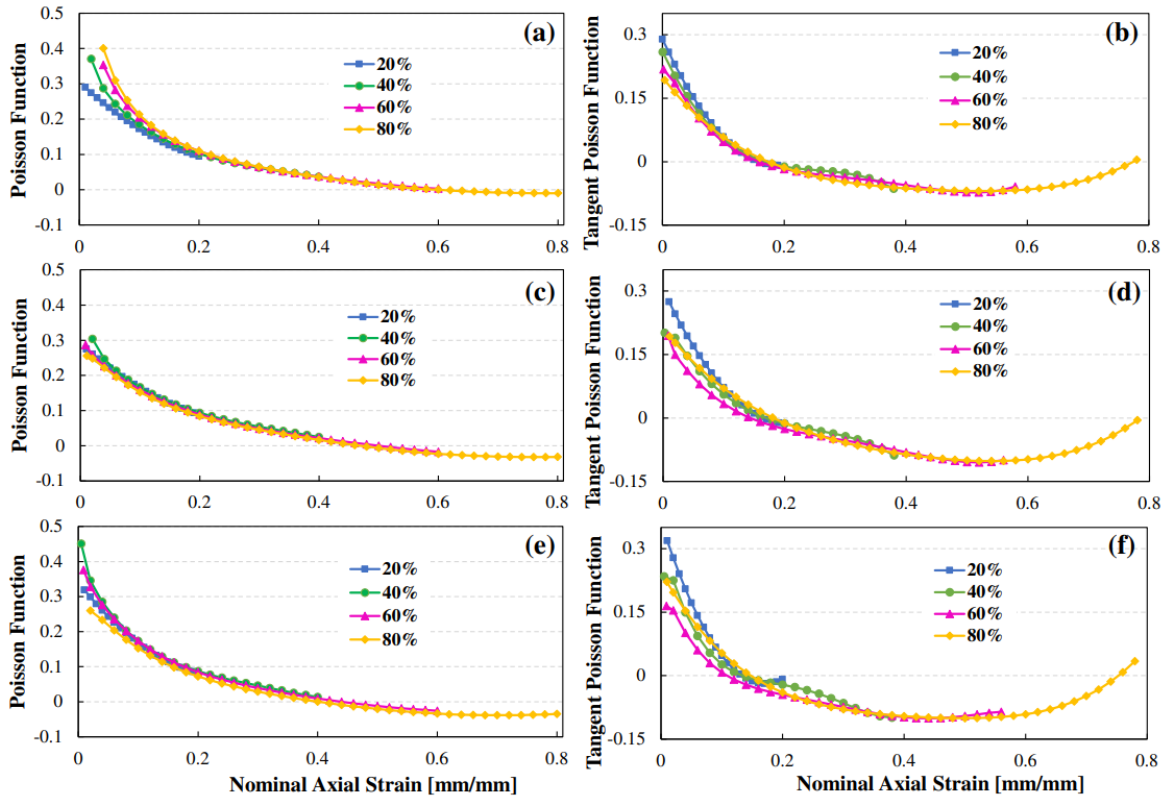

Figure 56 Evolution of the Poisson's function and of the tangent Poisson's function with nominal strain for Type A (a, b), Type B (c, d) and Type C (e, f) soft polyurethane foam for each cyclic compression step [16].

Also, the influence of the Poisson's ratio on the foam's compression behavior has been investigated from a numerical point of view. Since foams have a maximum transverse deformation of 2%, it is acceptable to consider a Poisson's ratio $\nu = 0$, as also suggested by literature [62,66] and by the *Mechanical behavior of elastomeric foams* section of Abaqus CAE guide [59], in case of large compression. Therefore, the *hyperfoam* material behavior is obtained considering a strain energy potential order N = 2 given the extremely non-linear trend of the compression curves. The material

is modelled considering two cases: by setting ν = 0 and providing the lateral nominal strain data point by point. In the latter case the software, through an algorithm, calculates two Poisson's ratio values, ν, according to the order N of the strain energy potential (§ 4.3). The *hyperfoam* material constants are summarized in Table 15. It is interesting to note how the first part of the curve is approximated by very high values of ν, close to 0.5, typical of an incompressible material, while the second part of the curve is characterized by completely different values which are, moreover, negative. In other words, the two found values, ν_1 and ν_2, show that foams at high compression levels, behave in the opposite way compared to the very first loading stages. For type A foam, the numerical output ν_1 = -0.1045 is quite different both from the more negative value found through the Poisson's function, ν_{sec}= -0.0101 and through the tangent Poisson's function ν_{tg}= -0.0693. While the numerical values of ν_1 identified for type B and type C are close to the most negative point identified by the Poisson function, ν_{sec} = -0.0322 and ν_{sec}= -0.3855 for type B and type C respectively. While the values identified by the tangent Poisson function are even more negative being equal to ν_{tg} = -0.1019 and ν_{tg} = -0.1006 for type B and type C.

Table 15 Finite element model constants obtained using compressive stress-strain curves until 80% of strain considering or not the lateral strain data for N=2.

		μ_1 [MPa]	μ_2 [MPa]	α_1	α_2	ν_1	ν_2
Type A	**ν = 0**	16.8665e-02	5.8777e-04	25.0000	-3.1196	0.0000	0.0000
	ν	8.6320e-02	4.1200e-03	25.0000	-1.2971	-0.1045	0.4932
Type B	**ν = 0**	5.5826e-02	1.1664e-03	25.0000	-2.1764	0.0000	0.0000
	ν	3.6560e-02	1.6042e-03	25.0000	-1.9501	-0.0289	0.4939
Type C	**ν = 0**	2.9965e-02	2.5872e-04	25.0000	-2.3389	0.0000	0.0000
	ν	1.9397e-02	6.4957e-04	23.9340	-1.5882	-0.0444	0.4874

The experimental results in form of displacement chromatic maps are reported together with the numerical results obtained through Abaqus CAE in Figure 57 and Figure 58. To simulate as much as possible what happens in the real experiment, the square 2D cubic sample was constrained at the upper end preventing the displacements along Y while at the lower end of the specimen a displacement up to 80% compression was imposed. Looking at the four steps reported in Figure 57 for the displacement along the load direction (Y), it is clear that the numerical model reproduces accurately what happen during the experiment. It should be clarified that the maps derived from the numerical model in the bottom row of Figure 57 and Figure 58 are obtained by including in the model the nominal lateral strain data, as required in the material section definition of Abaqus 6.13-1. Due to the progressive cells' collapse, mostly in correspondence of the movable plate and progressively smaller getting closer to the fixed plate, horizontal bands, clearly visible in Figure 57, are formed for

displacement along the load direction (Y). These bands have uniform color along the horizontal direction, appearing on the specimen in purple for greater displacements, while gradually fades in bands of the same color along the horizontal direction and becomes red at last, which corresponds to lower displacement according to the displacement color scale. These kind of deformations bands were also found in simple compression by Sadowski et al. [118] and by Linoul et al. [42] for closed-cell rigid PU foams. Considering the chromatic maps obtained for the direction transverse to the load, X, it can be seen that the numerical simulation (bottom row in Figure 58) well replicates what happens during the real test (top row in Figure 58). Indeed, concerning the experimental results, for 20% and 40% step (Figure 58a and b) the foam expands in both right and left direction while in the central area the material seems to have zero deformation. As compression progresses, 60% (Figure 58c) and 80% (Figure 58d), the trend of the transversal deformation of the specimen is reversed, as it can be seen from the reported displacements maps. The foam in the two final load steps is contracting and the shades of red at the 80% step indicate that the cells in the central area of the specimen are collapsing. In the numerical model, this behavior is captured at the 80% of strain (Figure 58h) but the localized effect that occurs in the experimental results displayed by DIC is missed.

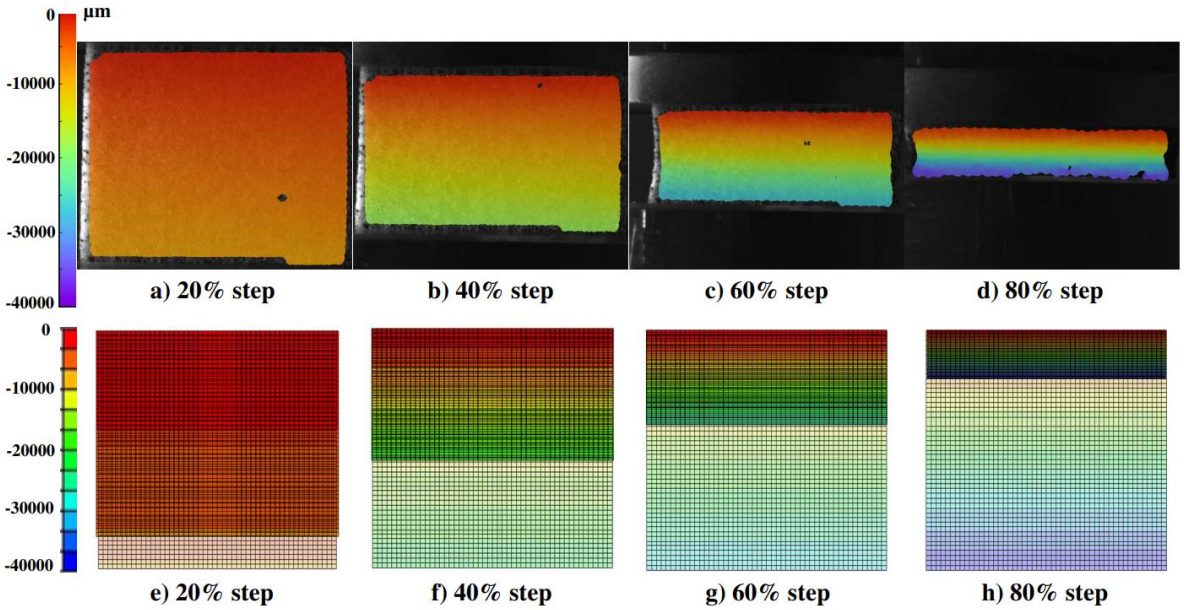

Figure 57 Experimental compression load steps of deformation and chromatic maps (expressed in µm) obtained by DIC for type B foam along the Y load direction (top row) and corresponding results obtained by numerical simulations (bottom row) [16].

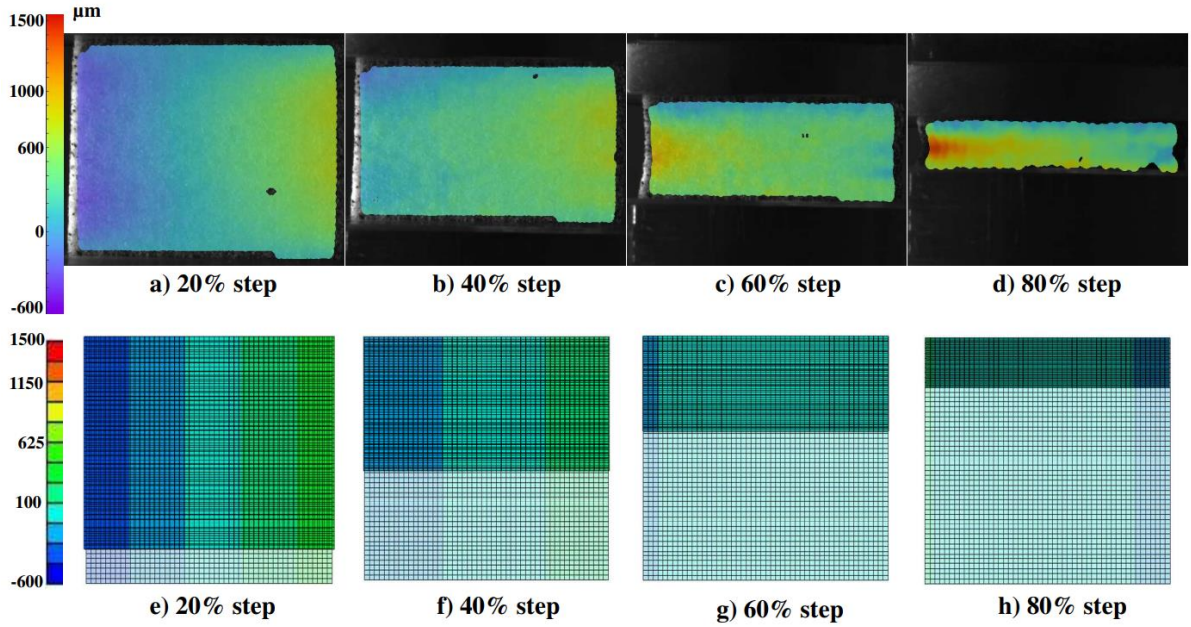

Figure 58 Experimental compression load steps of deformation and chromatic maps (expressed in µm) obtained by DIC for type B foam along the X transverse direction (top row) and corresponding results obtained by numerical simulations (bottom row)[16].

The behavior reported so far is also expressed by the stress-strain curves and by the lateral versus axial strain curves reported respectively in the *top row* and in the *bottom row* of Figure 59 for type A (a, d), type B (b, e) and type C (c, f) foams. For simplicity of representation, it was preferred to show only the compression up to 80% of strain. For the stress-strain curves, since the section variation is not very pronounced, it was preferred to compare them with the engineering curves. As far it concerns with the strains, since large deformations occur, a comparison considering both the engineering and the true data was performed for both the experimental and numerical curves. The stress-strain curves in Figure 59 show three typical regions that can be distinguished in cellular materials: a linear elastic branch followed by a stress plateau characterized by a line roughly parallel to the horizontal strain axis; finally, an ascending branch in which the stress steeply rises (densification) [26,27]. The stress-strain curves in the top row of Figure 59 show that the hyperfoam model reproduces very well the experimental curve in both cases $\nu = 0$ and considering the nominal lateral strain data point by point, the differences, although minimal, are noticeable in the stress peaks in the last load phase. More in detail, for type A, at 80% strain, a stress of 314.0 kPa is experimentally reached and errors of 4.1% and of 13.1% are recorded respectively for the curve obtained for $\nu = 0$ and for the one obtained considering the lateral nominal strain. The experimental test on type B foam gives a stress peak of 178.1 kPa at 80% of strain, replicated with a 10.5% of error by the data with $\nu = 0$ and with a 9.4% of error by the data including the lateral nominal strain. For type C an experimental stress peak of

53.8 kPa is reached at 80% of strain, with errors of 7.2% and of 2.9% respectively for ν = 0 and including the lateral nominal strain data.

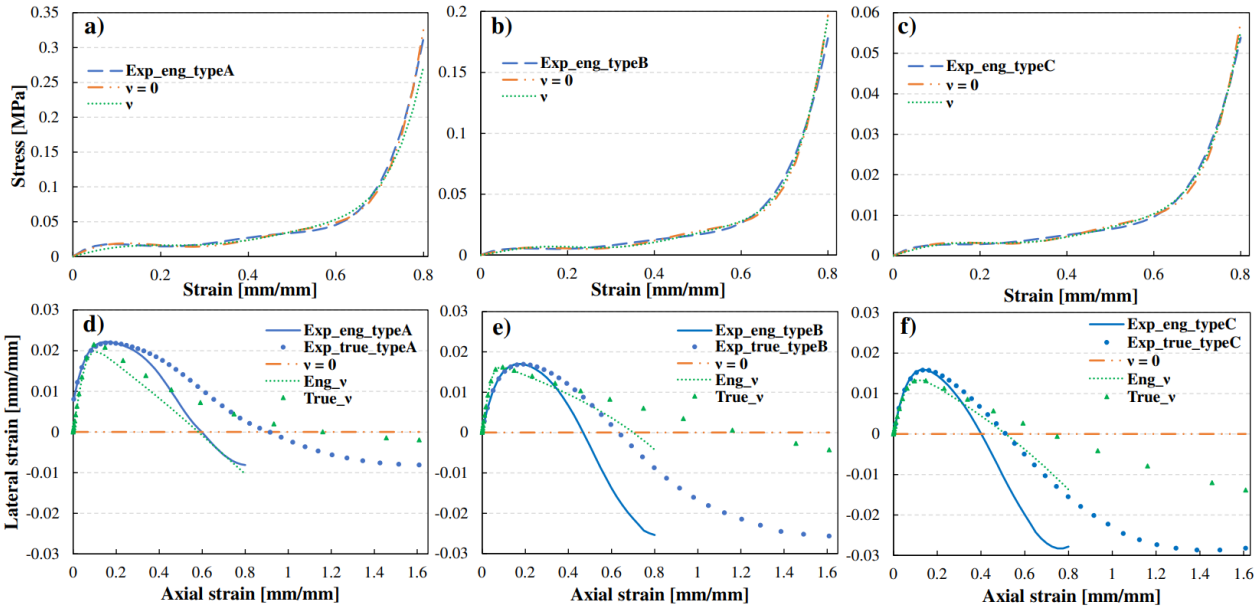

Figure 59 (Top row) Comparison of the experimental stress-strain curves obtained in cyclic compression at 80% of strain with those obtained by numerical simulations considering zero and non-zero Poisson's ratio for Type A (a), Type B (b) and Type C (c) soft polyurethane foam. (Bottom row) Comparison of the experimental lateral versus axial nominal compressive strain curves with those obtained by numerical simulations considering zero and non-zero Poisson's ratio for Type A (d), Type B (e) and Type C (f) soft polyurethane foam [16].

Observing the images of the lateral versus axial strain (bottom row in Figure 59) it can be noted that the numerical curves reproduce the trend inversion seen for the experimental curves. The only difference is that the experimental curves grow and then decrease with the same slope after the transition point, while the numerical curves show a different slope between the two sections. For both engineering and true formulation of type A the curves overlap quite well, while for type B and type C, after 40% strain, the experimental and numerical curves are quite different while the numerical model seems not to reach the same values of X-strain observed in the experimental test. As far it concerns with the results obtained from the numerical simulation it is interesting the comparison with those obtained by Widdle et al. [113]. These authors found that by incorporating the lateral stretch of the material into the uniaxial compression model the quality of fit degraded. This does not happen in the numerical model developed by Ogden [67] and implemented by Abaqus [59], in fact the numerical stress-strain curves in the *top row* of Figure 59 well reproduce the experimental curve and for the type B and the type C foam the stress peak obtained including the lateral nominal strain data is affected by a minor error respect to the one obtained with ν = 0.

The observed results are corroborated by the findings of Koumlis and Lamberson [48] who reported the same trend of the lateral versus axial strain, secant and tangent Poisson's function curves for a hard polyurethane foam used in a helmet shell. They found an auxetic behavior of the foam beyond 20% of nominal axial strain and that the Poisson's ratio is a function of the structure of the foam, independent of the loading rate. Similar results for the Poisson function were also reported by Pierron for a standard low-density polyurethane foam (30 g/dm^3) used to manufacture auxetic specimen [99]. Brincat et al. [111] tested until 75% of compression standard (untreated) polyurethane foam finding Poisson's ratio value ranged between 0 and -0.08 and the presence of the transition point between the 20 % and the 30% of axial compression, consistent with those found in this study.

4.8. Conclusions

4.8.1. Full-field experimental results

This section covers the analysis and evaluation of the mechanical characteristic of materials intended to be used in the design of human safety devices. For this purpose three soft open-cell polyurethane foams, with densities of 85, 65 and 45 kg/m^3 were tested. In order to satisfy also flame resistance requirements, a particular type of foam was chosen, containing expanded graphite particles dispersed in the material in a random way. This presence enhances the grayscale contrast compared to foams for which only the presence of voids in the material is exploited and allows to apply full-field DIC technique, directly exploiting the natural pattern of the specimen surface. Tensile, shear and cyclic compression tests were carried out to determine the characteristics of the materials and to compare their response to density variations. Despite unpainted specimens and large deformations, up to 90% in traction and shear for the least dense specimen and up to 80% in compression for all types of foam, full-field 2D-DIC successfully determined the full range of deformation experienced by the foams. Displacements and strains maps were obtained, stress-strain curves were plotted for each foam densities and the elastic modules were computed until 5% of strain following the linear elastic theory. Cyclic compression behaviour was deeply analysed also providing comments on the local behaviour of the material, because these foams are designed to absorb energy mainly in compression mode, for this reason, in addition to the displacement field, also the deformation gradient along the main directions was analysed proving that the deformation field is inhomogeneous and the deformation gradient is not constant across the whole field at given load step. Overall, considering all tests, it can be assessed that softer and less dense foams, can withstand deformations more than the higher density ones. As far as the energy absorption characteristics are concerned, the higher density foams dissipate more energy, as observed by the wider hysteresis cycles.

4.8.2. Shear test: a critical comparison among experimental approaches

For the analysis of the shear behavior of foams, the results obtained from the ASTM configuration with a 25 mm specimen were taken as reference which, as demonstrated by the analyses conducted with Digital Image Correlation (DIC), showed to be the least affected by parasitic effects. The results indicate that when using specimens with different thicknesses (25 mm and 50 mm), even though the load alignment conditions are not met, for this type of material, the results are very similar to those of the ASTM configuration with a 25 mm specimen. The BST configuration also provides good results, although it is much more time-consuming, parasitic effects are more pronounced and it is more complicated to achieve load alignment during the test setup. As for the Iosipescu test, it is not recommended to use notched specimens for this type of very soft material as they lead to an overestimated elastic modulus. DIC allows measurements to be taken up to large deformations; specifically, measurements taken with two points and with virtual extensometers at ±45° are comparable up to 30% deformation for ASTM and BS block shear tests, while they remain always comparable for the Iosipescu setup. Displacement and strain maps enable a qualitative investigation of undesired secondary effects. The best results are obtained for the ASTM C 273 setup with a 25 mm thick specimen and for the Iosipescu setup with an unnotched specimen. This implies that by obtaining shear characteristics through the Iosipescu setup with an unnotched specimen, there is a significant material savings and test repeatability is enhanced. In the latter case, a specimen of 20 x 26 x 13 mm is used, as opposed to a specimen of 200 x 70 x 25 mm.

4.8.3. Evaluation of the auxeticity of ordinary soft PU foam and numerical results

In this section the Poisson's ratio of materials intended to be used in the design of human safety devices was explored in tension and cyclic compression, both from an experimental and a numerical point of view under large deformations. Specifically, the Poisson's function and the tangent Poisson's function were used to characterize the material under tension and cyclic compression. It worth noting that, whereas the Poisson's function reaches an almost constant value after 10% of axial strain, the tangent Poisson's function keeps increasing up to 15-30% followed by a decreasing stage. The tensile behavior was also explored by FEM analysis considering three different conditions: $\nu = 0$, $\nu = \text{const}$ (the maximum value of the tangent Poisson's function) and considering the lateral deformation data of the specimen point by point. The two last conditions represent a novel approach for the description of the mechanical behavior of soft polyurethane foams. Results show that the experimental engineering stress-strain curves were faithfully reproduced considering a zero Poisson ratio while the true stress-strain curves and the true lateral versus axial strain curves were well reproduced considering $\nu = \text{const}$. In general, the numerical curves obtained including in the model the lateral strain data well reproduced the experimental true stress-strain curves, except for the type B foam

where a deviation in the true lateral versus axial strain curve is observed. Differently from what observed in tension, the foams behave auxetically in cyclic compression. This is verified for all the tested densities. The lateral strain behavior under cyclic compression load turns out to be characterized by a sequence of increasing/decreasing slopes. This result agrees with that found by Brincat et al. [111] in simple compression. Trend inversion occurs close to 20% of axial and 2% of transverse strain and reoccurs approximately at the same strain values with increasing load cycles. The tangent Poisson's function formulation shows negative value of the Poisson's ratio around 20% of global axial strain. This result is consistent with those found by plotting the transverse versus axial strain curves. Therefore, the tangent Poisson's function better highlights the auxetic behavior of the foams with to the Poisson's function formulation, which assumes negative values only at large strain. FEM analysis shows good results also in compression, with stress peaks closer to the experimental ones when $\nu = 0$ and when the nominal lateral strain data (ν) are included. The numerical model faithfully reproduces what occurs along the load direction. In transversal direction, on the other hand, DIC can capture phenomena like local cells collapse that are lost in the numerical simulations.

5. Numerical Modeling of a Crash Test

In this section, the modeling of impact tests Test 1 and Test 2, as described in §3.4, is discussed. This chapter is the result of an internship carried out in collaboration with Siemens engineers, in particular the Business Development Manager and the Lead Research, who provided the Madymo software license and support for the numerical modeling technical issues.

5.1. Preface

The BK160 Gabriél aircraft, based on its configuration (2 seats), weight (850 kg), and performance ($V_{stall} \leq 45$ knots), complies with the Special Condition requirements, resulting from the collaboration between Blackshape and EASA in the aircraft certification process (§2.3.3). The simulation of dynamic impact conditions specified in CS 23.562 Emergency Landing Dynamic Conditions section is aimed at a more in-depth study in the event of an upgrade of the performance (in terms of weight and stall speed) of the current aircraft configuration. In this way, from a design perspective, the limits of the current configuration are being examined to identify any issues that need to be addressed when transitioning to a more advanced configuration.

5.2. Madymo and the Multi-body Systems

Simcenter Madymo (MAthematical DYnamic MOdel) is a computer program that simulates the dynamic behavior of physical systems emphasizing the analysis of vehicle collisions and assessing injuries sustained by passengers. Although originally developed for studying occupant behavior during car crashes, Madymo is sufficiently flexible to analyze collisions involving other means of transport such as trains, airplanes, motorcycles and bicycles. It also allows assessments to be made of the suitability of various restraint systems, including seat belts and airbags. Madymo combines in one simulation program the capabilities offered by multi-body (for the simulation of the gross motion of systems of bodies connected by kinematical joints) and finite element techniques (for the simulation of structural behavior), Figure 60. A model can be created with only finite element models, or only multi-bodies, or both [119].

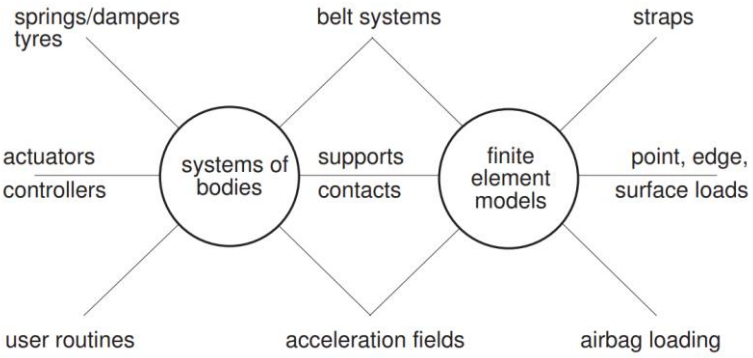

Figure 60 Madymo structure [119].

5.2.1. Finite Element Method (FEM) vs. Multi-Body Dynamics (MBD)

FEM and MBD are two different approaches in solving a problem. FEM approach is used usually when the deformation is to be calculated, while for the rigid body displacement component, multi-body dynamics approach should be followed [120].

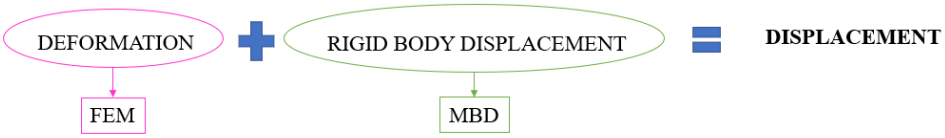

Figure 61 Concept scheme of combination of Finite Element Method and Multi-Body Dynamics.

To better communicate the difference, consider a falling block in Figure 62. When using FEA, the body is assumed to be deformable, and does exhibit deformation or a change in shape during the simulation (Figure 62a and b).When using MBD, the body is assumed to be rigid, and does not change shape at all during the simulation (Figure 62c and d). At a very general sense, MBD is used to determine the loads of moving/dynamic bodies, and FEA is used to determine the stresses and strains of static or dynamic bodies. The following table (Table 16) brings out the differences between the two approaches at different stages of a simulation. Depending on the desired output, one can choose either method, considering that the Finite Element Method (FEM) will require comparatively more time to solve the problem when there are more nodes involved, resulting in a higher degree of freedom. Another approach is to combine Multibody Dynamics (MBD) and FEM. This represents the optimal approach for solving systems that consist of multiple subsystems, which is often the case in reality. In the initial step, the MBD approach can be employed to simulate the motion of the body and determine parameters such as velocity, acceleration, and external loads. These loads can then serve as input for the Finite Element (FE) simulation to calculate the deformation of the body. It is widely recognized that any model is a part of a larger ecosystem. FEM is commonly used at the *Part* stage, while MBD is employed at the *Assembly* and *Product* stages. The MBD approach can be used to simulate body motion and extract parameters such as velocity, acceleration, and external loads.

These loads can be subsequently utilized as input for the FE simulation to compute body deformation. Technically, the combination of MBD and FEM is referred to as *reduction*, and *Component Mode Synthesis* (CMS) is one of the most commonly used methods for achieving this Figure 63 [121].

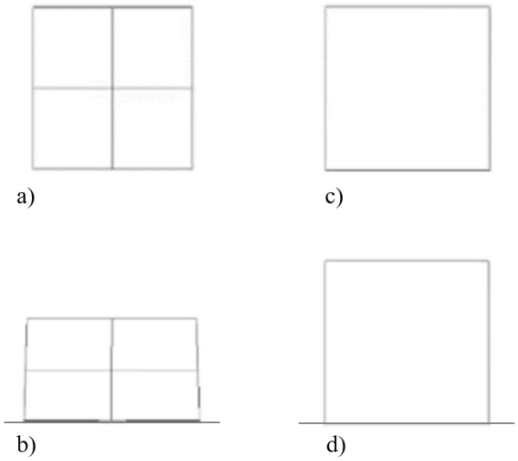

Figure 62 Falling block in a Fem analysis before the simulation (a) and during the contact with the ground (b), falling block in a MBD analysis before the simulation (c) and during the contact with the ground (d)[120].

Table 16 Difference between FEM and MBD at different stages of a simulation [120].

Parameter	**Finite Element Method**	**Multibody dynamics**
Before the simulation – Assumption	Body – Deformable	Rigid body
During the simulation – Shape	Shape changes	No shape change
After the simulation – Output variables (Common)	Stress, Strain, Strain rate	Acceleration, Velocity, Loads on moving bodies

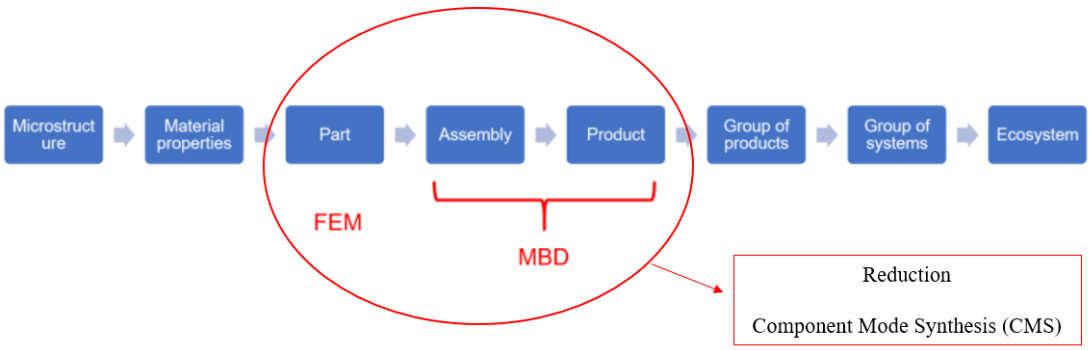

Figure 63 Breaking down an ecosystem [121].

5.3. Simcenter Madymo vs. Abaqus

In the numerical modeling part of the impact test, the cushion assumes significant importance because, as of now, given the configuration of the aircraft seat being examined, it is the only component designed to absorb the vertical energy generated in an impact. From the results of the numerical model described in § 4, it is evident that the Hyperfoam model implemented in Abaqus accurately reproduces the behavior of the analyzed polyurethane foams. At this point, it is interesting to determine whether the material model available in Madymo provides results comparable to those obtained in Abaqus. To this end, a drop ball test was simulated in order to compare the displacement and the forces generated during the contact between the ball and the foam.

5.3.1. Simcenter Madymo Material Foam Modeling

The behavior of solid foams can be described as highly non-linear and strain-rate dependent with high energy dissipation characteristics and hysteresis in cyclic loading. Low density combined with high energy dissipation capacity make foams attractive for energy absorbing functions in automotive and aerospace applications. However, the three-dimensional mechanical response of foam materials is quite difficult to capture in a mathematical model. The foam material model implemented in Madymo uses an experimental stress-strain curve rather than a material law. It is available for solid elements only. The model is based on the following two assumptions:

- there is no coupling between stresses and strains of different principal directions;
- strain rate effects can be characterized by a strain rate dependent scaling factor.

As a result, the stress-strain curve can be determined from uni-axial compression and tension tests for different loading rates. Mathematically, the stress-strain relationship has the following form:

$$\sigma = \xi(\dot{\bar{\varepsilon}})\sigma_r \tag{37}$$

where ξ is a scaling factor that depends on the effective strain rate, and σ_r is a user specified reference stress curve, $\dot{\bar{\varepsilon}}$ is the effective strain rate. This curve represents the quasi-static uni-axial behaviour of foam under both compression and tension. A piecewise linear interpolation is used. For this kind of material, the energy dissipation can be described by hysteresis.

Three Hysteresis models are available in Madymo, Hysteresis models 1 and 2 are generally used for foam materials and require the specification of the following parameters also reported in Figure 64:

- a loading curve $y_l(x)$;
- an unloading curve $y_u(x)$;

- a hysteresis slope *sl*;
- an elastic limit x_e.

The slope parameter *sl*, Δy/Δx in Figure 64, defines a linear function joining the loading and the unloading curve. The same slope *sl* is used for positive and negative values of the deformation *x* [119]. For further information about the topic consult the *Simcenter Madymo Theory Manual* [119].

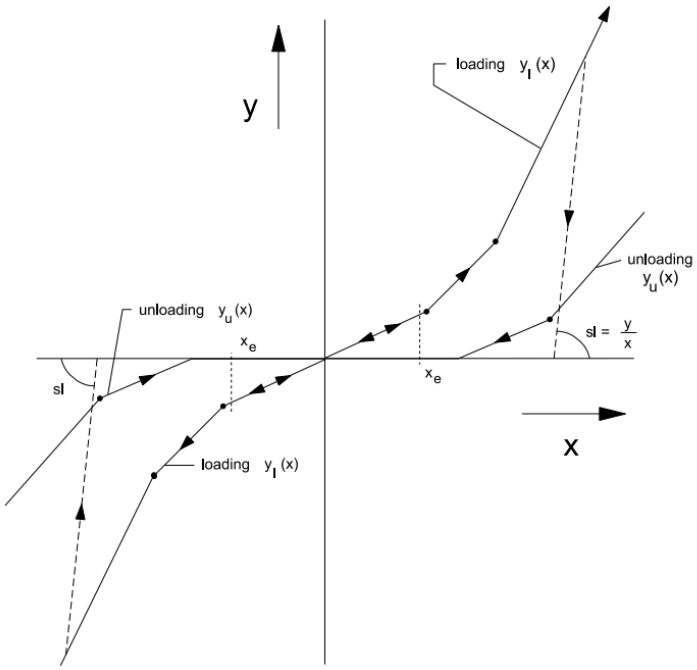

Figure 64 Parameters for description of hysteresis models 1 and 2 [119].

Two analytical laws are available for scaling up the user-defined stress-strain curve, the Cowper-Symonds and the Johnson-Cook formulations, reported respectively in eq. 38 and 39.

$$\xi(\dot{\varepsilon}_n) = 1 + \left(\frac{\dot{\varepsilon}_n}{C_1}\right)^{\frac{1}{C_2}} \tag{38}$$

$$\xi(\dot{\varepsilon}_n) = 1 + C_2 ln\left(\max\left(\frac{\dot{\varepsilon}_n}{C_1}\right), 1\right) \tag{39}$$

where C_1 and C_2 are user specified positive constants. Besides these, it is also possible to define a strain rate dependency function ξ as a user specified function. Both this user specified function and these empirical laws are based on nominal strain rates, $\dot{\varepsilon}_n$, so a transformation of logarithmic strain rates to nominal strain rates must be carried out. Taking the derivative of the effective strain with

respect to time and using the relationship between nominal and logarithmic strains, the nominal strain rate is obtained as:

$$\dot{\varepsilon}_n = \exp(s\varepsilon)\,\varepsilon^{-1}\boldsymbol{tr}\left(\underline{\varepsilon}\cdot\underline{\dot{\varepsilon}}^T\right);\quad s = sign\left[\min\left(\underline{\varepsilon}\right) + max\left(\underline{\varepsilon}\right)\right] \tag{39}$$

The nominal strain rate is adjusted depending on the sign of the largest absolute value of the principal strains. As a result, the stresses are scaled up much more for loading than for unloading.
Material damping can be taken into account by a similar model as used for isotropic and orthotropic materials, in which the damping is represented by a linear dependency on the strain rate:

$$\sigma = \tilde{\sigma} + \gamma\dot{\varepsilon} \tag{40}$$

where $\tilde{\sigma}$ is the stress tensor derived from the specified stress-strain curve including strain-rate dependency effects, $\dot{\varepsilon}$. γ is the damping coefficient, which is defined as

$$\gamma = Kd(\mu + (1-\mu)dt_e) \tag{41}$$

where K, d and dt_e denote, respectively, the maximum slope of the defined stress-strain curve, a damping constant and the critical element time-step according to the undamped stability criterion. The parameter μ can have two discrete values:

- $\mu = 0 \rightarrow \gamma = Kd\Delta t_e$, namely the damping depends on the element time step and as a result on element size; small elements show less damping than large elements.
- $\mu = 1 \rightarrow \gamma = Kd$, namely the damping is identical for all elements irrespective of size.

Regarding the data to be implemented in the model, it is important to include the complete compressive and tensile stiffness data in the curves, otherwise Madymo will extrapolate the data, which may not provide an accurate representation of the material behavior. Further details can be found in the *Simcenter Madymo Theory Manual* [119].

5.3.2. Drop Ball Test Modelling

A simple impact test was modeled in both Abaqus and Simcenter Madymo to compare the displacements and forces generated as a result of the impact of a sphere against the cushion. For this purpose, for both tests the following conditions were considered:

- a sphere with a radius R = 50 mm and a mass of m = 2 kg;
- a foam cushion of 400 mm width, 400 mm length and 100 mm height;

- a drop height of 1000 mm measured from the center of the sphere.

Figure 65a and b show respectively the Madymo model in the Y-Z plane and the ISO view. As evident from the images, the modeling is hybrid and includes two multi-body entities, namely the sphere and the support plane, and one Finite Element Method (FEM) modeled body, which is the cushion. The cushion's mesh was generated in Abaqus and imported into Madymo. In Madymo, it is important to define contact surfaces. To achieve this, the upper and lower surfaces of the cushion were modeled using a thin shell composed of elements connected with 4 nodes (PROPERTY.SHELL4), while the interior part of the cushion defined by the MATERIAL.FOAM property was modeled with solid elements connected with 8 nodes (PROPERTY.SOLID8). Loading and unloading functions of type A foam were defined as Cauchy (or true) stress versus Logarithmic (or true) strain, applicable for both small and large strains and Hysteresis mode 2 was used.
Figure 66a and b show respectively the Abaqus model in the X-Y plane and the ISO view. The sphere was modeled as a rigid body using R3D4 mesh element while the cushion was modeled through the 8-node brick C3D8R mesh element. A total of 1024 nodes were used to model the cushion, which are the same as the nodes in the cushion model in Madymo. As was previously described in §4.3 the foam was modeled using the Hyperfoam material model including the Mullins effect and the data related to the Poisson's ratio. As for the material model, the main differences between Abaqus and Madymo lie in the use of two different sets of data: tension and compression in Madymo, only compression with Mullins' effect in Abaqus and in the consideration of the Poisson's ratio. Indeed, as was already clarified in §5.3.1, in Madymo the Poisson's effect are neglected.

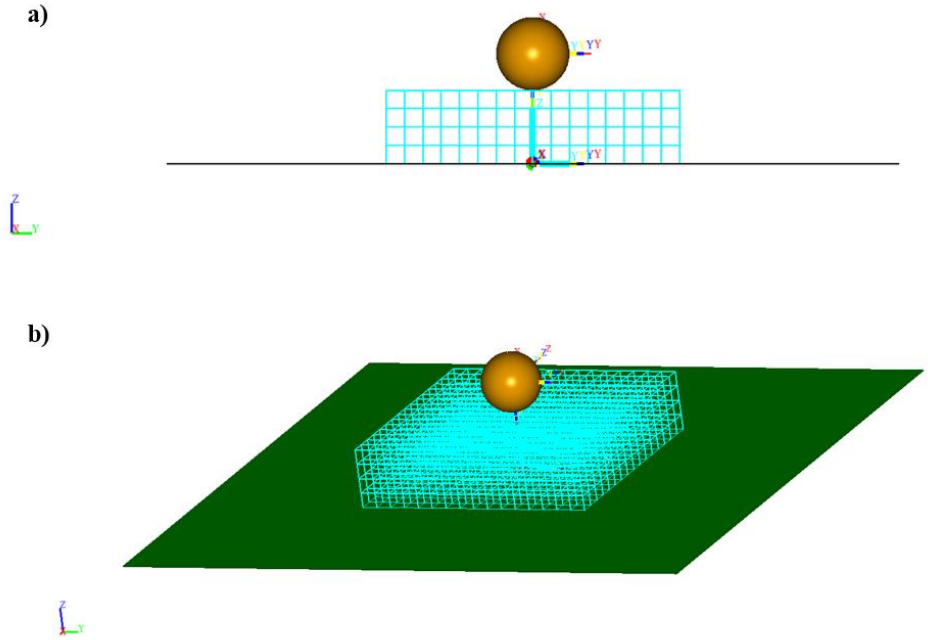

Figure 65 Drop Ball Test Madymo model a) scheme in the Y-Z plane, b) isometric view.

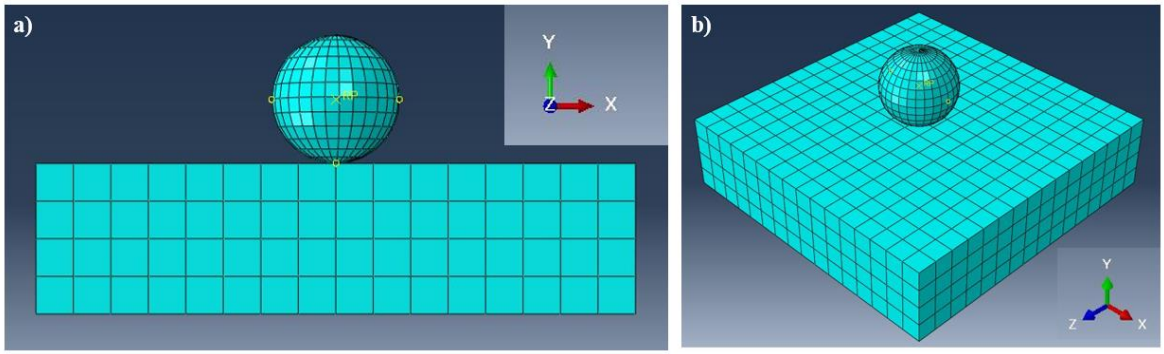

Figure 66 Drop Ball Test Abaqus model a) scheme in the X-Y plane, b) isometric view.

The results at the moment of maximum sphere penetration into the cushion are shown in Figure 67. Specifically, in Figure 67a, the indentation in Madymo is depicted, while in Figure 67b, the cushion section with the deformed mesh due to the impact of the sphere is evident. In the Madymo model two points were considered: the green one at the bottom of the cushion in contact with the plate and the red one representing the maximum indentation point of the foam. Their distance was calculated to be 61.62 mm. Considering that the height of the foam is 100 mm, it can be determined that the penetration at that point is 38.38 mm. Observing Figure 67c, obtained in Abaqus, it is immediately clear that the extent of sphere penetration is comparable to that obtained in Madymo, as also indicated by the color contour map and the node displacements in Figure 67d. The graph in Figure 66 clearly shows that the magnitude of the displacement obtained in Madymo closely follows that obtained in

Abaqus, and the maximum displacement magnitude is the same. Minimal differences are noticeable in terms of the force generated by the sphere-cushion contact. The values obtained in Abaqus are slightly higher at the peak of the maximum displacement. Specifically, a maximum force of 760N is reached in Abaqus, while a maximum force of 658N is reached in Madymo. Overall, it can be said that Madymo accurately reproduces the behavior of foams defined with the Hyperfoam model, which has already been validated using experimental data.

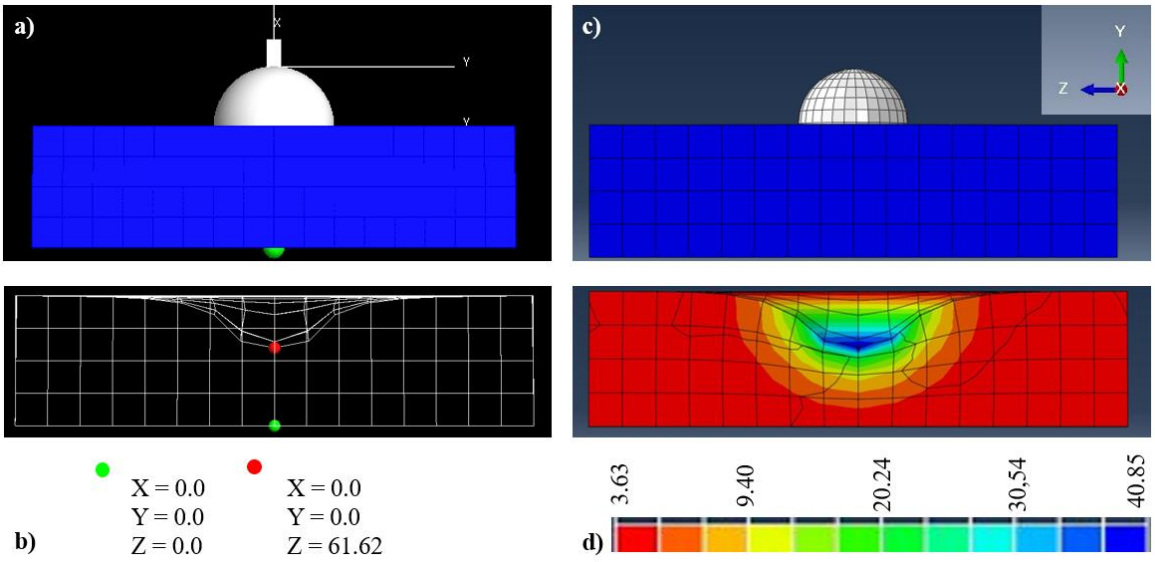

Figure 67 Drop Test results, a) Foam indentation by Madymo, b) section of indented foam with nodal deformation starting from the initial thickness of 100 mm, c) foam indentation by Abaqus, d) section of indented foam with nodal deformation. Measures are expressed in mm.

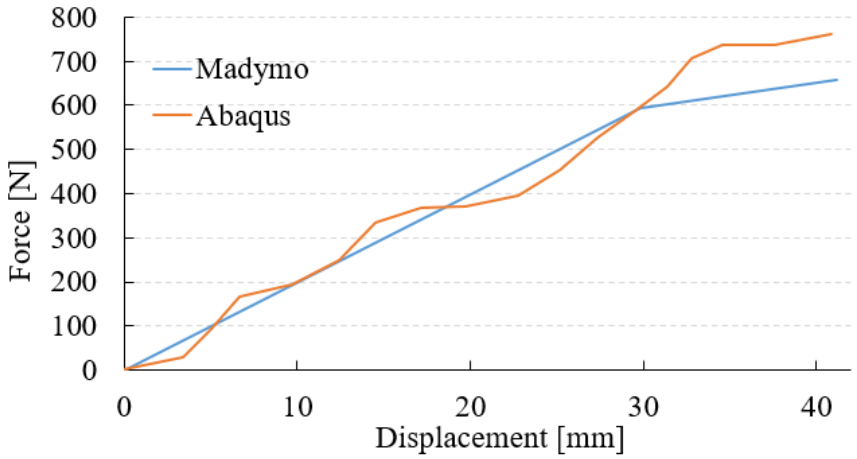

Figure 68 Drop Ball Test Abaqus vs. Madymo force vs. displacement result.

5.4. Safety Design of a Fully Integrated Seat in Fuselage structure

A Fully Integrated Seat in Fuselage (FISIF) structure refers to a concept in aircraft design where the passenger seats are an integral part of the aircraft's fuselage rather than being separate components that are installed into the cabin. This design approach is primarily associated with new and innovative aircraft concepts that aim to enhance passenger comfort, safety, and overall aircraft efficiency.

The aircraft efficiency is a key aspect in terms of weight savings; indeed, if traditional aircraft seats, which are separate components that need to be installed and secured within the cabin, adds weight to the aircraft, integrated seat reduce the weight of the cabin and contribute to fuel efficiency. Also, for small category airplanes, an integrated structure simplifies the complexity of the cabin layout, allowing for more efficient use of the available space. From a safety perspective, integrated seat may enhance safety in a crash scenario, since seats could be designed to absorb and distribute impact forces more effectively; but in some cases, the structure may be so rigid that it can transmit high forces to the occupants, which can result in serious injuries. The simulations presented below will be useful to understand any limitations and advantages of the current configuration in terms of safety. The following results offer a comprehensive insight into variations in injury parameters, depending on the diverse foam densities and thicknesses employed in the cushion. The cushion's efficacy is evaluated through a comparison of these results with those obtained when the virtual dummy is positioned on a rigid seat. Additionally, and of notable relevance, the thesis provides insight into excessive loads on the lumbar region, with 'excessive' defined in accordance with CS 23.562 regulations. Normally, in the certification process of aircraft seats, it is usual to see regular seats anchored on a sled, consisting of structural elements such as joints, seat frame structure, safety belt anchoring points, and non-structural elements such as cushions and restraint, as was showed in § 3.4. The peculiarity of the study presented in this thesis work is precisely given by the structural configuration of the seat, which is integrated into the fuselage structure. For this reason, as will be seen in the following paragraphs, the dynamic impact test simulations will concern the entire aircraft section and not exclusively the seat itself. This uniqueness distinguishes the present study from other works in the literature that focus on the traditional sled tests.

5.4.1. Bk 160 Gabriél sitting padding geometries and FEM modeling.

As previously mentioned, the examined seat is both rigid and integrated into the aircraft's structure, serving as a reinforcing element. Among the potential solutions outlined in §3.3.1, the most viable option is the utilization of seat padding. This padding is specifically designed to absorb the energy generated during an emergency landing. However, the options for custom-designed solutions aimed at absorbing the vertical energy component and maintaining lumbar load within mandated limits are considerably constrained when accounting for the available vertical space. The space between the

seat's bottom and the cockpit, which encloses the cabin, has to accommodate a pilot conforming to the anthropometric specifications outlined for a 95th percentile pilot [12]. These specifications describe the physical dimensions and measurements that represent the larger segment of the pilot population. They play a pivotal role in the design of aircraft cockpits and seats, ensuring their ability to comfortably accommodate a wide range of pilots. Typically, a 95th percentile pilot is larger and heavier than the average individual. For example, in the United States, a male pilot's height is approximately 183 centimeters, while a female pilot's height averages around 175 centimeters. Figure 69 shows a schematic of the Gabriél fully integrated seat structure including padding locations. Figure 70 and Figure 71 show the padding geometries with the actual measure respectively of the backrest and the seat cushion.

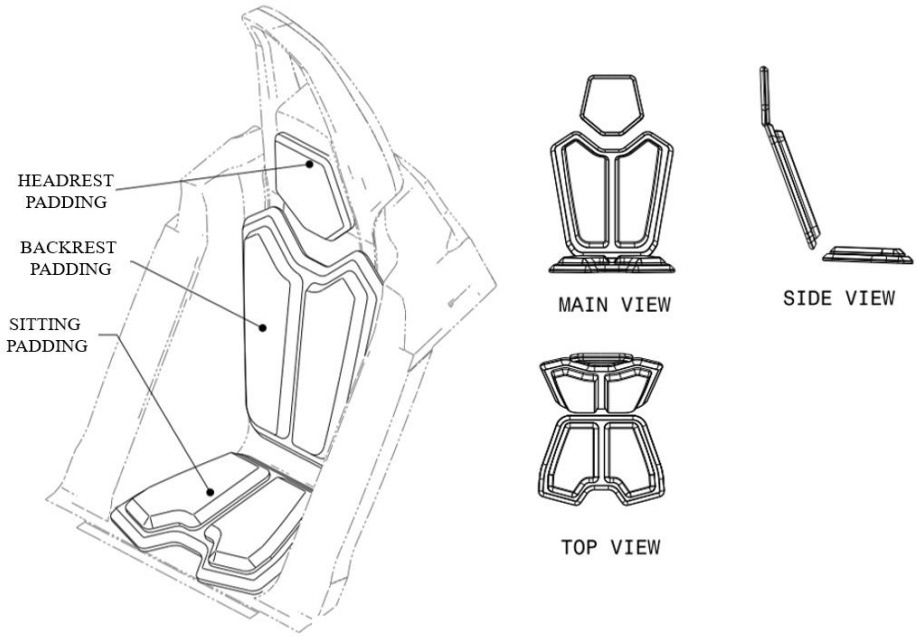

Figure 69 Bk 160 Gabriél Schematic of the fully integrated seat structure including padding locations.

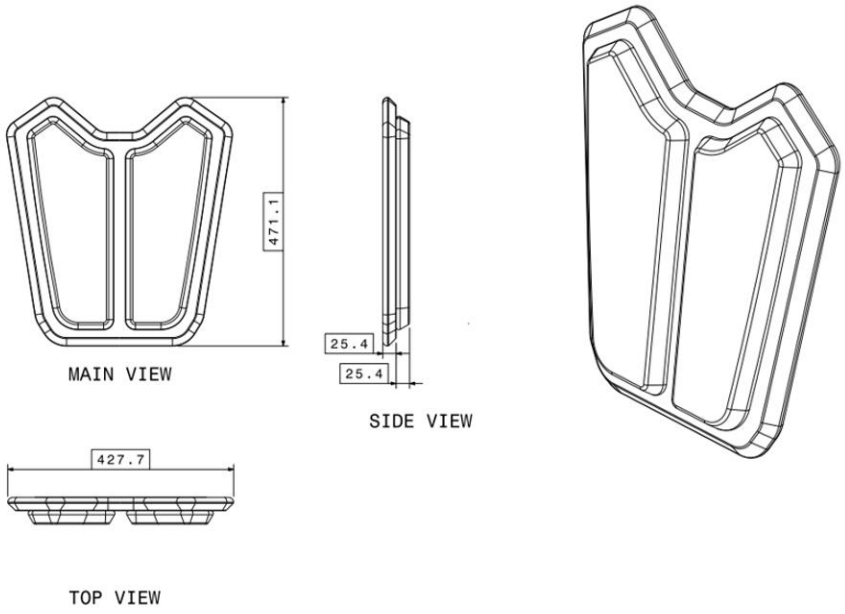

Figure 70 Bk 160 Gabriél backrest padding geometries. Measures are expressed in mm.

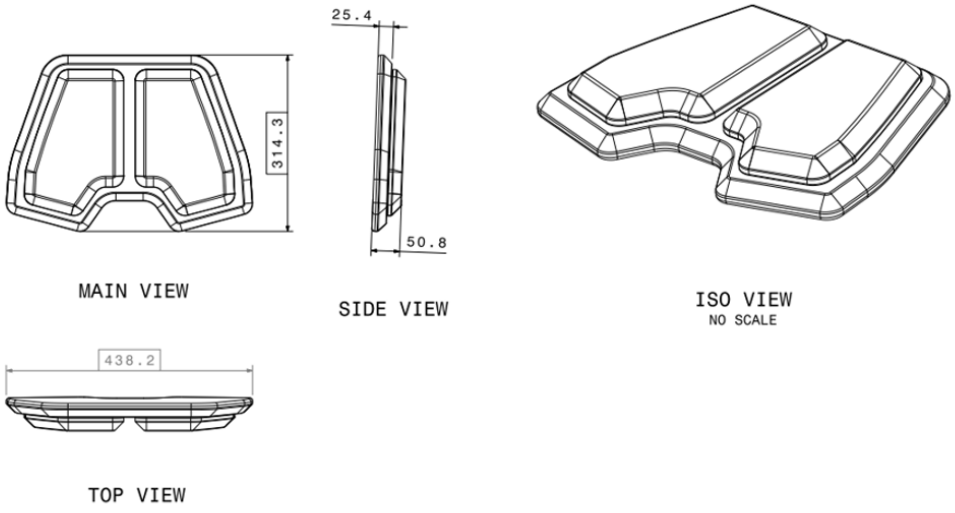

Figure 71 Bk 160 Gabriél sitting padding geometries. Measures are expressed in mm.

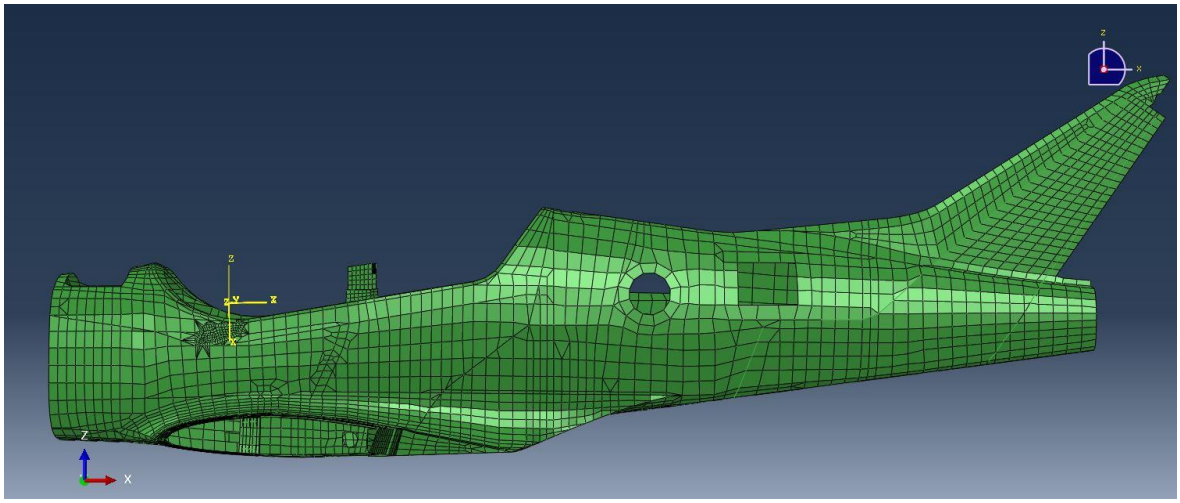

Figure 72 Nastran structural model of Bk 160.

The numerical structure representation of the Bk 160 in Figure 72 clearly shows the structural continuity of the entire fuselage body. The section in Figure 73 distinctly illustrates how the seat is connected to the sides of the cabin and to the wing spars, which are integral parts of the fuselage.
Upon closer examination of the seat in Figure 73, it becomes apparent that the mesh exclusively encompasses the structural components, excluding the cushions. In order to ensure precise alignment between the nodes of the cushions and those of the underlying structure, both the seat padding and backrest cushions were generated starting from the mesh located on the supporting surface of these padding elements. It is a well-established fact that numerical calculation software operates most effectively when nodes and connecting elements exhibit exact correspondence, thereby facilitating the accurate transmission of load and displacement data. Moving to Figure 74, the cushions in various configurations are presented. In Figure 74a, the cushion with its original design thickness of 50 mm is depicted (1495 node mesh). Figure 74b showcases the cushion at its maximum allowable thickness, 100 mm (2411 node mesh)., to conform to vertical space limitations Finally, in Figure 74c, the backrest is illustrated, which maintains a consistent thickness of 50 mm throughout (1989 node mesh).

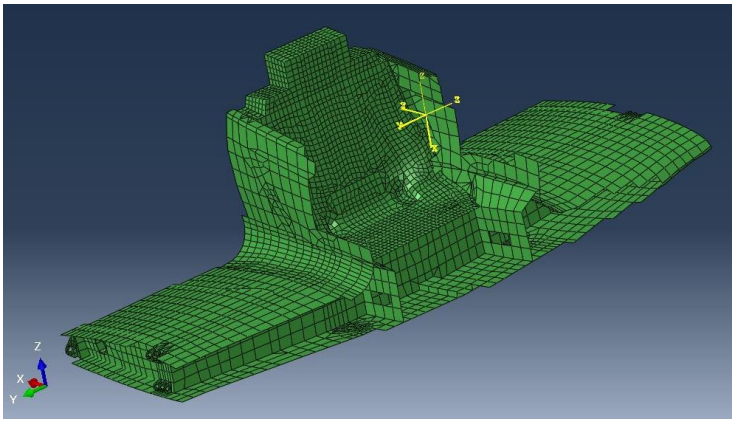

Figure 73 Nastran structural model of the fully composite integrated seat structure.

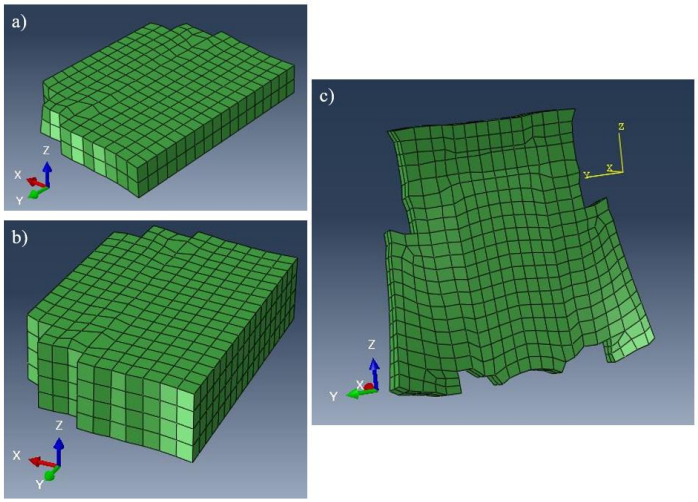

Figure 74 Mesh of the 50 mm seat cushion (a), 100 mm seat cushion (b) and of the backrest (c).

5.4.2. Simcenter Madymo structural model

In the marketplace, a variety of finite element modeling software programs are available, allowing for the transfer of models from one software to another. However, this interchange often results in the loss of valuable information. In this particular case, the structural model of the Bk 160 underwent initial analysis within Siemens' Simcenter platform before being imported into Madymo. This transition was facilitated by Siemens engineers who provided essential support throughout the modeling phase. Utilizing the Simcenter platform for structural analysis enabled the establishment of comprehensive global performance targets for strength and energy absorption, which in turn guided the structural design process. Employing nonlinear implicit structural analysis, the design was meticulously assessed against these performance targets, leading to the identification of critical load-bearing areas. Furthermore, the results of these simulations were systematically processed and automatically integrated as global stiffness characteristics into the corresponding MB structural

model of the safety system. This enhancement significantly bolstered the accuracy of the safety model, better equipping it to support certification activities. Since the results are confidential, in Figure 75, only images of the outputs related to material thickness properties and material properties by Simcenter are displayed.

After these steps, a Madymo input data file can be set up which specifies the configuration, the mass distribution and the general properties of the multibody systems (joint characteristics) and finite element structures. Simcenter Madymo XMADgic editor has an environment that allows for user-friendly visualization and manipulation of geometries. As evident from the images observed thus far, the aircraft's mesh is comprised solely of structural elements. To achieve a more faithful representation of the crash test, which includes the potential impact of the pilot against objects within the cabin, the multibody technique was employed to model the controls bulk located in front of the seat (brown items in Figure 76). Indeed, planes and ellipsoid can be used to model a body and represent its shape, these planes and ellipsoids are also used to model contact with other bodies or with finite elements. Each ellipsoid has associated kinematic properties, such as mass, stiffness, volume, inertial properties etc.[122]. During this modeling phase, FEM models of the backrest (green item in Figure 76) and the cushion (gray item in Figure 76) were imported into Madymo. These models, using proper joints, were strategically positioned on the rigid structural surfaces to ensure node alignment. Specific features like seat harness joint can be also modeled in Madymo (Figure 76). These joints were positioned considering the real configuration of the airplane and are used to simulate the behavior and interaction of seatbelts and harnesses with crash test dummies or occupants during crash simulations.

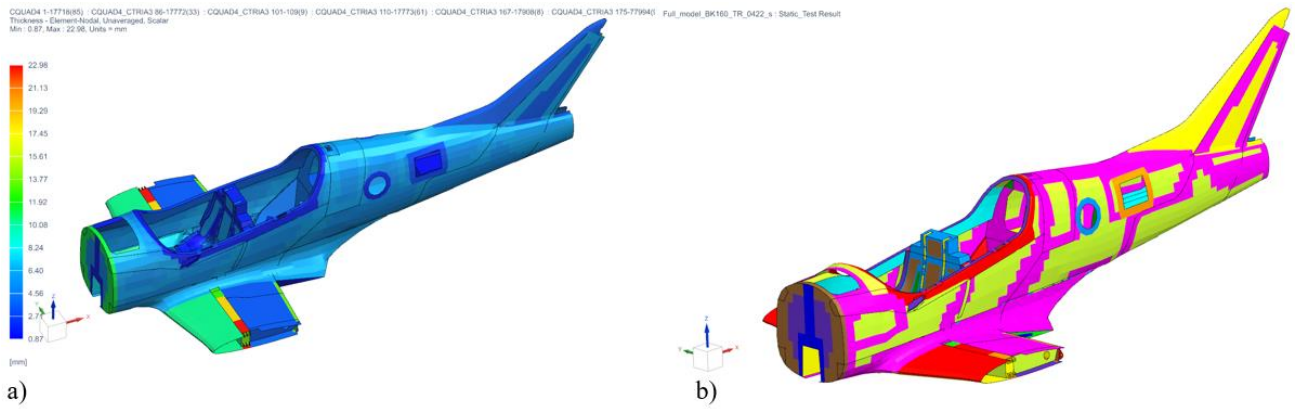

Figure 75 Bk 160 a) material thickness properties and b) material properties by Simcenter.

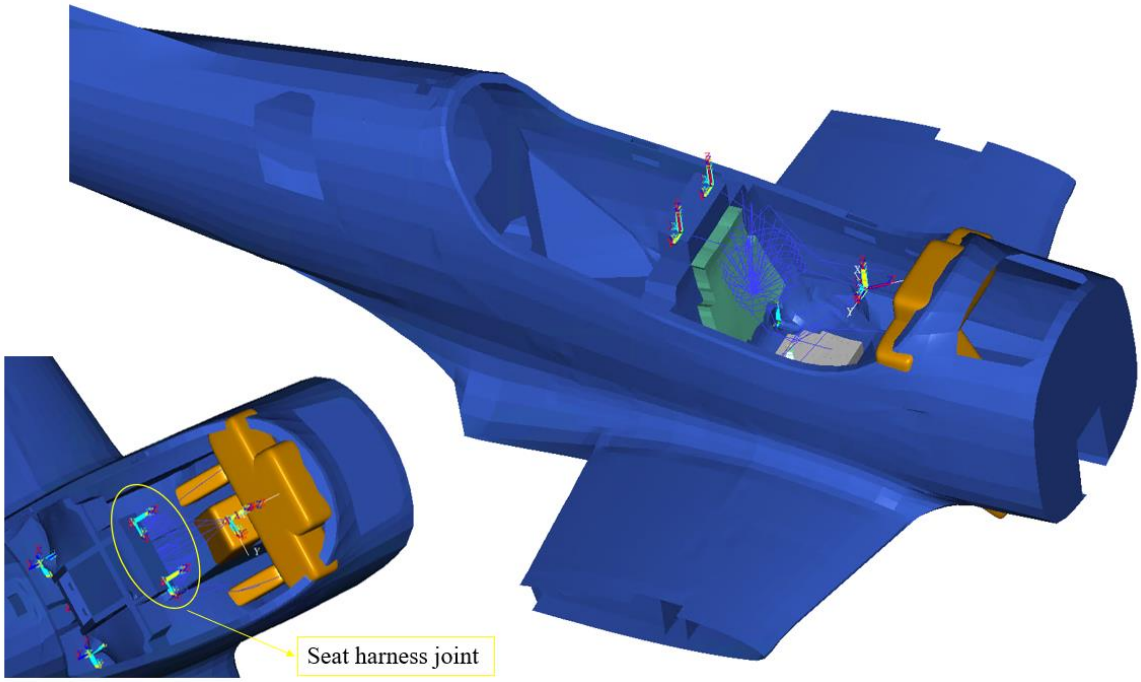

Figure 76 Simcenter Madymo structural model of BK 160 including the paddings, controls bulk and seat harness joint.

5.4.3. Dummy model and restraint system

A Hybrid III 50th Percentile Dummy, based on the human body, (new Siemens release 2022) is seated in the aircraft and restrained by shoulders and lap belts (Figure 77a and b). This dummy model accurately represents FAA-specific components ensuring that component masses and dimensions align precisely with the provided specifications. The new FAA-Dummy model is a multi-body model that offers significantly faster simulation run times compared to its previous versions. The major improvement of the Hybrid III 50th FAA over the Hybrid II dummy are the lumbar spine, that is capable of a more realistic response in severe vertical loading and the extended instrumentation, in particular in the thorax, neck, and leg regions. Additionally, compliance and contact properties of these components have been meticulously updated to meet the stringent hardware requirements necessary for individual component certification tests. Further details can be found in the *Simcenter Madymo Model Manual* [123]. The dummy interaction was set with the seat cushion, the seat belt system and the multibody items representing the controls bulk (Figure 78a and b). This is crucial for understanding injury mechanisms and improving occupant protection. Indeed, the dummy was used to calculate the injury parameters such as: HIC for the head resultant acceleration, the pelvis and the belts load. This dummy model is part of the Simcenter Madymo database, which has a wide library of different models, from infants to adults, based on the specific component (i.e., infant car seat) that has to be tested. Madymo allows engineers and researchers to simulate how restraint systems interact

with human dummies or occupants during a crash event. In this specific case only the seatbelts system was modeled, but also airbags, and other safety components are available. Respecting the aircraft's original configuration, a 5-point safety belt system has been modeled, comprising the left and right shoulder belts, the left and right lap belts, and the lift buckle. Belt parts are FEM component that can be modelled with truss or membrane elements in order to be able to model complex behavior such as multi-directional belt slip, submarining and roll-out. A belt can be tied to a finite element belt segment. All the belt model options can be used, including retractors, pretensioners and load limiters. The finite element belt segment can slide over the dummy surfaces subjected to Coulomb friction. Sub-cycling of the finite element time integration with respect to the multibody time integration (where the multibody time step is a multiple of the finite element time step) is implemented in order to reduce CPU time [119].

As can be seen from Figure 77 and Figure 78, the belts segments are anchored to the belt joints. The compliance of the joints is restrained using distance-force characteristics that were tuned to represent the local deformability of each part of the aircraft and energy absorbing structures (as was described in the previous section 5.4.2). The contact characteristics and material properties of the seat cushion were tuned in order to simulate accurate interactions with the dummy during its relative motion, a schematic is illustrated in Figure 79.

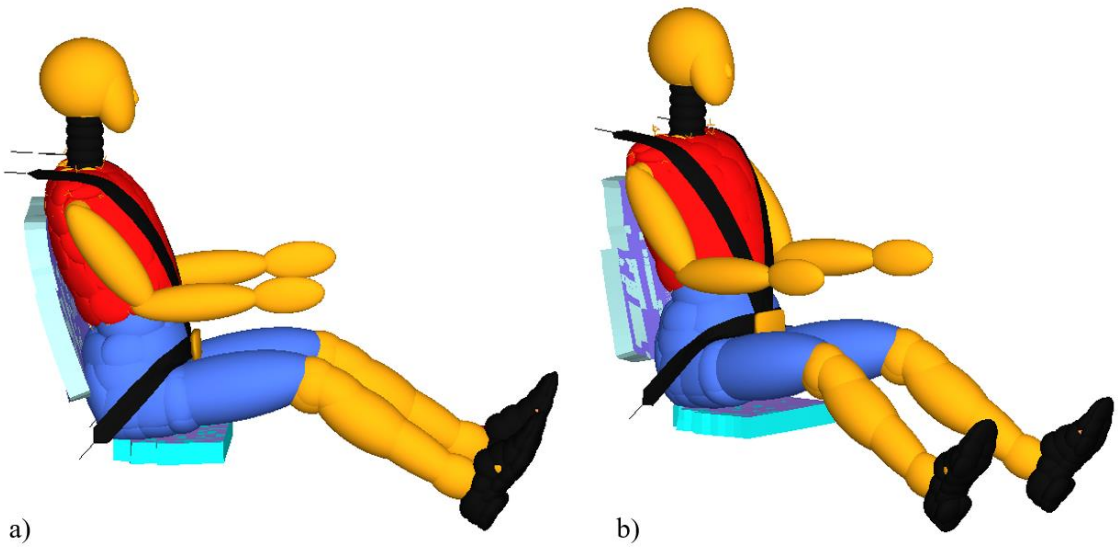

Figure 77 Hybrid III 50th Percentile Dummy and restraint system a) side view, b) iso view.

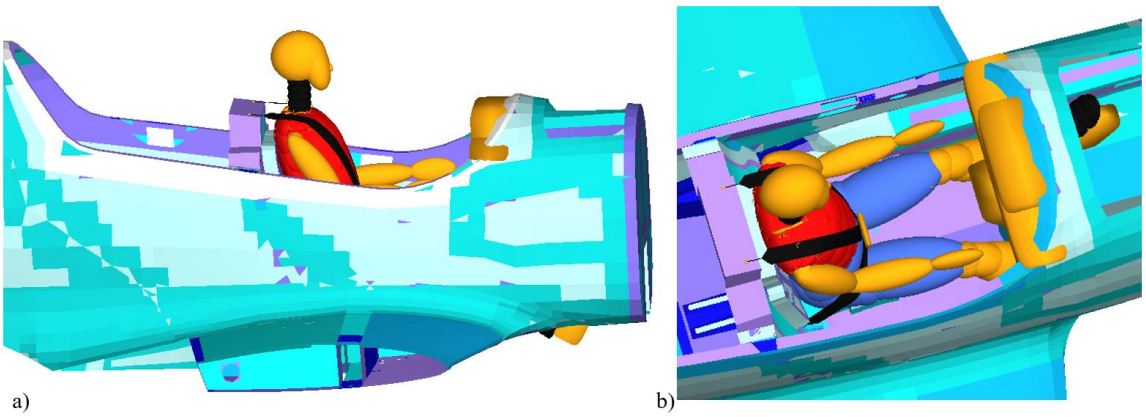

Figure 78 Hybrid III 50th Percentile Dummy positioned in the aircraft seat a) side view, b) top view.

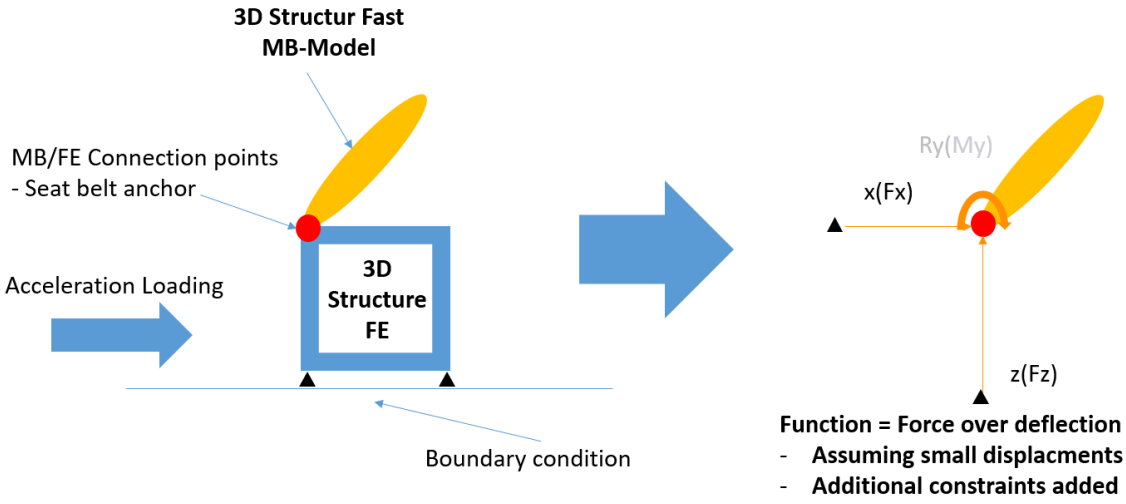

Figure 79 Schematic of the connection point to a structure [124].

5.4.4. Initial conditions

After establishing the structural model by configuring parameters like friction functions, stiffness functions, and material properties, initial conditions were defined that vary based on the specific T1 and T2 tests, as previously outlined in Table 2 within section 3.4. Test 1 and Test 2 were carried out on the forward seat, so onto the pilot's seat. An impact or collision event is frequently described in terms of a *crash pulse* (Figure 80). A crash pulse is a description of the accelerations occurring in the crash over time, or the acceleration-time history of the crash. Although the shape of a crash pulse can be highly complex and variable from crash to crash, for practical purposes, most aircraft and automobile crash pulses may be considered to be generally triangular in shape. This assumption vastly simplifies calculations related to the crash and provides reasonable estimates of acceleration

exposure for field investigators. Note that in a triangular pulse, the average acceleration of a pulse is one-half of the peak acceleration [125]. If the velocity of the vehicle at the time of the crash can be estimated and the stopping distance (vehicle crush plus soil deformation) measured then the acceleration of the vehicle during the crash can be estimated through a simple formula, assuming a triangular pulse:

$$Peak\ G = \frac{v^2}{(g) \cdot s} \tag{42}$$

where: v = velocity change of the impact;

s = stopping distance;

g = acceleration of gravity at sea level (9.8 m/s^2) [125].

The worst conditions, according to CS 23.562, correspond to a crash deceleration load of 19 G and 26 G respectively for Test 1 and Test 2 were considered (Figure 80).

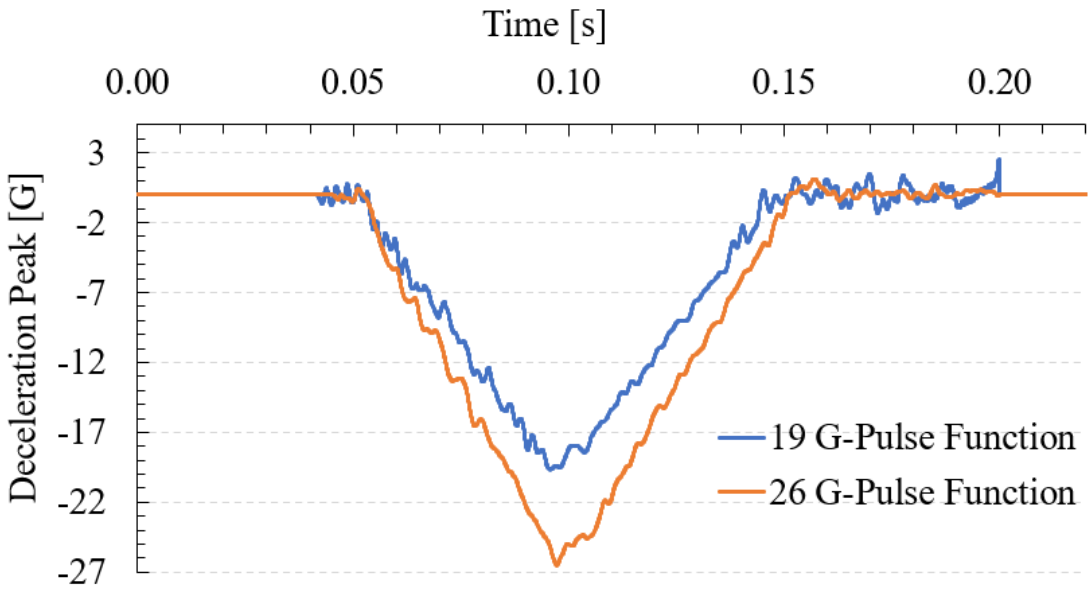

Figure 80 Triangular Crash Pulse for test T1 (19G) and T2 (26 G).

As the seat is integrated into the aircraft, it was necessary to tilt the entire aircraft by 60 degrees with respect to the ground for Test T1 (Figure 81) and 0 degrees with respect to the ground for Test T2 (Figure 81b) in order to comply with the CS 23.562 requirements (§3.4, Table 2). Pre-test conditions were considered in order to account for the influence of the occupant's weight on the seat.

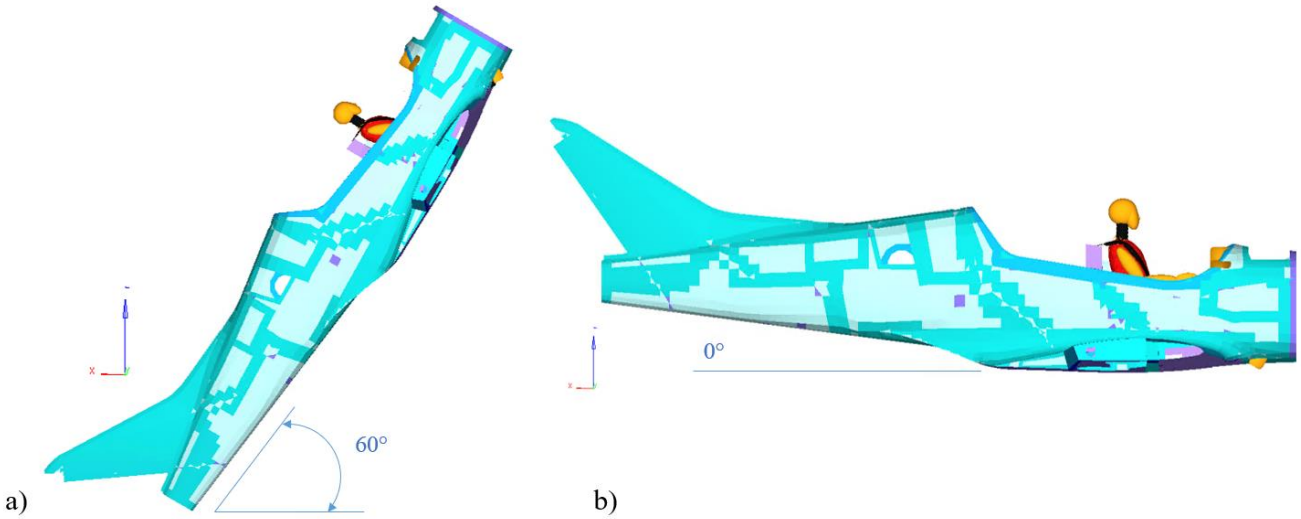

Figure 81a) 60-degree seat pitch angle for T1 test and b) 0-degree seat pitch angle for T2 test.

5.4.5. TEST 1 Dummy & Safety System Response

For the simulation of Test 1, the results obtained by considering the occupant seated directly on the rigid seat (without cushion) were compared with those obtained by considering the occupant seated on a foam cushion, either 50 mm or 100 mm thick, each with different densities. In Chapter 4, the characterization of these polyurethane foams with densities of 85, 65, and 45 kg/m³, respectively referred as type A, B and C, was extensively discussed. The first dynamic simulation was conducted without use of any seat cushion in order to evaluate the lumbar load exerted on the passenger without any energy absorbing material. Results are shown in Figure 82 with those obtained by the three foams considering a 50 mm (Figure 82a) and a 100 mm (Figure 82) thick seat cushion. Analyzing the provided graphs reveals a consistent breach of the Lumbar Spine load limit of 6675N. Notably, it is intriguing to observe that the peak load achieved with the rigid seat is marginally higher than that attained with the 50mm cushion for both foam type A and type B, as indicated by the data in Table 17. This suggests that the cushion itself can absorb a minimal amount of energy. What's even more interesting is the substantial peak load of 14596 N recorded for foam type C, the softest material, which significantly surpasses the others. Specifically, the peak load for the rigid seat is 9789 N, whereas for type A and type B, it is 9355 N and 9608 N, respectively. The peak lumbar loads remain consistently high when using the 100 mm cushions, reaching 12895, 14479, and 15207, respectively, for type A, type B, and type C. It's interesting to note that lumbar loads increase as the foam density decreases. Clearly, as seen in the graphs in Figure 83, which represent tests conducted with both the rigid seat and the 50 mm (Figure 83a) and 100 mm (Figure 83b) thick cushions, the 8900 N limit for the belt straps is consistently maintained. An interesting observation is that the peak force of 929 N obtained with the rigid seat is lower than what is achieved with the 50 mm thick cushions. This

disparity arises due to the fixed-point nature of the restraint system, ensuring that once the dummy is positioned and the belts are secured, there is no possibility of creating a gap during the test. Consequently, the dummy's position remains unchanged. The phenomenon of the dummy sinking into the cushion is evident in Figure 84a and b for the 50 mm thick type A foam, and even more pronounced in Figure 84c and d for the 100 mm thick type A foam. This sinking effect introduces variations in the results obtained for the belt straps. Specifically, the results for the 50 mm cushion show values of 1664, 1810, and 1456 N, respectively for types A, B, and C foam, which are considerably higher than those obtained with the 100 mm cushion, where values of 888, 953, and 1046 N, respectively for types A, B, and C foams, are recorded (Table 17). This is primarily because the ability of the dummy to sink deeply into the 100 mm cushion creates a significant gap between the dummy and the restraint system. Consequently, the initial seating position set for the dummy is altered, resulting in a noteworthy increase in lumbar load that, interestingly, does not significantly impact the loads on the belt straps. The presence of a significant gap, with the belts remaining 'loose,' leads to an irregular response in the curves obtained for the 100 mm cushion, which exhibits a significantly different trend from the bell-shaped curve, consistent with the deceleration impulse imparted to the system. In fact, in Figure 83b, multiple peaks corresponding to the phases when the dummy rebounds on the cushion and is restrained by the belts can be observed. As for the belts, for the sake of data readability, the curve corresponding to the maximum load values reached has been reported for each test. In this type of test, it consistently corresponds to the curve obtained for the upper attachment point of the shoulder harness.

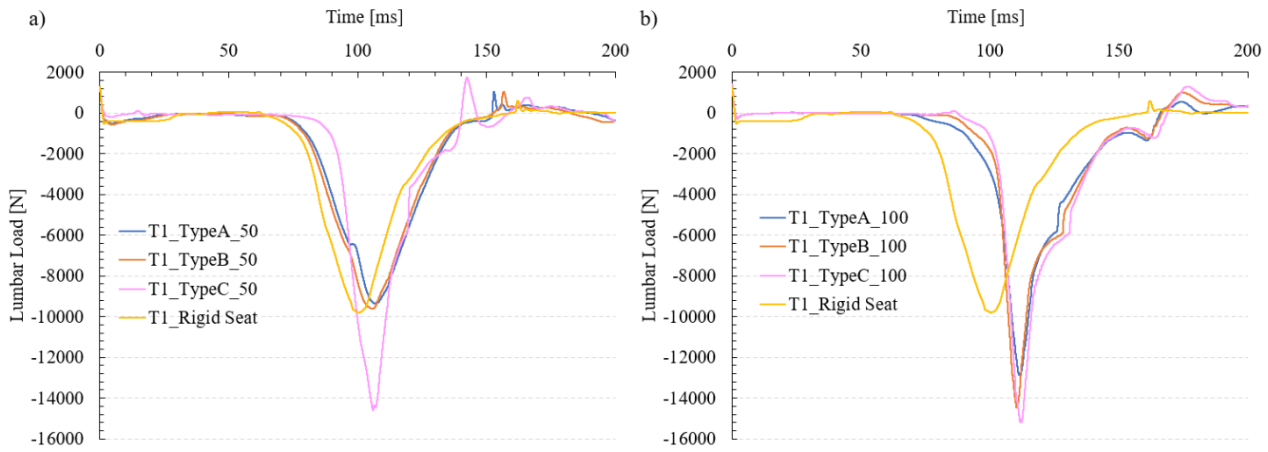

Figure 82 Test 1 comparison of the lumbar load vs. time obtained considering the rigid seat structure and the three foam types for a) 50 mm seat cushion, b) 100 mm seat cushion.

The limit of 1000 for the HIC injury parameter is consistently well met as shown from data reported in Table 17. As can be seen from Figure 84e, which depicts the maximum extension the dummy

reaches during the test, the head does not collide with any object. The crash sequence for Test 1is shown in Figure 85 from 0 to 200 ms for type A foam cushion of 50 mm (Figure 85a, b, c, d, e) and 100 mm (Figure 85f, g ,h, i, j).

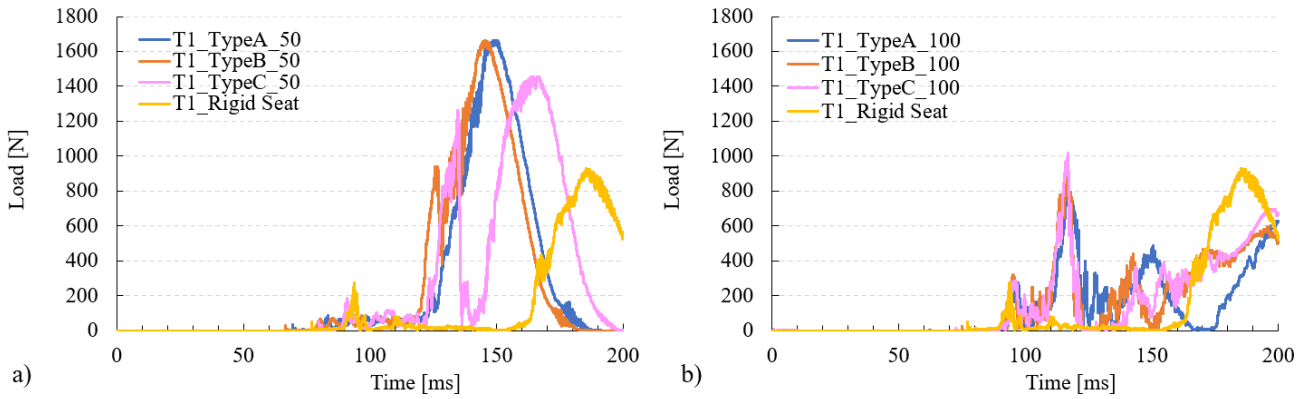

Figure 83 Test 1 comparison of the belt strap load vs. time obtained considering the rigid seat structure and the three foam types for a) 50 mm seat cushion, b) 100 mm seat cushion.

Table 17 Comparison of TEST 1 peak results.

T1-19 G								
Injury	Target	Rigid Seat	3D Model – 50 mm Foam			3D Model – 100 mm Foam		
			Type A	Type B	Type C	Type A	Type B	Type C
HIC 36	1000	84.7	81.7	79.5	143.6	156.1	143.0	169.5
Lumbar Spine [N]	6675	9789	9355	9608	14596	12895	14479	15207
Belt Strap [N]	8900	929	1664	1810	1456	888	953	1046

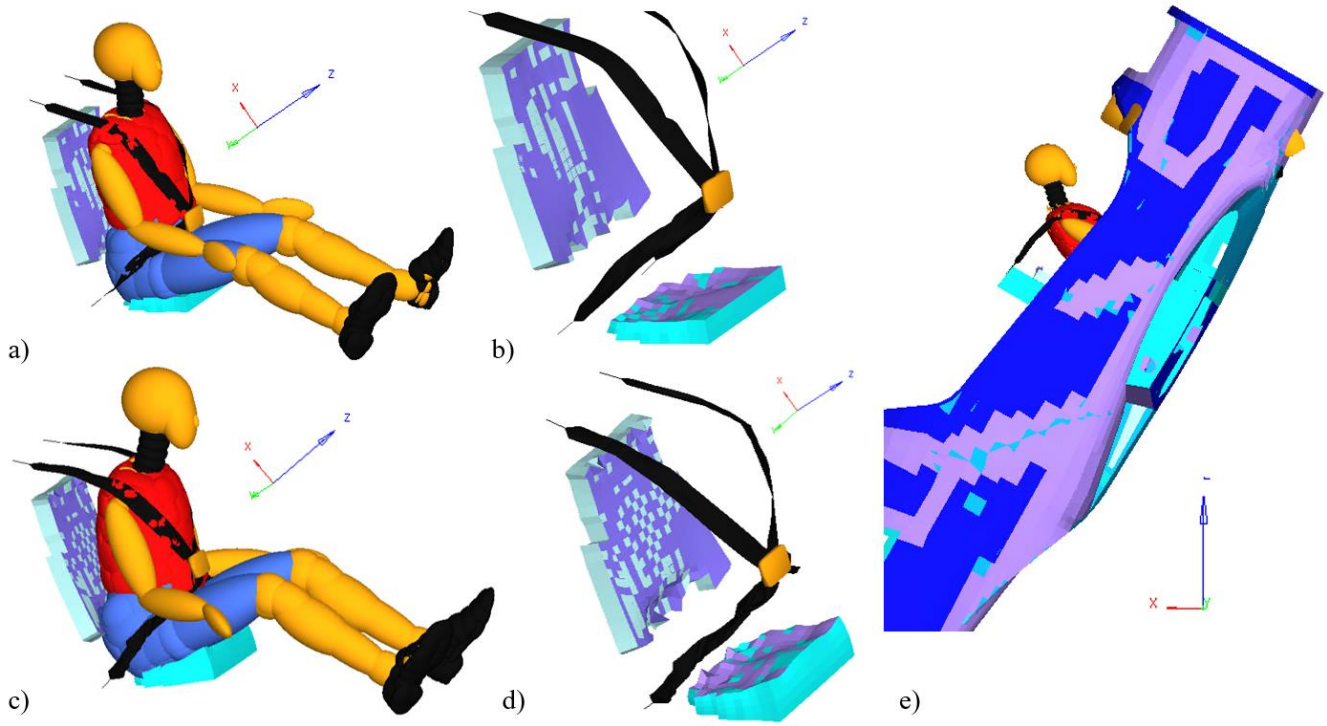

Figure 84 Test 1 a) Max dummy penetration into the 50 mm cushion, b) max deformation of the 50 mm seat cushion and of the restraint system, c) max dummy penetration into the 100 mm cushion, d) max deformation of the 100 mm seat cushion and of the restraint system, e) maximum head extension.

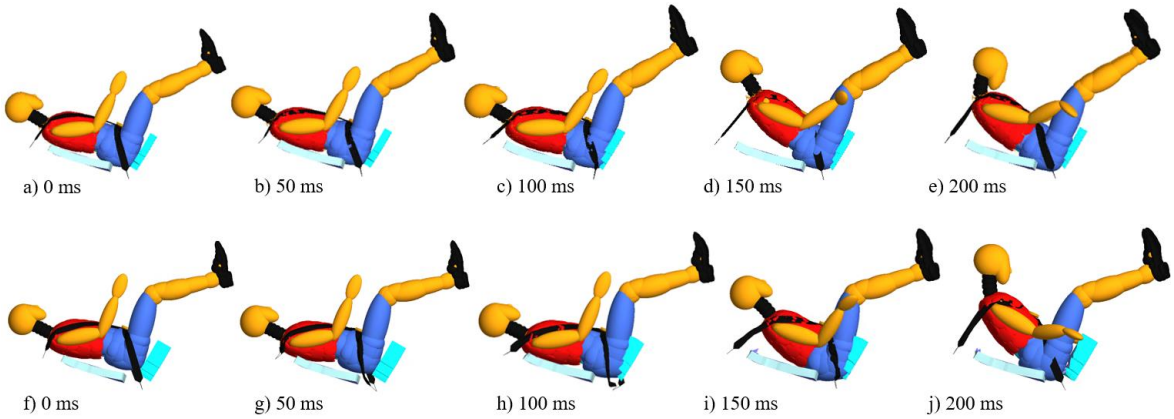

Figure 85 Test 1 crash sequence from 0 to 200 ms for type A foam cushion of 50 mm (top row) and 100 mm (bottom row).

5.4.6. TEST 2 Dummy & Safety System Response

As was already done for Test 1, also for Test 2 the results obtained by considering the occupant seated directly on the rigid seat (without cushion) were compared with those obtained by considering the occupant seated on a foam cushion, either 50 mm or 100 mm thick, each with different densities. Unlike Test 1, where the predominant load component is vertical, Test 2 involves an impact load in the longitudinal direction with a lateral component. Consequently, Test 1 and Test 2 yield entirely distinct results. As illustrated in Figure 86, it is evident that in this scenario, the compression loads on the lumbar and pelvic regions are not of primary concern; instead, it's the belt strap loads depicted in Figure 87 that are critical. Figure 88 vividly demonstrates the impact of Test 2, with a deceleration impulse of 26 G, causing the pilot to be forcefully propelled forward, sliding across the cushion, and secured by the harness system. In contrast to Test 1, where the cushion played a pivotal safety role, Test 2 places paramount importance on the harness system for safety. The graphs in Figure 86a (50 mm cushion) and Figure 86b (100 mm cushion) exhibit a markedly irregular pattern. Positive loads prevail, especially in the rigid seat test. Nonetheless, Table 18 includes the maximum recorded negative pelvis load value during the test. In stark contrast to the preceding scenario, which pertained to Test 1, Test 2 reveals a notable consistency in the safety belt graphs, demonstrating a coherent response to the triangular pulse deceleration of 26 G. As depicted in Figure 87a and b, the outcomes achieved with the dummy placed on the rigid seat consistently surpass those attained with the cushion. In fact, on the rigid seat, a peak load of 12976 N is observed, whereas the highest recorded value with the cushion, 8686 N, is associated with Type A using the 50 mm cushion. However, the peak values obtained with both the 50 mm cushion (Figure 87a) and the 100 mm cushion (Figure 87b) are nearly identical. This suggests that, in terms of its impact on the restraint system in Test 2, the cushion's density plays a minor role. In each type of test, the curve that recorded the maximum value has been reported, and for Test 2, it consistently coincided with the attachment point of the pelvis belts to the seat. Regarding the HIC parameter, values exceeding the permissible limit are registered in the rigid seat test, reaching 1366.9 N, and in the test utilizing the softer 50 mm cushion, Type C, where the value reaches 1008.0 N. Upon examining the maximum head extension in Figure 88e, it becomes evident that the head never makes contact with nearby objects. The crash sequence for Test 2 is shown in Figure 89 from 0 to 200 ms for type A foam cushion of 50 mm (Figure 89a, b, c, d, e) and 100 mm (Figure 89f, g ,h, i, j).

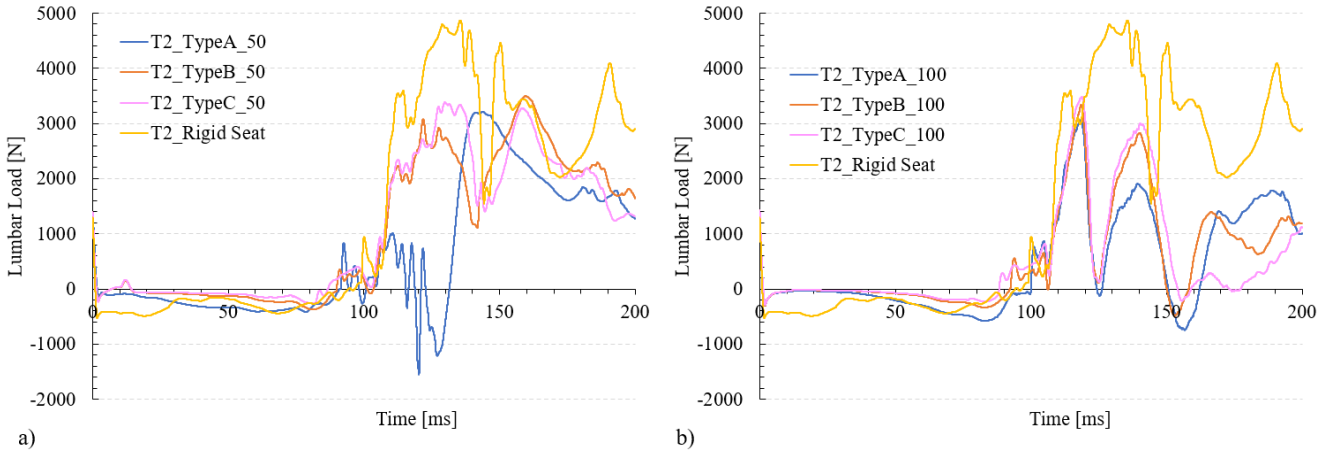

Figure 86 Test 2 comparison of the lumbar load vs. time obtained considering the rigid seat structure and the three foam types for a) 50 mm seat cushion, b) 100 mm seat cushion.

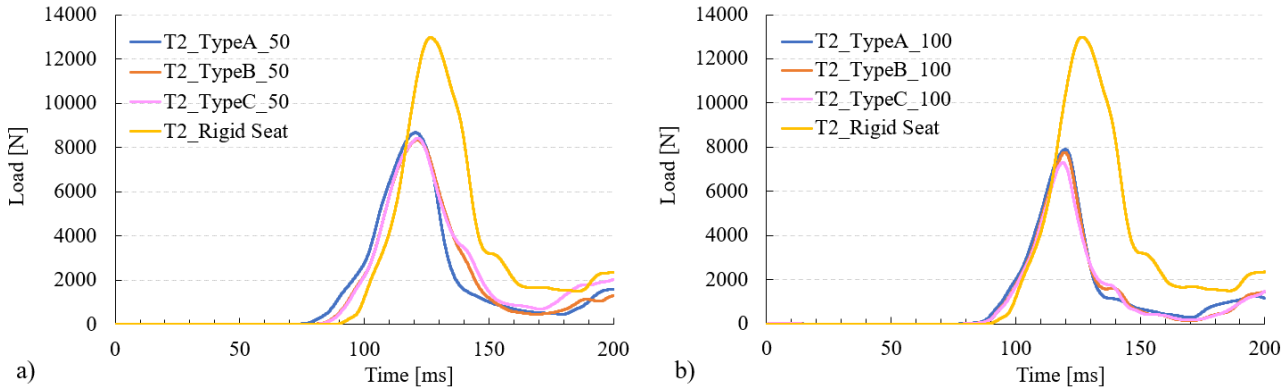

Figure 87 Test 2 comparison of the belt strap load vs. time obtained considering the rigid seat structure and the three foam types for a) 50 mm seat cushion, b) 100 mm seat cushion.

Table 18 Comparison of TEST 2 peak results.

T2-26 G								
Injury	Target	Rigid Seat	3D Model – 50 mm Foam			3D Model – 100 mm Foam		
			Type A	Type B	Type C	Type A	Type B	Type C
HIC 36	1000	1366.9	699.2	876.2	1008.0	653.7	806.4	821.5
Lumbar Spine [N]	6675	553	1561	371	259	747	563	295
Belt Strap [N]	8900	12976	8686	8333	8412	8680	7775	7298

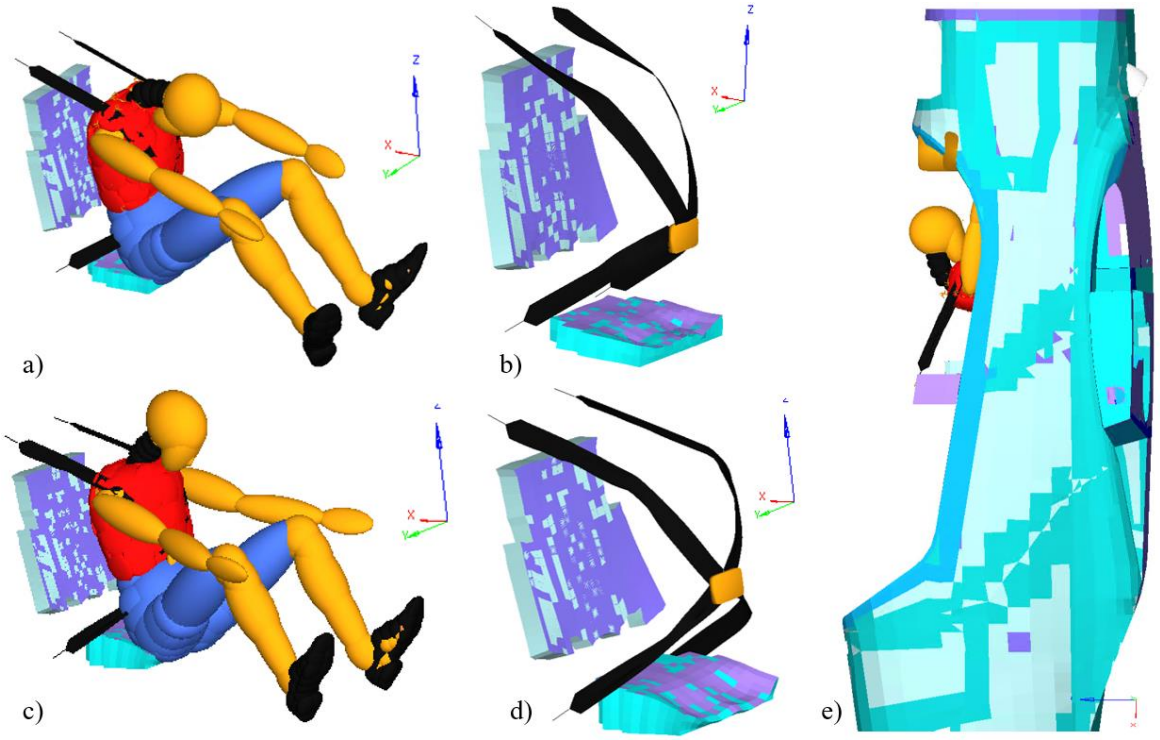

Figure 88 Test 2 a) Max dummy penetration into the 50 mm cushion, b) max deformation of the 50 mm seat cushion and of the restraint system, c) max dummy penetration into the 100 mm cushion, d) max deformation of the 100 mm seat cushion and of the restraint system, e) maximum head extension.

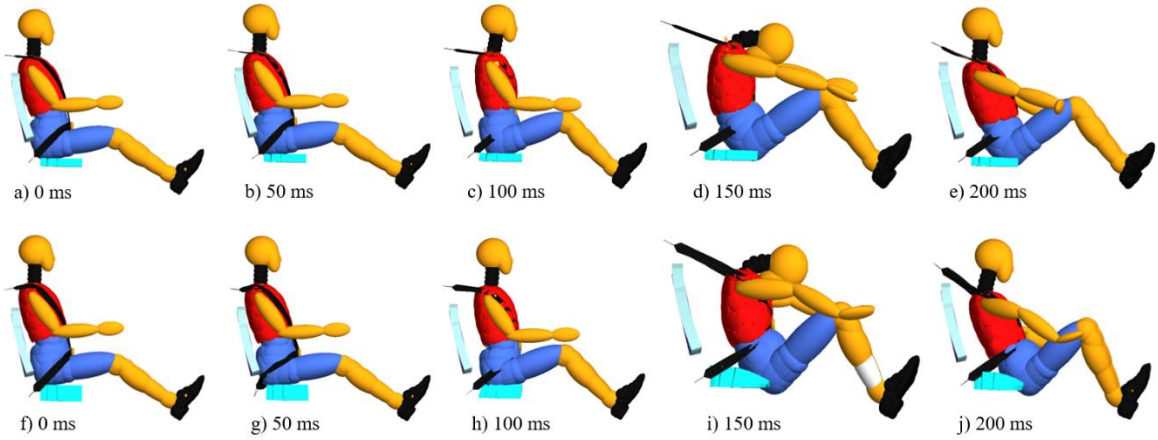

Figure 89 Test 2 crash sequence from 0 to 200 ms for type A foam cushion of 50 mm (top row) and 100 mm (bottom row).

5.4.7. Conclusions

This section has centered its attention on the numerical modeling aspect of dynamic impact tests T1 and T2. Within this study, a primary emphasis was given to the evaluation of how the seat cushion, utilized in an integrated aircraft seat, impacts the loads experienced in the lumbar and pelvic regions of the occupant. The choice of cushion material is crucial. Indeed, the seat cushion on a seat acts as

a spring/damper that is located in the primary load path between the seat occupant and the seat structure. The seat cushion is considered a primary component in the seat system. It must be included and certified as part of the seat system during the seat dynamic test program. It has been demonstrated that the seat cushion's physical properties, if improperly chosen, can amplify the lumbar-column pelvic load of the seated occupant during a vertical impact condition [126]. So, foams of three different densities of 85, 65, and 45 kg/m³, respectively referred as type A, B and C, compliant with flammability requirements, were analyzed because desirable materials for comfort are often ineffective in mitigating lumbar load, whereas effective materials for lumbar load attenuation are often unacceptable in terms of comfort. The selected foams underwent mechanical characterization and numerical modeling to ensure that Madymo accurately replicated the highly nonlinear behavior of this type of material. The most significant test for evaluating lumbar loads is the T1, characterized by a vertical component, while the T2 has proven crucial for assessing other parameters such as the loads on the restraint system and the HIC (Head Impact Criterion). Considering both tests, it can be concluded that the aircraft does not meet the targets set by the CS 23.562 regulation. Similar to findings by other authors [126], the soft foam Type C, i.e., the least dense foam, significantly amplifies the loads recorded in the occupant's lumbar region. For instance, during Test 1 with a 50 mm thick cushion made of Type C foam, a peak lumbar load of 14596 N was recorded, significantly surpassing the 9789 N load recorded when the dummy was placed on the rigid seat. This phenomenon can be attributed to the substantial alteration of the dummy's seating posture on the very soft cushion material. Foams with appropriate densities, as observed in the case of Type A and Type B, effectively mitigate these loads, albeit, in this specific case, with minimal dissipation of energy. Considering the constraints imposed by the aircraft's geometry, data obtained with a 100mm thick cushion were also analyzed. Given the integrated design of the seat, the only available option for energy dissipation is to employ a thicker seating padding. In this scenario, the tests once again did not meet the required standards. In fact, it was observed that very thick cushions significantly amplify lumbar loads, resulting in more or less the same peak value (12895, 14479, and 15207, respectively, for Type A, B, and C foam). This outcome is attributed to the occupant sinking into the seat, thereby altering the initial seating configuration of the dummy. The results of Test 2 demonstrate that cushions have a positive impact on the belt strap loads. In fact, these loads are considerably lower compared to the results obtained with the dummy positioned on the rigid seat test. As the test has not been successfully passed, carrying out an experimental test with the current configuration would be futile, expensive, and unlikely to produce reliable results. Consequently, it is imperative to move forward with a redesign of the seat structure, exploring alternative solutions or even considering radical changes, such as designing a seat that is not integrated into the fuselage.

6. Conclusions

This chapter presents an overview of the research activities and the most important results reached into this dissertation. The purpose of the research was to develop a complex numerical-experimental methodology aimed at evaluating the crashworthiness of an aeronautical seat integrated into the fuselage structure. This methodology considers not only the materials involved and their thickness but also critical impact conditions. This research has focused on applying this methodology to a specific case study, namely the seat of the Bk 160 Blackshape aircraft, actually conform to CS-VLA requirements integrated with a Special Condition agreed with EASA. The study aims to highlight the limitations of the current configuration in order to address any issues that may arise when seeking to improve the aircraft's performance in terms of weight and stall speed. In the latter case, it would be necessary to focus on reducing the loads on the lumbar and pelvic regions of the occupant to ensure compliance with the CS 23.562, which requires the physical execution of two dynamic tests.

Since the seat is integrated into the fuselage structure and the only sacrificial item is the seat cushion, the study starts with the analysis and evaluation of materials for human safety devices, particularly focusing on three soft open-cell polyurethane foams with densities of 85, 65, and 45 kg/m³. To meet flame resistance requirements, a foam containing dispersed graphite particles was chosen. Tensile, shear, and cyclic compression tests were conducted to understand material characteristics and density variations. Full-field DIC successfully captured deformations up to 90% in tension and shear and up to 80% in compression despite the absence of any speckle pattern being applied. Indeed, the expanded graphite particles dispersed in the material in a random way enhances the grayscale contrast compared to foams for which only the presence of voids in the material is exploited. This feature allows to apply full-field DIC technique, innovatively, directly exploiting the natural pattern of the specimen surface. In fact, the application of paint typically used to create the speckle pattern would crumble for this type of material at high deformations, leading to a loss of correlation. The experimental results showed that softer and less dense foams can withstand higher deformations than higher density ones; but higher density foams dissipate more energy, as seen in wider hysteresis cycles. Since there is no standard for obtaining shear characteristics of soft polyurethane foams, three different standards, using specimens with different geometries, were compared: ASTM C 273 for sandwich structures, BS 4370 for rigid sandwich structures, and the Iosipescu configuration for mostly composite materials. Once again, DIC has proven to be crucial for its versatility, allowing measurements to be taken where strain gauges and extensometers would typically be used. This is because each of the mentioned standards specifies different deformation measurement techniques. From the comparison of various tests with specimens of different geometries, it emerged that the results obtained for the ASTM C 273 setup with a 25 mm thick specimen and for the Iosipescu setup with an unnotched specimen are comparable. This led to significant material savings and enhanced

test repeatability. In fact, a specimen of 20 x 26 x 13 mm is used for the Iosipescu setup, as opposed to a specimen of 200 x 70 x 25 mm. Investigation about the Poisson's ratio find out that these ordinary foams exhibited an auxetic behavior that can be well replicated by the Hyperfoam material model available for the finite element model Abaqus. The experimental results were used for the numerical modeling of dynamic impact tests T1 and T2. The cushions were modeled using Finite Element Analysis (FEA) and then assembled into a combined numerical model, FEM + multi-body, using Simcenter Madymo software. The softest foam (Type C) significantly amplified lumbar loads during Test 1 due to occupant posture changes. Foams with suitable densities (Type A and B) mitigated these loads with minimal energy dissipation. Even with thicker cushions, the test did not meet standards, as occupant sinking altered dummy seating. Test 2 showed that cushions reduced belt strap loads compared to rigid seats. Results also revealed that, under CS 23.562 regulation, the aircraft as per the different configurations scenarios analyzes would fail to meet lumbar load targets. The experimental and numerical procedure implemented has proved to be effective in comparing different configurations and in indicating explorable alternative solutions as well as the possibility to unify the seat with the fuselage.

Multibody modeling turned out to be a versatile tool for simulating complex mechanical systems realistically, accurately representing the movement and behavior of interconnected components. Also, multibody simulations act as virtual prototypes, reducing the need for physical ones, thus saving time and costs, enhancing design efficiency and performance analysis.

In summary, this dissertation covered material analysis, seat cushion impact, and multibody modeling, highlighting the importance of material choice, design optimization, and safety assessments.

Acknowledgements

My most sincere gratitude goes to the Experimental Mechanics research group at the Polytechnic University of Bari, led by Professor Katia Casavola. Thank you for these years we have spent together, during which I have grown both personally and professionally. I would like to extend a special thank you to my supervisor, Prof. Giovanni Pappalettera, whose support has been crucial in facing the critical challenges of this research. His constant encouragement has played a pivotal role in the success of this thesis. I would also like to express my infinite gratitude to Prof. Vincenzo Moramarco, co-author in recent research projects, whose findings have been included in this thesis. His support, both personally and professionally, has been invaluable at every moment.
A special thank you goes to my corporate mentor, Engineer Lucia del Core, who deserves credit for initiating and organizing this doctoral program in collaboration with Blackshape.

I would like to express my deep appreciation to the Siemens mentors, Engineer Michiel Unger and Engineer Richard Lancashire, for the internship experience and for their unwavering support in resolving issues related to the use of the Madymo software. Their exceptional expertise and unwavering dedication to their work set them apart.

The last year of my doctoral period has been challenging and special, as I have not only created a research work but also a new life, my son Raul. I want to thank everyone for their understanding and support, especially Professor Katia Casavola, the group coordinator, who has always been kind and helpful, I have always had deep admiration for her.
A heartfelt thank you to the talented and wonderful Professors Claudia Barile and Gilda Renna. It has been an honour to work with you and participate in your activities.
A thousand thanks to Professor Emeritus Carmine Pappalettere, with whom I had the honor of working.
Thanks to my special colleagues, Simone, Vimal, and Michele.

Special thanks to my life partner, Martino, for his unwavering support and encouragement and for giving me the most beautiful gift of my life, our son, Raul.
Raul, I dedicate this work to you. Your arrival brought light. You have given deeper meaning to everything, and every day you inspire me to reach my goals.
I sincerely thank my entire family and friends, especially my little niece Nicole, as well as my special babysitter, grandmothers Maria Angela and Antonella, and my friend Arianna, who have always been present in my life and in Raul's.

Il mio più sincero ringraziamento va al gruppo di ricerca di Meccanica Sperimentale del Politecnico di Bari, guidato dalla Prof.ssa Katia Casavola. Grazie per questi anni trascorsi insieme, durante i quali sono cresciuta sia dal punto di vista umano che professionale. Desidero esprimere un ringraziamento speciale al mio supervisore, il Prof. Giovanni Pappalettera, il cui sostegno è stato fondamentale per affrontare le sfide cruciali della ricerca. Il suo costante incoraggiamento ha contribuito in modo determinante al successo di questo lavoro di tesi. Vorrei ringraziare infinitamente anche il Prof. Vincenzo Moramarco, coautore nei lavori di ricerca degli ultimi anni, i cui risultati sono stati inclusi in questa tesi. Il suo sostegno, sia dal punto di vista umano che professionale, è stato prezioso in ogni momento.
Un ringraziamento speciale va alla mia tutor aziendale, l'Ing. Lucia del Core, a cui va il merito di aver voluto e organizzato questo percorso di dottorato in collaborazione con l'azienda Blackshape.

Vorrei esprimere la mia profonda gratitudine ai tutor di Siemens, l'Ing. Michiel Unger e l'Ing. Richard Lancashire, per l'esperienza di tirocinio e per il loro costante supporto nella risoluzione delle questioni legate all'uso del software Madymo. La loro eccezionale competenza e la loro dedizione al lavoro li distinguono.

L'ultimo anno di dottorato è stato impegnativo e speciale, in quanto ho non solo creato un lavoro di ricerca, ma anche una nuova vita, il piccolo Raul. Desidero ringraziare tutti per la comprensione e il supporto, in particolare la Prof.ssa Katia Casavola, coordinatrice del gruppo, sempre gentile e disponibile, per cui nutro una stima infinita.
Un caloroso ringraziamento alle talentuose e splendide Professoresse Claudia Barile e Gilda Renna. È stato un onore lavorare con voi e partecipare alle vostre attività.
Mille grazie al Prof. Emerito Carmine Pappalettere con cui ho avuto l'onore di poter lavorare.
Grazie ai miei colleghi speciali, Simone, Vimal e Michele.

Ringrazio il mio compagno di vita Martino per il suo sostegno e l'incoraggiamento incondizionato e per avermi fatto il regalo più bello della mia vita, nostro figlio Raul.
Grazie a te Raul, a cui dedico questo lavoro, il tuo arrivo è stato luce. Hai dato un significato più profondo a tutto, e ogni giorno mi sproni a raggiungere i miei obiettivi.

Ringrazio di cuore tutta la mia famiglia e i miei amici, in particolare la piccola nipotina Nicole, nonché mia baby-sitter speciale, le nonne Maria Angela e Antonella e la mia amica Arianna, sempre presenti nella mia vita e in quella del piccolo Raul.

Bibliography

[1] https://blackshape.ro/news/blackshape-launches-bk160-gabriel/.

[2] Ronald I. C. Bartsch, International Aviation Law: A Practical Guide, Ashgate, United Kingdom, 2012.

[3] E. A. S. Agency, EASA & CONTINUING AIRWORTHINESS SEMINAR, in: EVEREST EVENTS, 2014.

[4] EASA, Annual Safety Review, 2022.

[5] Regulation (EU) No 996/2010 of the European Parliament and of the Council of 20 October 2010 on the investigation and prevention of accidents and incidents in civil aviation and repealing Directive 94/56/EC.

[6] https://transport.ec.europa.eu/transport-modes/air/aviation-safety-policy-europe/aviation-safety-rules/airworthiness_en.

[7] Commission Regulation (EU) No 748/2012 of 3 August 2012 laying down implementing rules for the airworthiness and environmental certification of aircraft and related products, parts and appliances, as well as for the certification of design and production organizations.

[8] Commission Regulation (EU) No 1321/2014 of 26 November 2014 on the continuing airworthiness of aircraft and aeronautical products, parts and appliances, and on the approval of organisations and personnel involved in these tasks Text with EEA relevance.

[9] T. Sgobba, B-737 MAX ED IL FALLIMENTO DEL SISTEMA DI REGOLAMENTAZIONE, Associazione Italiana Cultura Qualità, Settore Aerospace, Marzo 2020, pp 4-12.

[10] European Aviation Safety Agency, «https://www.enac.gov.it/sicurezza-aerea/aeronavigabilita-iniziale/omologazione-organizzazioni-di-progettazioni/prodotti/certificazioni-di-tipo-di-competenza-easa».

[11] J. Díaz, M. Costas, Crashworthiness, in: Encyclopedia of Continuum Mechanics, Springer Berlin Heidelberg, Berlin, Heidelberg, pp. 469–486, 2020. https://doi.org/10.1007/978-3-662-55771-6_223.

[12] T.R. Hurley, J.M. Vandenburg, Crashworthiness Design Guide Small Airplane Integrated Design and Manufacturing, April 12, 2002.

[13] C. Letondal, C. Hurter, R. Lesbordes, J.-L. Vinot, S. Conversy, Flights in my hands, in: Proceedings of the SIGCHI Conference on Human Factors in Computing Systems, ACM, New York, NY, USA, pp. 2175–2184, 2013. https://doi.org/10.1145/2470654.2481300.

[14] T.C. Chu, W.F. Ranson, M.A. Sutton, W.H. Peters, Applications of Digital.Image-Correlation Techniques to Experimental Mechanics, Exp. Mech., vol. 25, no. 3, pp. 232–244, 1985. https://doi.org/10.1007/ BF02325092.

[15] C. Casavola, L. Del Core, V. Moramarco, G. Pappalettera, M. Patronelli, Full-field mechanical characterization of polyurethane foams under large deformations by digital image correlation, Mechanics of Advanced Materials and Structures, 2021. https://doi.org/10.1080/15376494.2021.1905915.

[16] C. Casavola, L. Del Core, V. Moramarco, G. Pappalettera, M. Patronelli, Experimental and numerical analysis of the Poisson's ratio on soft polyurethane foams under tensile and cyclic compression load, Mechanics of Advanced Materials and Structures, 2021. https://doi.org/10.1080/15376494.2021.1994061.

[17] C. Casavola, L. Del Core, V. Moramarco, G. Pappalettera, M. Patronelli, Full-Field Experimental Study and Numerical Modeling of Soft Polyurethane Foam Subjected to Cyclic Loading, in: MDPI AG, p. 20, 2022. https://doi.org/10.3390/psf2022004020.

[18] H.M.C.C. Somarathna, S.N. Raman, D. Mohotti, A.A. Mutalib, K.H. Badri, The use of polyurethane for structural and infrastructural engineering applications: A state-of-the-art review, Constr Build Mater. vol. 190, pp. 995–1014, 2018. https://doi.org/10.1016/j.conbuildmat.2018.09.166.

[19] N. V. Gama, A. Ferreira, A. Barros-Timmons, Polyurethane foams: Past, present, and future, Materials., vol. 11, 2018. https://doi.org/10.3390/ma11101841.

[20] C. Ge, L. Priyadarshini, D. Cormier, L. Pan, J. Tuber, A preliminary study of cushion properties of a 3D printed thermoplastic polyurethane Kelvin foam, Packaging Technology and Science, vol. 31, pp. 361–368, 2018. https://doi.org/10.1002/pts.2330.

[21] C. Jackson, A.J. Emck, M.J. Hunston, P.C. Jarvis, A. Firmin, A Simple Comparison of the Characteristics of Energy-Absorbing Foams for Use in Safety Cushions in Glider Cockpit Environments, Tech. Soaring., vol. 33, no. 2, pp. 47–53, 2009.

[22] M. Jankowski and M. Kotełko, Dynamic compression tests of a polyurethane flexible foam as a step in modelling impact of the head to the vehicle seat head restraint, FME Trans., vol. 38, pp. 121–127, 2010.

[23] N.J. Mills, C. Fitzgerald, A. Gilchrist, and R. Verdejo, Polymer foams for personal protection: Cushions, shoes and helmets, Compos. Sci. Technol., vol. 63, no. 16, pp. 2389–2400, 2003. https://doi.org/10.1016/S0266-3538(03)00272-0.

[24] D. V. W. M. de Vries, Characterization of polymeric foams, Eindhoven Univ. Technol., no. July, pp. 34, 2009.

[25] A. T. Huber and L. J. Gibson, Anisotropy of foams, J. Mater. Sci., vol. 23, no. 8, pp. 3031–3040, 1988. DOI: 10.1007/ BF00547486.

[26] L. J. Gibson and M. F. Ashby, 1997. Cellular Solids, Cambridge University Press, Cambridge, UK. DOI: 10.1017/ CBO9781139878326.

[27] Mills N. J, Polymer Foams Handbook: Engineering and Biomechanics Applications and Design Guide, Butterworth Heinemann, p. 531, 2007.

[28] A. Kottar, H.P. Degischer, and B. Kriszt, Rontgen-computerto- € mographie zur charakterisierung von zellularem aluminium und seiner verformung, Mat-Wiss. Werkstofftech., vol. 31, no. 6, pp. 465–469, 2000. https://doi.org/10.1002/1521-4052(200006)31:6< 465::AIDMAWE465> 3.0.CO;2-G.

[29] I.M. Daniel, J.-M. Cho, Characterization of Anisotropic Polymeric Foam Under Static and Dynamic Loading, Exp Mech. 51 (2011) 1395–1403. https://doi.org/10.1007/s11340-011-9466-3.

[30] M. Avalle, G. Belingardi, and R. Montanini, Characterization of polymeric structural foams under compressive impact loading by means of energy-absorption diagram, Int. J. Impact Eng., vol. 25, no. 5, pp. 455–472, 2001. https://doi.org/10.1016/S0734- 743X(00)00060-9.

[31] J. Zhang, Z. Lin, A. Wong, N. Kikuchi, V.C. Li, A.F. Yee, G.S. Nusholtz, Constitutive Modeling and Material Characterization of Polymeric Foams, J Eng Mater Technol, vol. 119, pp. 284–291. https://doi.org/10.1115/1.2812258.

[32] W.Y. Lu, M. Neidigk, and N. Wyatt, Cyclic loading experiment for characterizing foam viscoelastic behavior, Conf. Proc. Soc. Exp. Mech. Ser., vol. 4, pp. 135–144, 2017. https://doi.org/10.1007/978-3- 319-42028-8_16.

[33] J. V. Mane, S. Chandra, S. Sharma, H. Ali, V.M. Chavan, B.S. Manjunath, R.J. Patel, Mechanical Property Evaluation of Polyurethane Foam under Quasi-static and Dynamic Strain Rates- An Experimental Study, in: Procedia Eng, Elsevier Ltd, pp. 726–731, 2017. https://doi.org/10.1016/j.proeng.2016.12.160.

[34] G. Pampolini, M. Raous, Nonlinear elasticity, viscosity and damage in open-cell polymeric foams, Archive of Applied Mechanics, vol. 84, pp. 1861–1881, 2014. https://doi.org/10.1007/s00419-014-0891-5.

[35] M. Petru and O. Novak, Measurement and Numerical Modeling of Mechanical Properties of Polyurethane Foams, Asp. Polyurethanes, pp. 73–109, 2017. https://doi.org/10.5772/intechopen.69700.

[36] G. Silber, M. Alizadeh, M. Salimi, Large deformation analysis for soft foams based on hyperelasticity, Journal of Mechanics, vol. 26, pp. 327–334, 2010. https://doi.org/10.1017/S1727719100003889.

[37] A.D. Marter, A.S. Dickinson, F. Pierron, and M. Browne, A practical procedure for measuring the stiffness of foam like materials, Exp. Tech., vol. 42, no. 4, pp. 439–452, 2018. https://doi.org/10.5258/SOTON/404042.

[38] B.T. Werner, W.Y. Lu, and K. Connelly, Compression testing of aged low density flexible polyurethane foam, Conf. Proc. Soc. Exp. Mech. Ser., vol. 4, pp. 145–151, 2011. DOI: 10.1007/978-3- 319-42028-8_17.

[39] A.M. Korsunsky, M. Sebastiani, E. Bemporad, Residual stress evaluation at the micrometer scale: Analysis of thin coatings by FIB milling and digital image correlation, Surf Coat Technol, vol. 205, pp. 2393–2403, 2010. https://doi.org/10.1016/j.surfcoat.2010.09.033.

[40] W.A. Take, Thirty-sixth canadian geotechnical colloquium: Advances in visualization of geotechnical processes through digital image correlation, Canadian Geotechnical Journal, vol. 52, pp. 1199–1220, 2015. https://doi.org/10.1139/cgj-2014-0080.

[41] C. Barile, C. Casavola, G. Pappalettera, Digital image correlation comparison of damaged and undamaged aeronautical CFRPs during compression tests, Materials, vol. 12, 2019. https://doi.org/10.3390/ma12020249.

[42] D.A. Apostol, D.M. Constantinescu, L. Marşavina, E. Linul, Analysis of deformation bands in polyurethane foams, in: Key Eng Mater, Trans Tech Publications Ltd, 2014: pp. 250–253. https://doi.org/10.4028/www.scientific.net/KEM.601.250.

[43] D.M.C. and F.S. D.A. Apostol, Characterization and damage assessment of polyurethane foams subjected to compression testing, Materia Plastics, vol. 56, pp. 454–457, 2016.

[44] H. Jin, W.Y. Lu, S. Scheffel, T.D. Hinnerichs, M.K. Neilsen, Full-field characterization of mechanical behavior of polyurethane foams, Int J Solids Struct, vol. 44, pp. 6930–6944, 2007. https://doi.org/10.1016/j.ijsolstr.2007.03.018.

[45] O. Jirousek, T. Doktor, D. Kytyr, P. Zlamal, et al., X-ray and finite element analysis of deformation response of closed-cell metal foam subjected to compressive loading, J. Inst., vol. 8, no. 02, p. C02012, 2013. https://doi.org/10.1088/1748-0221/8/02/C02012.

[46] T. Zhang, E. Maire, J. Adrien, P.R. Onck, L. Salvo, Local Tomography Study of the Fracture of an ERG Metal Foam, Adv Eng Mater, vol. 15, pp. 767–772, 2013. https://doi.org/10.1002/adem.201300004.

[47] S. Hensley, M. Christensen, S. Small, D. Archer, E. Lakes, R. Rogge, Digital image correlation techniques for strain measurement in a variety of biomechanical test models, Acta Bioeng Biomech, vol. 19, pp. 187–195, 2017. https://doi.org/10.5277/ABB-00785-2016-04.

[48] S. Koumlis, L. Lamberson, Strain Rate Dependent Compressive Response of Open Cell Polyurethane Foam, Exp Mech, vol. 59, pp. 1087–1103, 2019. https://doi.org/10.1007/s11340-019-00521-3.

[49] A. Jung, K. Al Majthoub, C. Jochum, S.M. Kirsch, F. Welsch, S. Seelecke, S. Diebels, Correlative digital image correlation and infrared thermography measurements for the

investigation of the mesoscopic deformation behaviour of foams, J Mech Phys Solids, vol. 130, pp. 165–180, 2019. https://doi.org/10.1016/j.jmps.2019.06.009.

[50] S. Kishimoto, Q. Wang, Y. Tanaka, Y. Kagawa, Compressive mechanical properties of closed-cell aluminum foam-polymer composites, Compos B Eng, vol. 64, pp. 43–49, 2014. https://doi.org/10.1016/j.compositesb.2014.04.009.

[51] P. Bing, D. W, Y. Xia, Incremental calculation for large deformation measurement using reliability-guided digital image correlation, in: Opt Lasers Eng, pp. 586–592, 2012. https://doi.org/10.1016/j.optlaseng.2011.05.005.

[52] Y. Wang and A.M. Cuitio, Full-field measurements of heterogeneous deformation patterns on polymeric foams using digital image correlation, Int. J. Solids Struct., vol. 39, no. 13-14, pp. 3777–3796, 2002. https://doi.org/10.1016/S0020-7683(02)00176-2.

[53] F. Hild, B. Raka, M. Baudequin, S. Roux, and F. Cantelaube, Multiscale displacement field measurements of compressed mineral-wool samples by digital image correlation, Appl. Opt., vol. 41, no. 32, pp. 6815–6828, 2002. https://doi.org/10.1364/AO.41.006815.

[54] UNI EN ISO 1798:2008 Flexible cellular polymeric materials Determination of tensile strength and elongation at break, 2008

[55] UNI EN ISO 3386-2:1997/Amd.1:2010 Flexible cellular polymeric materials-Determination of stress-strain Characteristics in compression, 2010.

[56] ASTM, C 273-00 Standard Test Method for Shear Properties of Sandwich Core Materials, Annual Book of ASTM Standards, vol. 15.03. 100 Barr Harbor Drive, West Conshohocken, PA 19428-2959, United States, 2000.

[57] BS4370 Part 2, British Standard Methods of Test for Rigid Cellular Materials, British Standard Institution, London , 1973.

[58] ASTM D5379/D5379M − Standard Test Method for Shear Properties of Composite Materials by the V-Notched Beam Method. 2012, ASTM International: West Conshohocken, PA.

[59] M. Smith, ABAQUS/Standard User's Manual, Version 6.9, Dassault Syst——————emes Simulia Corp, Providence, RI, 2009.

[60] L. Mullins, Softening of Rubber by Deformation, Rubber Chem Technol, vol. 42, no. 1, pp. 339–362, 1969. DOI: 10.5254/1. 3539210

[61] M.A. Sutton, J.H. Yan, V. Tiwari, H.W. Schreier, J.J. Orteu, The effect of out-of-plane motion on 2D and 3D digital image correlation measurements, Opt Lasers Eng, vol. 46, pp. 746–757, 2008. https://doi.org/10.1016/j.optlaseng.2008.05.005.

[62] F. Pierron, Identification of Poisson's ratios of standard and auxetic low-density polymeric foams from full-field measurements, Journal of Strain Analysis for Engineering Design, vol. 45, pp. 233–253, 2010. https://doi.org/10.1243/03093247JSA613.

[63] C. E. Shannon, A mathematical theory of communication, Bell Syst. Tech. J., vol. 27, no. 3, pp. 379–423, 1948. DOI: 10.1002/j. 1538-7305.1948.tb01338.x.

[64] X.Y. Liu, R.L. Li, H.W. Zhao, T.H. Cheng, G.J. Cui, Q.C. Tan, G.W. Meng, Quality assessment of speckle patterns for digital image correlation by Shannon entropy, Optik (Stuttg), vol. 126, pp. 4206–4211, 2015. https://doi.org/10.1016/j.ijleo.2015.08.034.

[65] R. Belda, R. Megías, N. Feito, A. Vercher-Martínez, E. Giner, Some practical considerations for compression failure characterization of open-cell polyurethane foams using digital image correlation, Sensors (Switzerland), vol. 20, pp. 1–21, 2020. https://doi.org/10.3390/s20154141.

[66] B. Guo, F. Pierron, R. Rotinat, Identification of low density polyurethane foam properties by DIC and the virtual fields method, in: ICEM 2008: International Conference on Experimental Mechanics 2008, SPIE, pp. 737554, 2008. https://doi.org/10.1117/12.839331.

[67] R.W. Ogden, Large deformation isotropic elasticity: on the correlation of theory and experiment for compressible rubberlike solids, 1972.

[68] R.W. Ogden, D.G. Roxburgh, A pseudo–elastic model for the Mullins effect in filled rubber, Proceedings of the Royal Society of London. Series A: Mathematical, Physical and Engineering Sciences, vol. 455, pp. 2861–2877, 1999. https://doi.org/10.1098/rspa.1999.0431.

[69] K. Ramaswamy, V. L. Virupaksha, J. Polan, and B. Tripathy, Validation of Expanded Polypropylene (EPP) Foam Material Models for Low-Speed Bumper and Pedestrian Protection Applications, SAE Tech. Pap., 2017-01-0363, 2017. https://doi.org/10.4271/2017-01-0363.

[70] D.J. O'connor, An evaluation of test methods for shear modulus of sandwich cores, Int J Cem Comp Lightweight Concr, vol. 6, no 1, pp. 3-12, 1984. https://doi.org/10.1016/0262-5075(84)90054-X.

[71] M.R.M. Rejab, M.S.M. Sani, M.M. Noor, K. Kadirgama, M.M. Rahman, A. Alias, Mechanical behaviour of polymeric foam core at various orientation angles, in: WIT Transactions on the Built Environment, pp. 429–438, 2010. https://doi.org/10.2495/HPSM100401.

[72] I. Beverte, An experimental method for the investigation of rigid polyurethane foams in shear, Journal of Cellular Plastics, vol. 54, pp. 851–884, 2018. https://doi.org/10.1177/0021955X18782080.

[73] K.B. Park, H.T. Kim, N.Y. Her, J.M. Lee, Variation of mechanical characteristics of polyurethane foam: Effect of test method, Materials, vol. 12, 2019. https://doi.org/10.3390/ma12172672.

[74] L.C.S. Nunes, Modified slotted shear test for a thin sheet of solid polymer under large deformations, Polym Test., vol. 45, pp. 20–30, 2015. https://doi.org/10.1016/j.polymertesting.2015.05.003.

[75] F. Stojcevski, T. Hilditch, L.C. Henderson, A modern account of Iosipescu testing, Compos Part A Appl Sci Manuf, vol. 107, pp. 545–554, 2018. https://doi.org/10.1016/j.compositesa.2018.02.011.

[76] J.C. Xavier, N.M. Garrido, M. Oliveira, J.L. Morais, P.P. Camanho, F. Pierron, A comparison between the Iosipescu and off-axis shear test methods for the characterization of Pinus Pinaster Ait, in: Compos Part A Appl Sci Manuf, pp. 827–840, 2004. https://doi.org/10.1016/j.compositesa.2004.01.013.

[77] F. Pierron, A. Vautrin, Accurate comparative determination of the in-plane shear modulus of T300/914 by the iosipescu and 45° off-axis tests, Comp Sci Techn, vol 52, no 1, pp. 61-72, 1994. https://doi.org/10.1016/0266-3538(94)90008-6.

[78] J.H. Choi, J. Jang, W. Shim, J.M. Cho, S.J. Yoon, C.H. Choi, H.N. Han, W.R. Yu, Determination of the in-plane shear modulus of unidirectional carbon fiber-reinforced plastics using digital image correlation and finite-element analysis, Compos Struct, vol. 229, 2019. https://doi.org/10.1016/j.compstruct.2019.111392.

[79] M. Garrido, P. Melro, J.R. Correia, Effects of elevated temperature on the shear response of end-grain balsa used in composite sandwich panels, J Sand Struct Mat, vol. 23, pp. 2106–2126, 2021. https://doi.org/10.1177/1099636220909773.

[80] N.A. Danila, I. Blanari, P.D. Barsanescu, Determining the state of stress in the narrow section of Arcan test specimens, by the FEM method, in: IOP Conf Ser Mater Sci Eng, Institute of Physics Publishing, 2019. https://doi.org/10.1088/1757-899X/564/1/012066.

[81] A. Fathi, J.H. Keller, V. Altstaedt, Full-field shear analyses of sandwich core materials using Digital Image Correlation (DIC), Compos B Eng, vol. 70, pp. 156–166, 2015. https://doi.org/10.1016/j.compositesb.2014.10.045.

[82] T. Voiconi, E. Linul, L. Marsavina, T. Sadowski, and M. Knec, Determination of flexural properties of rigid PUR foams using digital image correlation, SSP, vol. 216, pp. 116–121, 2014. DOI: 10.4028/www.scientific.net/SSP.216.116.

[83] A.R. Nazari, M.Z. Kabir, H. Hosseini Toudeshky, Investigation of elastomeric foam response applied as core for composite sandwich beams through progressive failure of the beams, J Sand Struct Mat, vol. 21, pp. 604–638, 2019. https://doi.org/10.1177/1099636217697496.

[84] P. Li, Y.B. Guo, V.P.W. Shim, A rate-sensitive constitutive model for anisotropic cellular materials - Application to a transversely isotropic polyurethane foam, Int J Solids Struct, vol. 206, pp. 43–58, 2020. https://doi.org/10.1016/j.ijsolstr.2020.08.007.

[85] R. Bigger, B. Blaysat, C. Boo, M. Grewer, J. Hu, A. Jones, M. Klein, K. Raghavan, P. Reu, T. Schmidt, T. Siebert, M. Simenson, D. Turner, A. Vieira, T. Weikert, A Good Practices Guide for Digital Image Correlation, 2018. https://doi.org/10.32720/idics/gpg.ed1.

[86] L. Marsavina, D.M. Constantinescu, E. Linul, T. Voiconi, D.A. Apostol, Shear and mode II fracture of PUR foams, Eng Fail Anal, vol. 58, pp. 465–476, 2015. https://doi.org/10.1016/j.engfailanal.2015.05.021.

[87] S.T. Taher, O.T. Thomsen, J.M. Dulieu-Barton, Bidirectional thermo-mechanical properties of foam core materials using DIC, in: Conference Proceedings of the Society for Experimental Mechanics Series, Springer New York LLC, pp. 67–74, 2011. https://doi.org/10.1007/978-1-4614-0207-7_9.

[88] H. Daiyan, E. Andreassen, F. Grytten, H. Osnes, R.H. Gaarder, Shear Testing of Polypropylene Materials Analysed by Digital Image Correlation and Numerical Simulations, Exp Mech, vol. 52, pp. 1355–1369, 2012. https://doi.org/10.1007/s11340-012-9591-7.

[89] G. Escusa, F. Cruz, J. Sena-Cruz, E. Pereira, I. Valente, J. Barros, SHEAR BEHAVIOUR OF POLYURETHANE FOAM, APFIS2017-6 th Asia-Pacific Conference on FRP in Structures, 19-21st July 2017.

[90] M. Kalina, F. Šimčák, M. Hagara, M. Schrötter, M. Štamborská, The use of the experimental optical technique for investigation of shear strains of the samples exposed to shear stress beyond the yield point, in: Procedia Eng, Elsevier Ltd, pp. 264–272, 2012. https://doi.org/10.1016/j.proeng.2012.09.513.

[91] F. Pierron, Identification of materials mechanical properties from full-field measurements: Latest advances in the virtual fields method, in: Applied Mechanics and Materials, Trans Tech Publications Ltd, pp. 3–9, 2008. https://doi.org/10.4028/www.scientific.net/AMM.13-14.3.

[92] M. Grediac and L. Dufort, Experimental evidence of parasitic effects in the shear test on sandwich beams, Exp. Mech., vol. 42, no. 2, pp. 186–193, 2002. https://doi.org/10.1007/BF02410882

[93] C. G'Sell, S. Boni, and S. Shrivastava, Application of the plane simple shear test for determination of the plastic behaviour of solid polymers at large strains, J. Mater. Sci., vol. 18, no. 3, pp. 903–918, 1983. https://doi.org/10.1007/BF00745590

[94] S. Demirel, B. Ergun Tuna, Evaluation of the cyclic fatigue performance of polyurethane foam in different density and category, Polym Test, vol. 76, pp. 146–153, 2019. https://doi.org/10.1016/j.polymertesting.2019.03.019.

[95] H. Jmal, R. Dupuis, E. Aubry, Quasi-static behavior identification of polyurethane foam using a memory integer model and the difference-forces method, Journal of Cellular Plastics, vol. 47, pp. 447–465, 2011. https://doi.org/10.1177/0021955X11406101.

[96] N.J. Mills, Finite element models for the viscoelasticity of opencell polyurethane foam, Cell. Polym., vol. 25, no. 5, pp. 293–316, 2006. https://doi.org/10.1177/026248930602500502.

[97] Y. Shen, F. Golnaraghi, and A. Plumtree, Modelling compressive cyclic stress-strain behaviour of structural foam, Int. J. Fatigue, vol. 23, no. 6, pp. 491–497, 2001. https://doi.org/10.1016/S0142- 1123(01)00014-7.

[98] J. Diani, B. Fayolle, P. Gilormini, A review on the Mullins effect, Eur Polym J, vol. 45, pp.) 601–612, 2009. https://doi.org/10.1016/j.eurpolymj.2008.11.017.

[99] O. Duncan, F. Clegg, A. Essa, A.M.T. Bell, L. Foster, T. Allen, A. Alderson, Effects of Heat Exposure and Volumetric Compression on Poisson's Ratios, Young's Moduli, and Polymeric Composition During Thermo-Mechanical Conversion of Auxetic Open Cell Polyurethane Foam, Phys Status Solidi B Basic Res, vol. 256, 2019. https://doi.org/10.1002/pssb.201800393.

[100] G.N. Greaves, A.L. Greer, R.S. Lakes, T. Rouxel, Poisson's ratio and modern materials, Nat Mater, vol. 10, pp. 823–837, 2011. https://doi.org/10.1038/nmat3134.

[101] B. Sanborn and B. Song, Poisson's ratio of a hyperelastic foam under quasi-static and dynamic loading, Int. J. Impact Eng., vol. 123, no. 1, pp. 48–55, 2019. https://doi.org/10.1016/j.ijimpeng.2018. 06.001.

[102] C.W. Smith, R. J. Wootton, and K. E. Evans, Interpretation of experimental data for Poisson's ratio of highly nonlinear materials, Exp. Mech., vol. 39, no. 4, pp. 356–362, 1999. https://doi.org/10. 1007/BF02329817.

[103] A. Dorfmann, R.W. Ogden, A constitutive model for the Mullins effect with permanent set in particle-reinforced rubber, Int J Solids Struct, vol. 41, pp. 1855–1878, 2004. https://doi.org/10.1016/j.ijsolstr.2003.11.014.

[104] G. Silber, M. Schrodt, G. Benderoth, and A. Kuhhorn, € Hyperelastic description of polymer soft foams at finite deformations, Tech. Mech., vol. 25, no. 3–4, pp. 162–173, 2005.

[105] I. Carranza, A.D. Crocombe, I. Mohagheghian, P.A. Smith, A. Sordon, G. Meeks, C. Santoni, Characterising and modelling the mechanical behaviour of polymeric foams under complex loading, J Mater Sci, vol. 54, pp. 11328–11344, 2019. https://doi.org/10.1007/s10853-019-03673-8.

[106] F.S. Chang, J.O. Hallquist, D.X. Lu, B.K. Shahidi, C.M. Kudelko, and J.P. Tekelly, Finite element analysis of low-density high-hysteresis foam materials and the application in the automotive industry, SAE Tech. Pap., no. 940908, 1994. https://doi.org/10.4271/940908.

[107] K. Bouchahdane, N. Ouelaa, and A. Belaadi, Static and fatigue compression behaviour of conventional and auxetic open-cell foam, Mech. Adv. Mater. Struct., pp. 1–14, 2021. https://doi.org/10.1080/ 15376494.2021.1972496.

[108] S. Cui, B. Gong, Q. Ding, Y. Sun, F. Ren, X. Liu, Q. Yan, H. Yang, X. Wang, B. Song, Mechanical metamaterials foams with tunable negative poisson's ratio for enhanced energy absorption and damage resistance, Materials, vol. 11, 2018. https://doi.org/10.3390/ma11101869.

[109] R.H. Pritchard, P. Lava, D. Debruyne, E.M. Terentjev, Precise determination of the Poisson ratio in soft materials with 2D digital image correlation, Soft Matter, vol. 9, pp. 6037–6045, 2013. https://doi.org/10.1039/c3sm50901j.

[110] J. Lisiecki, T. Błazejewicz, S. Kłysz, G. Gmurczyk, P. Reymer, G. Mikułowski, Tests of polyurethane foams with negative Poisson's ratio, Phys Status Solidi B Basic Res, vol. 250, pp. 1988–1995, 2013. https://doi.org/10.1002/pssb.201384232.

[111] J.P. Brincat, K.M. Azzopardi, A. Buttigieg, F. Scarpa, J.N. Grima, R. Gatt, Foams as 3D perforated systems: An analysis of their Poisson's ratios under compression, Phys Status Solidi B Basic Res, vol. 251, pp. 2233–2238, 2014. https://doi.org/10.1002/pssb.201484262.

[112] W. H. El-Ratal and P. K. Mallick, Elastic response of flexible polyurethane foams in uniaxial tension, J. Eng. Mater. Technol., vol. 118, no. 2, pp. 157–161, 1996. https://doi.org/10.1115/1.2804881.

[113] R.D. Widdle, A. K. Bajaj, and P. Davies, Measurement of the Poisson's ratio of flexible polyurethane foam and its influence on a uniaxial compression model, Int. J. Eng. Sci., vol. 46, no. 1, pp. 31–49, 2008. https://doi.org/10.1016/j.ijengsci.2007.09.002.

[114] Y. C. Fung, Foundations of solid mechanics, J. R. Aeronaut. Soc., vol. 70, no. 663, p. 525, 1968. https://doi.org/10.1017/ S0001924000058632.

[115] B. Banerjee, B. Kraus, and R. Das, Characterization of an anisotropic low-density closed-cell polyurethane foam, 2015. https://doi.org/10.13140/RG.2.1.2971.2088.

[116] J.B. Choi and R. S. Lakes, Non-linear properties of polymer cellular materials with a negative Poisson's ratio, J. Mater. Sci., vol. 27, no. 17, pp. 4678–4684, 1992. https://doi.org/10.1007/BF01166005.

[117] J.G. Murphy and G. A. Rogerson, A method to model simple tension experiments using finite elasticity theory with an application to some polyurethane foams, Int. J. Eng. Sci., vol. 40, no. 5, pp. 499–510, 2002. https://doi.org/10.1016/S0020-7225(01)00079-9.

[118] L. Marsavina, D. Constantinescu, E. Linul, T. Voiconi, D. Apostol, and T. Sadowski, Damage identification and influence on mechanical properties of closed cell rigid foams, 13th International Conference on Fracture, ICF 2013, vol. 4, 2013.

[119] Simcenter Madymo Theory Manual, 2022. https://support.sw.siemens.com/en-US/product/246637901.

[120] http://mscnastrannovice.blogspot.kr/2015/04/what-is-difference-between-mbd-and-fea.html.

[121] https://caendkoelsch.wordpress.com/2017/12/31/what-is-the-difference-between-finite-element-method-fem-and-multi-body-dynamics-mbd/

[122] G. Rechnitzer, R. Zou, R. Grzebieta, MADYMO COMPUTER MODELLING OF ENERGY ABSORBING REAR UNDERRUN BARRIERS FOR HEAVY VEHICLES-A PILOT STUDY, Monash University Accident Research Centre - Report no 112 - 1997.

[123] Simcenter Madymo Model Manual, Version 2306, Siemens Digital Industries Software. www.siemens.com/simcenter madymo.

[124] Michiel Unger, Siemens Digital Industries Software, Where digital twin meets tomorrow.

[125] D.F. Shanahan, Human Tolerance and Crash Survivability, North Atlantic Treaty Organization. (NATO), Research and Technology Organization Human Tolerance and Crash Survivability, 2004.

[126] A. Adams, H. Lankarani, Aircraft Seat Cushion Performance Evaluation and Replacement Implementation, 2003, *Age* 8, 1. https://doi.org/10.1533/ijcr.2003.0234.